UNIVERSITY OF CALIFORNIA
SANTA CRUZ

PREFERENTIAL CONCENTRATION OF HEAVY INERTIAL PARTICLES USING THE TWO-FLUID EQUATIONS

A dissertation submitted in partial satisfaction of the
requirements for the degree of

DOCTOR OF PHILOSOPHY

in

APPLIED MATHEMATICS AND STATISTICS

by

Sara Nasab

September 2021

The Dissertation of Sara Nasab
is approved:

Professor Pascale Garaud, Chair

Professor Nicholas Brummell

Professor Patrick Chuang

Professor Eckart Meiburg

Peter Biehl
Vice Provost and Dean of Graduate Studies

Table of Contents

List of Figures

List of Tables

Abstract

Preferential concentration of heavy inertial particles using the two-fluid equations

by

Sara Nasab

Preferential concentration describes the tendency of heavy particles to accumulate in certain regions of a turbulent flow. This process has been hypothesized to play a role in particle growth which is of crucial importance in numerous physical and engineering applications. The efficiency of preferential concentration is known to depend on the ratio of the particle stopping time to the turbulent eddy turnover time, which is called the Stokes number. In this thesis, we investigate the role of turbulence on preferential concentration of heavy particles with Stokes number less than unity. We use Direct Numerical Simulations and adopt the two-fluid formalism, where the particulate phase is treated as a continuum. In the first work, we study a two-way coupled system in the particle-induced Rayleigh-Taylor instability, and observe the striking emergence of dense, filamentary particle structures. Most notably, we find that the particle concentration enhancement primarily depends on three properties of the system: the rms fluid velocity, the Stokes number, and the assumed particle diffusivity from the two-fluid equations. Additionally, we note that when preferential concentration is dominant, the probability distribution function of the particle concentration takes on a distinctive form, characterized by an exponential tail whose slope is related to the same three properties listed above. In the second part, we further extend our study to a regime in which turbulence is externally-driven, and verify that the results found in the first study also hold. In the final work, we use a box-counting algorithm to identify and extract key features of the dense particle structures. We find in particular that these

structures have a large aspect ratio. We propose an advection-diffusion model to predict their thickness, and find preliminary evidence that suggests that their long dimension depends on the Taylor microscale.

Dedicated to my family

Mom, Dad, Arian, & Armand

Acknowledgments

This work, and the completion of my graduate program, would not have been possible without the love and support of numerous individuals.

First, I would like to thank Pascale Garaud for being an outstanding advisor, playing the role of mentor in more ways than one. Thank you for being a constant during the past several years. I am especially grateful for your dedication and patience in challenging me to be a better researcher. The last several months have been especially grueling, but having you as my advisor helped me push to the very end. And of course, thank you for introducing me to your wonderful daughter Julia, whose knock-knock jokes will only get better with time.

I would also like to thank my dissertation committee: Patrick Chuang, Eckart Meiburg, and Nic Brummell. Thank you for the valuable discussions and helpful comments over the years. It also goes without saying that a considerable amount of time goes into reading a thesis, and for that, I am grateful.

I feel very lucky to have met such incredible friends during my time at Santa Cruz, making me feel at home from the very beginning. Thank you, Raquel Barata, for being my first friend here, and helping me see the good in others. A huge "thumbs up" to George Labaria, for eventually convincing me after four years that I like climbing. Thank you, Richard Shaffer, for the 6-hour Zoom calls and conversations that, more often than not, lead to Hannibal Buress. Thank you, Michael Lavell (otherwise known as Mäk), for inspiring me to be a better student, and being a wonderful example on what it takes to be a great one. Thank you, Tenavi Nakamura-Zimmerer, for believing in me during those times that I did not believe in myself. Thank you, Bethany Johnson, for your kindness; I am so glad you ended up at Santa Cruz. Thank you, Martín Rodriguez, for making me feel like part of the family and for the daily *meh-mehs* (let me know when you

want to go into business together). Thank you, Heidi Rogers, for your honesty and vulnerability, and always standing up for what you believe in. Thank you, Carmen Segura, for being a solid friend your last year at Santa Cruz (so lucky I made the roster)! Thank you, Kelsey Forbush, for taking me to wine tastings and feeding me on a weekly basis. Thank you, Daphne Gorman, for the inappropriate roommate humor. Thank you, Marie Lau, for being so frank and coining the expression "central fat". Thank you, Alexandra Race, for being a wonderful roommate and always a thoughtful friend. Thank you, Katie Giampa and Lizzie Thurman, for being my designated Bumble Buds, and being by my side, especially during the difficult times. Thank you, Annalisa Cadonna, for being a great example of what a beautiful life after the Ph.D. looks like; it looks like there will hopefully be less tears and less fries. Thank you, Alessia Cecchet, for being a constant source of support, especially during this past year. Our long Monday walks have been essential to start my week off right, and I'm not sure how I would have stayed sane otherwise. You are truly a wonderful friend, and I hope for great things for you in the near future.

Thank you to my smart and beautiful friends from Tennessee, who are always just a phone call away: Emily Best (pharmacist!), Natalee Lewis (physical therapist!), and Kim Hawkes (mother *and* nurse!). I am grateful for our long-lasting friendship. You mean so much to me.

Finally, I would like to thank my family: my brothers Armand and Arian, and my parents Ahad and Jenny. From math competitions to soccer games to swimmeets and finally to the Ph.D. program, thank you for your never-ending support and encouragement. Thank you for letting me figure things out on my own, and trusting me along the way. I love you all more than you will ever know.

Chapter 1

Introduction

1.1 Particle-laden flows

Particle-laden flows appear in many fields ranging from biology, chemical engineering, to geophysical and astrophysical applications. They are defined as two-phase flows, consisting of a dispersed phase (usually modeled as spherical particles such as sediments, droplets, or bubbles) and a continuous carrier phase. These flows are difficult to model, combining two challenging topics of fluid mechanics: turbulence and multi-phase physics. The major obstacle keeping us from fully understanding these flows is the vast range of time and length scales associated with the microphysics of the particles and the scales of turbulent motion.

A notable physical process of two-phase flows is preferential concentration, which describes the accumulation of heavy particles within certain regions of the fluid due to their inertia. Thus, the particle distribution becomes non-uniform, resulting in regions of higher particle concentration and regions of low concentration. It has been shown that the primary mechanisms that can cause preferential concentration are the inertial bias mechanism and the sweep-stick mechanism. The inertial bias mechanism describes the tendency of small particles to concen-

trate in regions of high strain and low vorticity (Maxey, 1987), as illustrated in Figure 1.1 and described in more detail in Section 1.2. For larger particles, the sweep-stick mechanism plays a dominant role, in which dense clusters form in zero acceleration points of the flow, subsequently "sticking" and then moving with the local fluid velocity (Goto & Vassilicos, 2006; Coleman & Vassilicos, 2009). In this thesis, we focus our investigation on small inertial particles, and therefore only study the effect of preferential concentration due to the inertial bias mechanism.

Figure 1.1: Illustration of a single particle interacting in 2D flow (figure adapted from Eaton & Fessler, 1994).

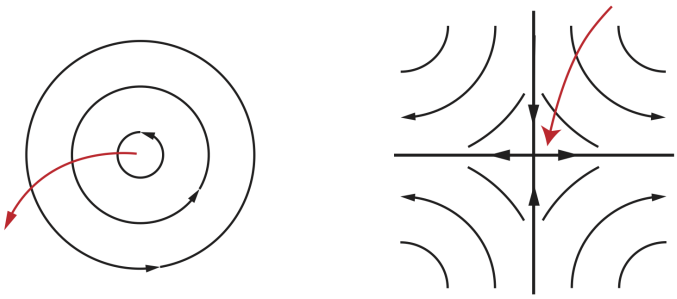

Historically, preferential concentration has been chiefly investigated in systems well within the dilute limit, where particles are typically characterized as small and spherical. One of the first reported experimental observations of preferential concentration was done by Kada & Hanratty (1960). They found that beyond a certain volume fraction the concentration field of heavy particles was non-uniform; however these results were not quantitatively explained. Later works in the context of turbulent pipe flows (Fessler et al., 1994; Wang & Squires, 1996; Rouson & Eaton, 2001) and free shear flows (Crowe et al., 1985; Kobayashi et al., 1988; Wen et al., 1992; Gañán-Calvo & Lasheras, 1991; Raju & Meiburg, 1997) found corroborating evidence that confirmed that the largest particle densities were located near the outer edges of coherent vortex structures. This observation was later explained by Maxey (1987), who showed that inertial particles preferentially

accumulate in regions of low vorticity and high strain rate (see Section 1.2.2 for more details). Chein & Chung (1988b) further demonstrated that the Stokes number, which is defined as the ratio of the particle stopping time to the typical fluid eddy turnover time, has a direct impact on the efficiency of preferential concentration. Most of these discoveries have provided the basis for understanding particle-laden flows (see review papers by Eaton & Fessler 1994; Elghobashi 1994; Balachandar & Eaton 2010; Monchaux et al. 2012).

Higher concentrations due to preferential concentration can promote collisional growth, a topic that is particularly relevant in geophysical and astrophysical applications. For example in clouds, the processes by which growth from micron-sized droplets to millimeter-sized raindrops occur remain a subject of continuing research. These processes are thought to include condensational growth, collision-coalescence, sedimentation, and latent heating. Although a wealth of research has been done through controlled laboratory experiments (Saw et al., 2008; Bateson & Aliseda, 2012) and numerical simulations (Devenish et al. 2012; Grabowski & Wang 2013 and references therein), most studies remain highly idealized either only capturing a subset of physical processes, incorporating a relatively low Reynolds number, or modeling a monodisperse collection of droplets. Despite these limitations, it is now known that condensation and Brownian motion alone are only effective for forming droplets around $20 - 30$ μm in diameter. To grow to sizes needed to initiate rainfall, other pathways to droplet growth need to be considered. Recent works (Wang et al., 2000; Ghosh & Jonas, 2001; Ayala et al., 2008) have suggested that preferential concentration does play a role in increasing the local droplet concentration, and thus aid in enhancing collision rates and contribute to droplet growth.

Preferential concentration has also been widely proposed to play a part in the

coagulation of dust particles in accretion disks (Weidenschilling & Cuzzi, 1993; Blum & Wurm, 2008; Birnstiel et al., 2016). During the initial phase of planetary formation, micron-sized dust grains eventually grow to kilometer-sized planetesimals, however the mechanisms responsible for particle growth are still unclear. It is known that during the onset of planetary formation, accretion disks are composed of 99% gas and 1% solid micron-sized dust grains. The small dust grains are well-coupled to the gas, so that their velocities are primarily determined by Brownian motion and turbulence. Because their velocities are relatively small, these particles stick on impact resulting in a newly formed larger particle (Weidenschilling, 1977; Blum & Wurm, 2008). However in order for these type of collisions to occur, particles must be relatively near one another, and thus preferential concentration may facilitate this process (see Blum 2006 and references therein).

1.2 Mathematical formulation

1.2.1 Stokes number

Preferential concentration in turbulent, particle-laden flows has been found to primarily depend on the nondimensional Stokes number. The Stokes number is typically defined as the ratio between the particle stopping time τ_p to the characteristic fluid eddy turnover time τ_e. It is now known that the Stokes number controls the effect that particle inertia has on the interactions with turbulence (Maxey, 1987).

The particle stopping time τ_p is a parameter that can be easily determined

based on intrinsic particle properties, and is written as

$$\tau_p = \frac{d_p^2 \rho_s}{18 \rho_f \nu}, \tag{1.1}$$

where d_p is the diameter of the particle, ρ_s is the solid density of the particle, ρ_f is the mean fluid density, and ν is the kinematic viscosity of the fluid. On the other hand, the typical eddy turnover time is one that is not as readily agreed upon. For simpler flows where there exist only one characteristic timescale, the choice for τ_e is obvious. For fully turbulent systems that consist of a wide range of time scales, the eddy turnover timescale depends on the aspect of the flow that one wishes to study (which is then used to determine τ_e). It is common in turbulent flows to choose the eddy turnover time based on the smallest scales of turbulence (i.e. on the Kolmogorov scale), but this is not the only possible choice.

It is known that when the Stokes number is much smaller than unity, particle inertia is negligible and as a result, particle motion is dictated entirely by the carrier flow (Crowe et al., 1985; Chein & Chung, 1988b; Tang et al., 1992; Maxey, 1987). When the Stokes number is of order unity, particles tend to preferentially concentrate in regions of low vorticity and high strain rate. Finally when the Stokes number is much larger than unity, the particles become decorrelated from fluid motions, and as a result, the particles do not respond to the changes in local flow structures as compared to the smaller particles.

We can see how the Stokes number influences the spatial distribution of particles in 3D Direct Numerical Simulations (DNSs) generated for the study described in Ch. 4. In Figure 1.2, we present snapshots of the particle concentration field in a turbulent flow after the system has reached a statistically steady state, where the red color represents larger values in particle concentration and the blue color represent lower values in particle concentration. When $St \sim O(10^{-3})$ as shown

Figure 1.2: Snapshots of the particle concentration field from Direct Numerical Simulations with varying Stokes number (with other parameters fixed to be the same), whose model set-up is described in Section 4.2.

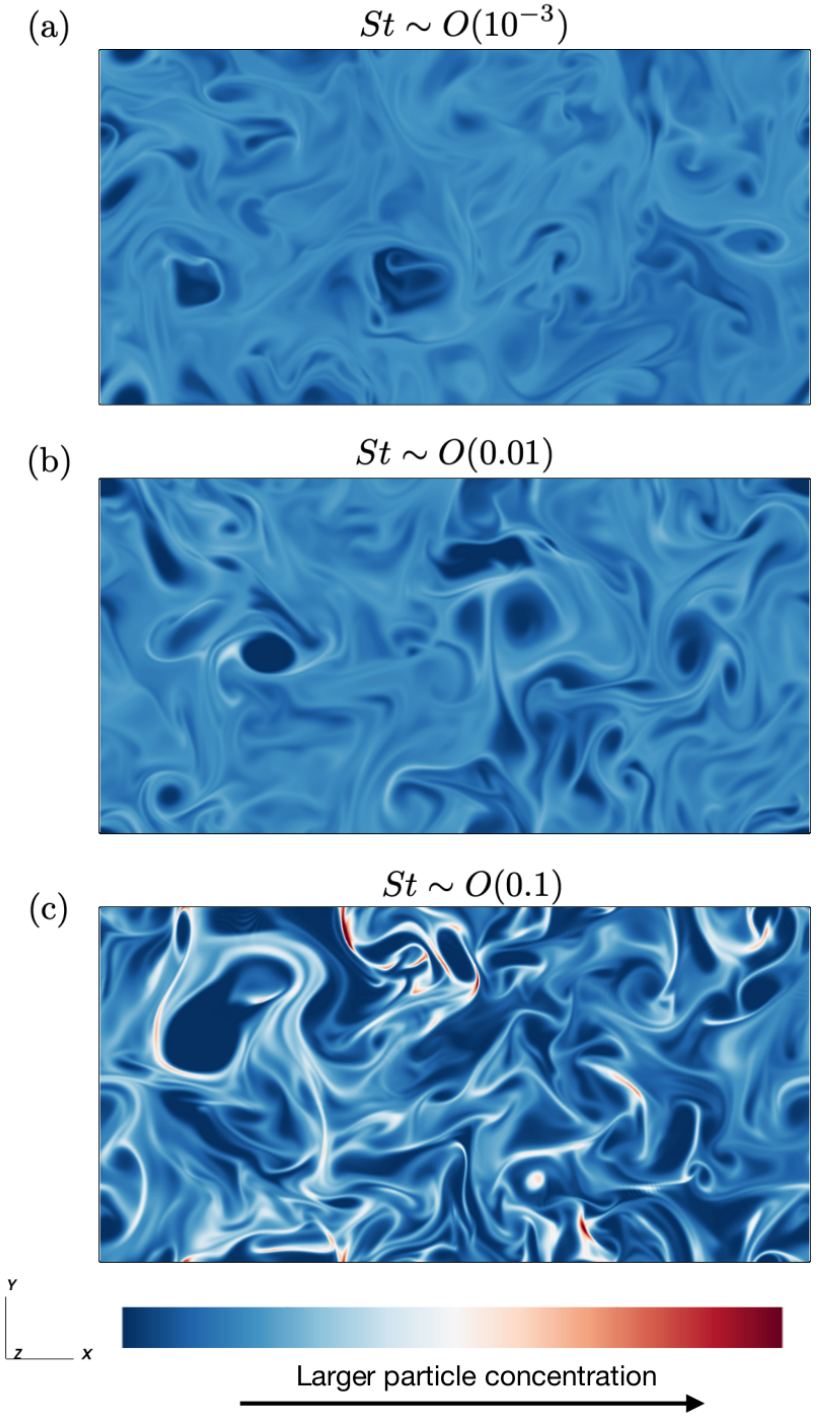

by Figure 1.2(a), the spatial distribution of the particles appears to be fairly uniform, which is expected when particle inertia is negligible. In Figure 1.2(b) when the Stokes number increases to $St \sim O(0.01)$, particles begin to accumulate significantly more around the vortex edges, resulting in a slight increase in particle concentration enhancement. When $St \sim O(0.1)$ as shown in Figure 1.2(c), we see that the spatial distribution of the particles has indeed become more heterogeneous due to preferential concentration. Specifically, we see the emergence of highly concentrated, filamentary structures (shown in red) as well as contrasting regions void of particles (shown in dark blue). As discussed earlier, previous studies have likewise shown that inertial particles are rarely found inside vortex structures, and instead found in the saddle regions between vortices (Fessler et al., 1994; Crowe et al., 1985; Maxey & Corrsin, 1986).

1.2.2 Maxey's model

In this section, we show how the Stokes number is related to preferential concentration following the original derivations by Maxey (1987). We specifically focus on the long-term behavior of a collection of heavy particles, and ultimately see how inertial bias creates a tendency for the particles to aggregate in regions of high strain rate and low vorticity.

Here and for the remainder of this work, we focus on particulate flows in which the particle solid density is much larger than the mean density of the fluid (i.e. $\rho_s \gg \rho_f$). We also study a monodisperse collection of particles in which each particle is sufficiently small such that the fluid Reynolds number based on the particle size and velocity is smaller than one, and thus follows Stokes' drag. Following Maxey (1987), the motion of a single spherical particle in this limit is

then modeled by

$$\frac{d\mathbf{v}_p}{dt} = \frac{1}{\tau_p}\Big\{\mathbf{u}(\mathbf{x}_p(t), t) - \mathbf{v}_p + \mathbf{w_s}\Big\} \tag{1.2}$$

where $\mathbf{u}$ is the fluid velocity at the particle position $\mathbf{x}_p$ at time t, $\mathbf{v}_p$ is the particle velocity, and $\mathbf{w_s} = \tau_p \mathbf{g}$ is the particle settling velocity where $\mathbf{g} = -g\hat{\mathbf{e}}_z$ is the acceleration due to gravity.

In order to show how the Stokes number St influences particle motion, we nondimensionalize Eq. (1.2) with respect to a set of characteristic velocity and length scales for the given system represented by U_c and L_c. The following nondimensional variables are then:

$$\hat{t} = \frac{t}{L_c/U_c}, \qquad \hat{\mathbf{x}}_p = \frac{\mathbf{x}_p}{L_c}, \qquad \hat{\mathbf{u}} = \frac{\mathbf{u}}{U_c}, \qquad \hat{\mathbf{v}}_p = \frac{\mathbf{v}_p}{U_c}. \tag{1.3}$$

The resulting nondimensionalized form of Eq. (1.2) is then

$$\frac{d\hat{\mathbf{v}}_p}{dt} = \frac{1}{St}\Big\{\hat{\mathbf{u}}(\hat{\mathbf{x}}_p(t), t) - \hat{\mathbf{v}}_p + \hat{\mathbf{w}}_s\Big\}, \tag{1.4}$$

where $St = \tau_p/\tau_e$, which we recognize as the ratio of the stopping time to a characteristic timescale of the flow, as introduced earlier. The nondimensional settling velocity is given by $\hat{\mathbf{w}}_s = \mathbf{w_s}/U_c$, and the variable t for the remainder of this derivation is implicitly nondimensional.

First we consider the case when particle inertia is negligible, or when $St \to 0$. We carry out an asymptotic expansion to the lowest order in St and obtain

$$\hat{\mathbf{v}}_p = \hat{\mathbf{u}}(\hat{\mathbf{x}}_p(t), t) + \hat{\mathbf{w}}_s, \tag{1.5}$$

and see that the particle velocity is linearly dependent on the fluid velocity and the terminal settling velocity. That is, the motion of the particle is dictated by

the local fluid velocity.

We next consider the case when particle inertia is small but not negligible. We integrate Eq. (1.4) over the time interval $[t_0, t]$ and obtain the integral solution for the particle velocity $\hat{\mathbf{v}}_p$:

$$\hat{\mathbf{v}}_p(t) = e^{-t/St}\hat{\mathbf{v}}_p(t_0) + \mathbf{w}_s(1 - e^{-t/St}) + \frac{1}{St}\int_{t_0}^{t} e^{-(t-t')/St}\,\hat{\mathbf{u}}(t')\,dt', \tag{1.6}$$

where $\hat{\mathbf{u}}(t) \equiv \hat{\mathbf{u}}(\hat{\mathbf{x}}_p(t), t)$ for convenience.

Applying integration by parts yields the following solution for the particle position $\hat{\mathbf{x}}_p$.

$$\begin{aligned}\hat{\mathbf{x}}_p(t) = \hat{\mathbf{x}}_p(t_0) + St(\hat{\mathbf{v}}_p(t_0) - \hat{\mathbf{w}}_s) + \hat{\mathbf{w}}_s t + \int_{t_0}^{t} \hat{\mathbf{u}}(t')\,dt' - St\hat{\mathbf{u}}(t) \\ + e^{-t/St}\Big[- St(\hat{\mathbf{v}}_p(t_0) - \hat{\mathbf{w}}_s) + St\hat{\mathbf{u}}(t_0)\Big] + O(St^2).\end{aligned} \tag{1.7}$$

Since we are interested in the long-term averaged particle velocity solution, the initial particle velocity does not hold significance to the final solution. With that in mind, Maxey (1987) substitutes the lowest order particle velocity solution (1.5)

$$\hat{\mathbf{v}}_p(t_0) = \hat{\mathbf{u}} + \hat{\mathbf{w}}_s$$

in (1.7), so that the particle position then simplifies to

$$\hat{\mathbf{x}}_p(t) = \hat{\mathbf{x}}_p(t_0) + St\hat{\mathbf{u}}(t_0) + \hat{\mathbf{w}}_s t + \int_{t_0}^{t} \hat{\mathbf{u}}(t')\,dt' - St\hat{\mathbf{u}}(t) + O(St^2). \tag{1.8}$$

Next taking the temporal derivative of Eq. (1.8), the updated differential equation becomes

$$\frac{d\hat{\mathbf{x}}_p}{dt} = \hat{\mathbf{u}}(t) + \hat{\mathbf{w}}_s - St\frac{d\hat{\mathbf{u}}}{dt} + O(St^2). \tag{1.9}$$

Up to the first-order correction term in St, we clearly see that the particle velocity now has additional dependence on the Stokes number given by the last term on the right-hand side. Note that (1.9) was derived following Maxey for historical accuracy, but it can also be obtained more easily by applying Laplace's approximation to the particle velocity equation (see Appendix A for more details).

In order to express the particle velocity in (1.9) as a function of the instantaneous particle position $\hat{\mathbf{x}}_p$, we recast $d\hat{\mathbf{u}}/dt$ as the derivative following the particle as

$$\begin{aligned}\frac{d\hat{\mathbf{u}}}{dt} &= \left(\frac{\partial \hat{\mathbf{u}}}{\partial t} + \frac{d\hat{\mathbf{x}}_p}{dt}\cdot\nabla\hat{\mathbf{u}}\right)\bigg|_{\hat{\mathbf{x}}_p(t)} \\ &= \left(\frac{\partial \hat{\mathbf{u}}}{\partial t} + (\hat{\mathbf{u}}(\hat{\mathbf{x}}_p(t),t) + \hat{\mathbf{w}}_s)\cdot\nabla\hat{\mathbf{u}}\right)\bigg|_{\hat{\mathbf{x}}_p(t)} + O(St), \end{aligned} \tag{1.10}$$

where in the second line, we substitute the lowest order particle velocity solution (1.5) for $d\hat{\mathbf{x}}_p/dt$. Finally we substitute the first-order solution of (1.10) for $d\hat{\mathbf{u}}/dt$ in (1.9) and get

$$\frac{d\hat{\mathbf{x}}_p}{dt} = \hat{\mathbf{u}}(\hat{\mathbf{x}}_p(t),t) + \hat{\mathbf{w}}_s - St\left(\frac{\partial \hat{\mathbf{u}}}{\partial t} + (\hat{\mathbf{u}}(\hat{\mathbf{x}}_p(t),t) + \hat{\mathbf{w}}_s)\cdot\nabla\hat{\mathbf{u}}\right)\bigg|_{\hat{\mathbf{x}}_p(t)} + O(St^2). \tag{1.11}$$

Written in this way, we easily see the contributions to the particle velocity compared to (1.4) in terms of the fluid velocity, the settling velocity, and the particle position.

These results were then used to investigate the behavior for a *collection* of particles with velocity $\hat{\mathbf{u}}_p$ (defined in Eq. 2.5). For particles with low Stokes number, Maxey (1987) showed that the long-term collective particle velocity can be modeled with a similar equation as the one for the single particle velocity (following methods by Kraichnan 1970, Riley 1971, and Reeks 1980).

Thus in the case for when particle inertia is negligible, the average particle

velocity can be modeled by

$$\hat{\mathbf{u}}_p(\hat{\mathbf{x}}, t) = \hat{\mathbf{u}}(\hat{\mathbf{x}}(t), t) + \hat{\mathbf{w}}_s. \tag{1.12}$$

The divergence of Eq. (1.12) yields $\nabla \cdot \hat{\mathbf{u}}_p = \nabla \cdot \hat{\mathbf{u}} = 0$, implying that the particle concentration field is incompressible. Therefore clustering due to preferential concentration cannot occur for particles when $St \to 0$.

On the other hand, when the Stokes number is small but not negligible, the collective particle velocity is given by

$$\hat{\mathbf{u}}_p(\hat{\mathbf{x}}, t) = \hat{\mathbf{u}}(\hat{\mathbf{x}}, t) + \hat{\mathbf{w}}_s - St\left(\frac{\partial \hat{\mathbf{u}}}{\partial t} + \hat{\mathbf{u}} \cdot \nabla \hat{\mathbf{u}} + \hat{\mathbf{w}}_s \cdot \nabla \hat{\mathbf{u}}\right) + O(St^2), \tag{1.13}$$

where the divergence of (1.13) using Einstein summation convention (in which repeated indices are implicitly summed over) is

$$\nabla \cdot \hat{\mathbf{u}}_p = -\frac{St}{4}\left[\left(\frac{\partial u_i}{\partial x_j} + \frac{\partial u_j}{\partial x_i}\right)^2 - \left(\frac{\partial u_i}{\partial x_j} - \frac{\partial u_j}{\partial x_i}\right)^2\right]. \tag{1.14}$$

We clearly see in this case that the divergence of the particle velocity is not necessarily zero. In the expanded expression on the right-hand side, the first term corresponds to the strain rate and the second term corresponds to vorticity. For the divergence of the particle field to be positive, the strain rate is low and the vorticity is high. In constrast for the divergence to be negative, the strain rate dominates. Therefore, preferential clustering occurs in regions of low vorticity or high strain rate.

1.3 Computational approaches

In this section, we provide a brief overview of the more popular formalisms used to model two-phase flows. The Equilibrium Eulerian approach assumes a continuum treatment of the particles, and is given by an explicit representation for the fluid velocity and a transport equation for the particle concentration. The two-fluid formalism (which is discussed in Ch. 2) also models the particles as a continuum; however in this approach, we require an additional momentum equation for the particle field. The Lagrangian formalism models the dispersed phase as point particles, in which the motion for each particle is tracked individually. In fully resolved simulations (which are not covered in this thesis), the interactions between the two phases as well as the local flow around the particles are fully resolved. Generally speaking, the appropriate formalism in which to model the system primarily depends on particle size (or, the Stokes number), where the hierarchy of formalisms is depicted in Figure 1.3. In what follows, we describe the Equilibrium Eulerian, the two-fluid (separately introduced in Ch. 2), and Lagrangian formalisms in more detail.

Figure 1.3: Hierarchy of modeling approaches for increasing Stokes number.

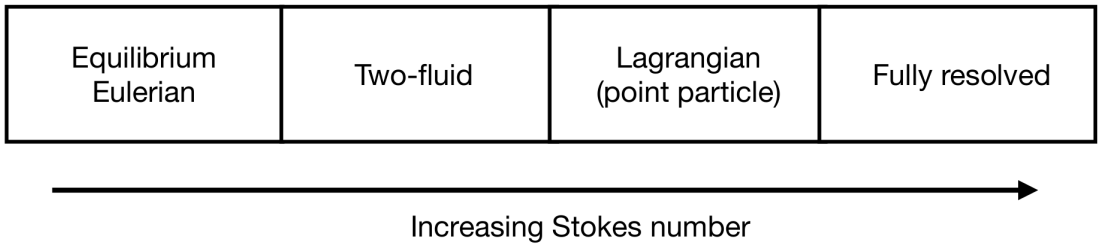

1.3.1 Lagrangian Formalism

With the rise of state-of-the-art computational capabilities, one of the more popular methods is the Lagrangian formalism which integrates Eq. (1.2) separately for each particle in the fluid as

$$\frac{d\mathbf{x}_{p,i}}{dt} = \mathbf{u}_{p,i} \qquad \text{and} \qquad \frac{d\mathbf{u}_{p,i}}{dt} = \frac{\mathbf{u}_i - \mathbf{u}_{p,i}}{\tau_p} + \mathbf{g} \quad \text{for } i = 1, ..., N_p, \tag{1.15}$$

where $\mathbf{x}_{p,i}$ is position of the ith particle, $\mathbf{u}_i = \mathbf{u}(\mathbf{x}_i)$ is the fluid velocity at position $\mathbf{x}_i$, and $\mathbf{u}_{p,i}$ is the velocity of the ith particle. The back reaction of the particles on the fluid is accounted for by adding a mean local drag force $\mathbf{F}_p$ in the Navier-Stokes equation shown here for an incompressible fluid of uniform density ρ_f:

$$\rho_f \left(\frac{\partial \mathbf{u}}{\partial t} + \mathbf{u} \cdot \nabla \mathbf{u} \right) = -\nabla p + \rho \mathbf{g} + \rho_f \nu \nabla^2 \mathbf{u} + \mathbf{F}_p, \tag{1.16}$$

where ρ is the density deviation away from the mean fluid density ρ_f, p is the pressure, and $\mathbf{F}_p$ is explicitly defined as

$$\mathbf{F}_p(\mathbf{x}) = \sum_{i=1}^{n_p(\mathbf{x})} \frac{m_p}{v_c(\mathbf{x})} \frac{\mathbf{u}_{p,i} - \mathbf{u}_i}{\tau_i(\mathbf{x})}, \tag{1.17}$$

where m_p and τ_p are the mass and stopping time of the ith particle, respectively, and $n_p(\mathbf{x})$ is the number of particles in small control volume $v_c(\mathbf{x})$ centered around $\mathbf{x}$. It is worth noting that the Lagrangian and fully-resolved approaches are the only formalisms that can efficiently model a poly-disperse distribution of particles exactly should this be needed. Although there exist current models using this approach that are capable of tracking up to $O(10^9)$ particles, parallelization issues can arise due to an uneven distribution of particles over the domain due to preferential concentration. As a result, the computational load will be unbal-

anced towards the processors responsible for solving the governing equations in the region of the domain corresponding to higher concentrations of particle, and the computational cost can be expensive. Thus for systems in which particles are mono-disperse and are sufficiently small to be well-coupled with the fluid, alternative approaches can be used.

1.3.2 Equilibrium Eulerian formalism

In the following formalism, the particles are not treated individually, but instead, are modeled as a continuum. We also assume that the collection of monodisperse, spherical particles follow Stokes drag. We then define the local mass density ρ_p and collective velocity $\mathbf{u}_p$ to describe this "fluid of particles" in a small volume centered around the position $\mathbf{x}$ as

$$\mathbf{u}_p(\mathbf{x}) = \frac{1}{n_p(\mathbf{x})} \sum_{i=1}^{n_p(\mathbf{x})} \mathbf{u}_{p,i}, \qquad \rho_p = \frac{1}{v_c(\mathbf{x})} \sum_{i=1}^{n_p(\mathbf{x})} m_p. \tag{1.18}$$

When particle inertia is negligible, the particles can be modeled together with the carrier flow as a single fluid. The particle velocity is derived from the Lagrangian equation of motion (1.2) following an expansion in τ_p in the limit of $\tau_p \to 0$, and dimensionally written as

$$\mathbf{u}_p = \mathbf{u} + \mathbf{w}_s. \tag{1.19}$$

Consequently, the drag term (1.17) greatly simplifies in this limit to become

$$\mathbf{F}_p(\mathbf{x}) = \rho_p \mathbf{g}. \tag{1.20}$$

Additionally, the evolution of the particle concentration is modeled by the trans-

port equation

$$\frac{\partial \rho_p}{\partial t} + \mathbf{u}_p \cdot \nabla \rho_p = \kappa_p \nabla^2 \rho_p, \tag{1.21}$$

where κ_p represents particle diffusivity. This term is included under our continuum treatment of particles to stabilize the system when running numerical experiments, although it is also physically motivated. In reality, a group of particles undergo both stochastic collisions with the molecules of the carrier fluid, which results in an added dispersive term in Eq. (1.21) from their Brownian motion, as well as mutual long-range interactions through their wakes which can also be modeled as a diffusion term. We also see that in this limit for which particle inertia is negligible, the particle velocity is divergence free $\nabla \cdot \mathbf{u}_p$, and thus the advection term has been simplified from $\nabla \cdot (\mathbf{u}_p \rho_p)$ to $\mathbf{u}_p \cdot \nabla \rho_p$.

Together, the system of equations for the Equilibrium Eulerian formalism can be written as

$$\rho_f \left(\frac{\partial \mathbf{u}}{\partial t} + \mathbf{u} \cdot \nabla \mathbf{u} \right) = -\nabla p + (\rho + \rho_p)\mathbf{g} + \rho_f \nu \nabla^2 \mathbf{u}, \tag{1.22}$$

$$\frac{\partial \rho_p}{\partial t} + (\mathbf{u} - w_s \hat{\mathbf{e}}_z) \cdot \nabla \rho_p = \kappa_p \nabla^2 \rho_p, \tag{1.23}$$

$$\nabla \cdot \mathbf{u} = 0, \tag{1.24}$$

where the particles and fluid together as a single-phase fluid whose density perturbation away from the mean ρ_f is $\rho + \rho_p$. For this limit to apply, the particle stopping time τ_p must be small enough to instantaneously respond to changes in the fluid motion. In recent works, the Equilibrium Eulerian approach has been adopted (Burns & Meiburg, 2012; Alsinan et al., 2017; Reali et al., 2017) and has the advantage of using an explicit equation for the particle velocity, which is straightforward to implement in the fluid momentum equation.

Other versions of this formalism have been proposed, for which particle inertia

is incorporated in the particle equation. They are easily derived by carrying out an expansion of (1.2) to higher-order terms in τ_p. There also exist several variants of the Equilibrium Eulerian approach that include other relevant forces such as added mass, Basset history, and Saffman lift in the Fast Eulerian approach, which we do not cover in this thesis (Maxey & Riley, 1983; Ferry & Balachandar, 2001). To avoid any confusion, it is worth mentioning that for the remainder of this work, the Equilibrium Eulerian approach refers to the formalism in which particle inertia is negligible, although this terminology is used more broadly in other papers.

Chapter 2

Two-fluid equations

In this section, we present the two-fluid equations in which we use to model particle-laden flows for the remainder of this work. The contents of Section 2.1 was originally part of the reprint presented in Chapter 3 and moved to this portion of the thesis for pedagogical purposes.

2.1 Governing equations

The two-fluid formalism for particle-laden flows can be derived starting from the Lagrangian-Eulerian formalism by locally averaging the particle properties to obtain the continuum density and momentum conservation equations. This essentially follows the derivation of Ishii and Mishima (Ishii & Mishima, 1984) (see also Ishii & Hibiki, 2010; Delhaye & Achard, 1976). The formalism has been widely used within the astrophysics community for studying protoplanetary disks (Youdin & Goodman, 2005; Nakagawa et al., 1986), as well as in studies related to sediment transport in rivers and oceans (Hsu et al., 2004; Bakhtyar et al., 2009; Revil-Baudard & Chauchat, 2013), for instance.

For simplicity in this work, we focus on particulate flows in which the particle

solid density ρ_s is much larger than the mean density of the fluid ρ_f, such as droplets or aerosols in the atmosphere or dust in accretion disks. We also assume that the particles are spherical, monodisperse, and dilute (ensuring that particle-particle collisions do not dominate the particle evolution equations).

2.1.1 Lagrangian formalism

Under the above assumptions, we can model the motion of a single particle interacting with the fluid through Stokes drag by solving the coupled ordinary differential equations

$$\frac{d\mathbf{x_p}}{dt} = \mathbf{u}_p \quad \text{and} \quad \frac{d\mathbf{u}_p}{dt} = \frac{\mathbf{u}(\mathbf{x_p}) - \mathbf{u}_p}{\tau_p} + \mathbf{g}, \tag{2.1}$$

where $\mathbf{x_p}$ is the position of the particle, $\mathbf{u}_p$ is its velocity, $\mathbf{u}(\mathbf{x_p})$ is the fluid velocity at $\mathbf{x_p}$, $\mathbf{g} = -g\hat{\mathbf{e}}_z$ is gravity, and τ_p is the particle stopping time. In (2.1), we have assumed that the reduced mass (which would normally multiply $\mathbf{g}$) is approximately 1 since $\rho_s \gg \rho_f$. We have also neglected other effects such as the Basset history and Saffman lift terms for the same reason (Maxey & Riley, 1983).

To model a collection of N_p monodisperse particles using the LE approach, (2.1) is integrated separately for each particle in the fluid:

$$\frac{d\mathbf{x}_{p,i}}{dt} = \mathbf{u}_{p,i} \qquad \text{and} \qquad \frac{d\mathbf{u}_{p,i}}{dt} = \frac{\mathbf{u}(\mathbf{x}_{p,i}) - \mathbf{u}_{p,i}}{\tau_p} + \mathbf{g} \quad \text{for } i = 1, ..., N_p, \tag{2.2}$$

where $\mathbf{x}_{p,i}$ and $\mathbf{u}_{p,i}$ are the position and velocity of the ith particle, respectively. The back reaction of the particles on the fluid is accounted for by adding a mean local drag force $\mathbf{F}_p$ in the Navier-Stokes equation shown here in the limit of the

Boussinesq approximation (Boussinesq, 1903a; Spiegel & Veronis, 1960):

$$\rho_f\left(\frac{\partial \mathbf{u}}{\partial t} + \mathbf{u}\cdot\nabla\mathbf{u}\right) = -\nabla p + \rho\mathbf{g} + \rho_f\nu\nabla^2\mathbf{u} + \mathbf{F}_p, \tag{2.3}$$

where ρ is the density deviation away from the mean fluid density ρ_f, p is the pressure, ν is the kinematic velocity of the fluid, and $\mathbf{F}_p$ is explicitly defined as

$$\mathbf{F}_p(\mathbf{x}) = -\sum_{i=1}^{N_p} \frac{m_p}{v_\epsilon}\frac{\mathbf{u}(\mathbf{x}_{p,i}) - \mathbf{u}_{p,i}}{\tau_p} H(\epsilon - |\mathbf{x}_{p,i} - \mathbf{x}|), \tag{2.4}$$

where H is the Heaviside function, m_p is the particle mass, and v_ϵ is the volume of a sphere of radius ϵ. The averaging radius ϵ is typically chosen to be one grid cell in numerical computations using the LE formalism, but does not need to be specified here, other than satisfying the requirement that ϵ be small. Equations (2.2)–(2.4), together with the fluid incompressibility condition $\nabla\cdot\mathbf{u} = 0$, form the Lagrangian-Eulerian equations. These can now be statistically averaged using methods motivated from kinetic theory to derive the two-fluid formalism.

2.1.2 Two-fluid formalism

We first define the local mass density of particles ρ_p and corresponding velocity $\mathbf{u}_p$, averaged in a small volume centered around the position $\mathbf{x}$ as

$$\rho_p = \frac{m_p}{v_\epsilon}\sum_{i=1}^{N_p} H(\epsilon - |\mathbf{x}_{p,i} - \mathbf{x}|), \qquad \mathbf{u}_p(\mathbf{x}) = \frac{1}{v_\epsilon}\sum_{i=1}^{N_p} \mathbf{u}_{p,i} H(\epsilon - |\mathbf{x}_{p,i} - \mathbf{x}|). \tag{2.5}$$

Applying this average to the particle evolution equations in (2.2) (as done in Ishii & Mishima, 1984, for instance), we approximately get

$$\frac{D_p\mathbf{u}_p}{D_p t} = \frac{\mathbf{u} - \mathbf{u}_p}{\tau_p} + \mathbf{g} + ... \tag{2.6}$$

where $D_p/D_pt = \partial/\partial t + \mathbf{u}_p \cdot \nabla$ is the derivative following the mean particle velocity. The evolution equation for the particle density can be obtained by mass conservation to be

$$\frac{\partial \rho_p}{\partial t} + \nabla \cdot (\rho_p \mathbf{u}_p) = ... \tag{2.7}$$

In both equations, dots on the right hand side result from three possible sources: (1) dispersion in both mass and momentum conservation equations due to the fact that $\mathbf{u}_{p,i} \neq \mathbf{u}_p$; (2) unaccounted for interactions of the particles with the fluid, which include Brownian motions for very small particles, and self-interaction of the particle with its own wake if the latter is not perfectly modeled by the Stokes solution; and (3) long-range interactions of particles with one another due to each other's wakes. Aside from Brownian motions, these terms are generally very difficult to model, leading to strong anisotropic dispersion, and likely to depend nonlinearly on the mean particle density and velocity.

In what follows, we will model these terms for simplicity as $\nu_p \nabla^2 \mathbf{u}_p$ in the momentum equation and $\kappa_p \nabla^2 \rho_p$ in the density equation, so

$$\frac{\partial \mathbf{u}_p}{\partial t} + \mathbf{u}_p \cdot \nabla \mathbf{u}_p + \frac{\mathbf{u}_p - \mathbf{u}}{\tau_p} - \mathbf{g} = \nu_p \nabla^2 \mathbf{u}_p, \tag{2.8}$$

$$\frac{\partial \rho_p}{\partial t} + \nabla \cdot (\rho_p \mathbf{u}_p) = \kappa_p \nabla^2 \rho_p. \tag{2.9}$$

These terms are included to stabilize the numerical scheme in the DNSs, although they are also physically motivated in the limit where Brownian motion is the dominant source of dispersion. Note that we anticipate the two-fluid approach to break down when the Stokes number (the ratio of the stopping time to the eddy turnover time) approaches unity, in which case the particles become uncorrelated with the fluid and therefore also with one another (Shotorban & Balachandar, 2006). When this happens, the mean particle velocity $\mathbf{u}_p$ is no longer a good

approximation for each individual particle velocity, and the averaging procedure becomes meaningless.

To couple the particle and fluid evolution equations, note that the drag term in the continuum limit in (2.3) becomes

$$\mathbf{F}_p(\mathbf{x}) = \rho_p(\mathbf{x})\frac{\mathbf{u}_p(\mathbf{x}) - \mathbf{u}(\mathbf{x})}{\tau_p}, \tag{2.10}$$

so the two-way coupled equations are

$$\rho_f\left(\frac{\partial \mathbf{u}}{\partial t} + \mathbf{u}\cdot\nabla\mathbf{u}\right) = -\nabla p + \rho\mathbf{g} + \rho_p\frac{\mathbf{u}_p - \mathbf{u}}{\tau_p} + \rho_f\nu\nabla^2\mathbf{u}, \tag{2.11}$$

$$\frac{\partial \mathbf{u}_p}{\partial t} + \mathbf{u}_p\cdot\nabla\mathbf{u}_p + \frac{\mathbf{u}_p - \mathbf{u}}{\tau_p} - \mathbf{g} = \nu_p\nabla^2\mathbf{u}_p, \tag{2.12}$$

$$\frac{\partial \rho_p}{\partial t} + \nabla\cdot(\rho_p\mathbf{u}_p) = \kappa_p\nabla^2\rho_p, \tag{2.13}$$

$$\nabla\cdot\mathbf{u} = 0. \tag{2.14}$$

It is worth noting that in this limit, we are able to account for the inertial clustering of particles since the particle velocity field $\mathbf{u}_p$ is not required to be divergence-free (i.e. $\rho_p\nabla\cdot\mathbf{u}_p$ is not necessarily zero in eqn. 2.13). Moreover, for smaller particles that are well-coupled to the fluid, the two-fluid formalism recovers the equilibrium Eulerian formalism in which particle inertia is negligible. We can demonstrate this by taking the formal limit $\tau_p \to 0$ to obtain:

$$\mathbf{u}_p = \mathbf{u} - w_s\hat{\mathbf{e}}_z, \tag{2.15}$$

$$\rho_f\left(\frac{\partial \mathbf{u}}{\partial t} + \mathbf{u}\cdot\nabla\mathbf{u}\right) = -\nabla p + (\rho + \rho_p)\mathbf{g} + \rho_f\nu\nabla^2\mathbf{u}, \tag{2.16}$$

$$\frac{\partial \rho_p}{\partial t} + (\mathbf{u} - w_s\hat{\mathbf{e}}_z)\cdot\nabla\rho_p = \kappa_p\nabla^2\rho_p, \tag{2.17}$$

$$\nabla\cdot\mathbf{u} = 0, \tag{2.18}$$

where the settling velocity w_s is related to the stopping time and gravity via $w_s = \tau_p g$. The particle velocity $\mathbf{u}_p$ is now determined by the carrier fluid velocity and the particle settling velocity. Compared to the two-fluid formalism, we see that $\nabla \cdot \mathbf{u}_p \equiv 0$; thus, the particle concentration is solely advected by the carrier flow. As a result, preferential concentration cannot be captured by the equilibrium Eulerian approach (Maxey & Riley, 1983).

2.2 Advantages of the two-fluid formalism

Due to the continuum treatment of the dispersed phase, the two-fluid formalism (as well as the Equilibrium Eulerian formalism) has a number of computational and analytical advantages over the Lagrangian and fully-resolved formalisms. First we can easily extract averaged particle properties over a small control volume (e.g. particle concentration and particle velocity) in the two-fluid formalism, whereas extracting the same properties with point (or fully-resolved) particles is not as straightforward. Moreover computational load imbalances that occur in highly concentrated regions when tracking individual particles is not an issue in the two-fluid approach. Furthermore if needed, a linear stability analysis can be used to study the stability properties of the two-phase system. At the same time, an advantage of using the two-fluid formalism over the Equilibrium Eulerian approach is that inertial particles can be modeled, and thus, regions of significant particle concentration enhancement due to preferential concentration can be captured. Generally speaking when using the two-fluid formalism, the restrictions on the Stokes number is much more relaxed with $St \lesssim O(1)$.

2.3 Numerical implementation

In order to investigate the nonlinear dynamics of turbulent particle-laden flows using the two-fluid equations, we use the highly scalable, triply periodic code PADDI (Stellmach et al., 2011; Traxler et al., 2011b) which was originally used to study fingering convection and thermohaline staircases (in oceanic contexts). There exist other versions of the code that have been used to study sedimentary convection (Reali et al., 2017; Ouillon et al., 2020) and astrophysical instabilities (Moll et al., 2016; Garaud & Kulenthirarajah, 2016; Harrington & Garaud, 2019). In this section, we describe the modifications that were made to the original version of PADDI to incorporate inertial particles. This mainly consisted of adding the two-fluid equations by incorporating the particle momentum and transport equations and modifying the I/O subroutines to include particle information.

2.3.1 Structure of PADDI-2F

The version of the code that we use is referred to as PADDI-2F, which models the evolution of inertial particles in an incompressible flow. The physical system modeled by PADDI-2F includes an incompressible fluid under the Boussinesq approximation, along with equations for the particle field:

$$\frac{\partial \mathbf{u}}{\partial t} + \mathbf{u}\cdot\nabla\mathbf{u} = -\tilde{\nabla}p + D_{visc}\nabla^2\mathbf{u} + R_{part}\left(r\frac{\mathbf{u}_p - \mathbf{u}}{T_p}\right), \tag{2.19}$$

$$\frac{\partial \mathbf{u}_p}{\partial t} + \mathbf{u}_p\cdot\nabla\mathbf{u}_p = \frac{\mathbf{u} - \mathbf{u}_p}{T_p} - G_p\hat{\mathbf{e}}_z + D_{visc,part}, \tag{2.20}$$

$$\frac{\partial r}{\partial t} + \nabla\cdot(\mathbf{u}_p r) = D_{part}\nabla^2 r, \tag{2.21}$$

$$\nabla\cdot\mathbf{u} = 0. \tag{2.22}$$

Note that a temperature equation can also be added if required.

Table 2.1: Description of input parameters in PADDI-2F in Eqs. (2.19)–(2.22).

Parameter	Description
D_{visc}	Fluid velocity diffusion coefficient
$D_{visc,part}$	Particle velocity diffusion coefficient
D_{part}	Particle concentration diffusion coeff.
R_{part}	Particle mass loading parameter
T_{part}	Particle stopping time
G_p	Gravity parameter

The particle equations are represented by (2.20)-(2.21), and the back reaction of the particles is accounted for in the drag term found in the fluid momentum equation (2.19). The code is written with generalized input parameters that are highlighted in blue, so that the user has the freedom to select their own nondimensionalization (see Table 2.1 for their definitions). The equations are solved on a Cartesian grid with periodic boundary conditions, where the domain in physical space is defined as

$$\Omega = \begin{cases} (0, L_x) \times (0, L_y) \times (0, L_z) & \text{(3D case)}, \\ (0, L_x) \times (0, L_y) & \text{(2D case)}. \end{cases}$$

The resolution is specified by the user with the number of grid points in the $x-$,$y-$, and $z-$directions N_x, N_y, and N_z, respectively. Furthermore, the state variables are initialized by the user with their choice for $\mathbf{u}(\mathbf{x}, 0)$, $\mathbf{u}_p(\mathbf{x}, 0)$, and $r(\mathbf{x}, 0)$

PADDI-2F solves the governing equations (2.19)-(2.22) in spectral space, which has the advantage of providing a high degree of accuracy and can significantly accelerate the calculation when using fast Fourier transforms as we do here (for more details, see Stellmach & Hansen, 2008). Diffusion terms are treated implicitly in spectral space, whereas the nonlinear and drag terms are first computed in

physical space, transformed into spectral space, and then, integrated explicitly using a third-order Adams-Bashforth backward-differentiation scheme (where this spectral method is covered in Peyret, 2002; Canuto et al., 2007).

Furthermore, system diagnostics are computed and written to various external output files, which are printed periodically at designated timesteps provided by the user. These files include global diagnostics (such as volume averaged kinetic energy, minimum and maximum velocities, etc.), vertical profiles (i.e. horizontally averaged quantities), and energy spectra which have all been modified to include relevant particle data in PADDI-2F.

2.3.2 Details of the integration scheme

Several numerical choices for the implementation of the two-fluid equations in PADDI-2F are worth mentioning here. First we incorporate the drag term found in Eqs. (2.19)-(2.20) in a way to guarantee that momentum is conserved. For each time step, the drag term is computed using the fluid and particle velocities of the latest iteration and is stored in physical space. In this manner, the drag term used to advance either the fluid and particle momentum equations will remain consistent.

The fluid momentum equation (2.19) is integrated in spectral space with the following scheme. First, note that we can apply the vector identity

$$\mathbf{u} \cdot \nabla \mathbf{u} = (\nabla \times \mathbf{u}) \times \mathbf{u} + \frac{1}{2} \nabla |\mathbf{u}|^2, \tag{2.23}$$

to the advection term in Eq. (2.21). The fluid momentum equation can then be recast as

$$\frac{\partial \mathbf{u}}{\partial t} + (\nabla \times \mathbf{u}) \times \mathbf{u} = -\nabla q + D_{visc} \nabla^2 \mathbf{u} + \mathbf{F}, \tag{2.24}$$

where the terms on right-hand side include the diffusion and body force terms $\mathbf{F}$ along with the total pressure

$$q = p + \frac{1}{2}|\mathbf{u}|^2. \tag{2.25}$$

In spectral space, Eq. (2.24) can be written as a set of ODEs for each wavenumber $\mathbf{k}$ as

$$\left(\frac{\partial}{\partial t} - D_{visc}|\mathbf{k}|^2\right)\tilde{\mathbf{u}}_\mathbf{k} = -i\mathbf{k}\tilde{q}_\mathbf{k} - \tilde{\xi}_\mathbf{k} + \tilde{\mathbf{F}}_\mathbf{k}, \tag{2.26}$$

where the accented terms are spectral space representations of the variables previously written in physical space, and $\tilde{\xi}_\mathbf{k}$ is the transform of $(\nabla \times \mathbf{u}) \times \mathbf{u}$.

To ensure that the divergence-free condition for the fluid velocity is satisfied, the code uses what is referred to as "divergence cleaning" by adjusting the total pressure q accordingly. To see this, we first take the divergence of the fluid momentum equation (2.19) and use the property that $\nabla \cdot \mathbf{u} = 0$ to obtain

$$\nabla \cdot [(\nabla \times \mathbf{u}) \times \mathbf{u}] = -\nabla^2 q + \nabla \cdot \mathbf{F}. \tag{2.27}$$

Transforming (2.27) into spectral space and solving for the pressure term yields

$$\tilde{q}_\mathbf{k} = \frac{i\mathbf{k}\tilde{\mathbf{F}}_\mathbf{k} - i\mathbf{k}\tilde{\xi}_\mathbf{k}}{|\mathbf{k}|^2}, \tag{2.28}$$

which now shows what is required (and computed in PADDI-2F) to guarantee incompressibility.

The particle momentum equation (2.20) is transformed similarly to the fluid momentum equation without the added "divergence cleaning" step since the pressure term is not present. Using the same vector identity introduced in (2.23) for

$\mathbf{u}_p \cdot \nabla \mathbf{u}_p$, we then rewrite the particle momentum equation as

$$\frac{\partial \mathbf{u}_p}{\partial t} + (\nabla \times \mathbf{u}_p) \times \mathbf{u}_p + \frac{1}{2}\nabla |\mathbf{u}_p|^2 = D_{visc,part} \nabla^2 \mathbf{u}_p + \mathbf{F}_p, \tag{2.29}$$

where $\mathbf{F}_p$ includes the forces due to gravity and drag.

We then write Eq. (2.29) as a set of equations in spectral space for each wavenumber $\mathbf{k}$ as

$$\left(\frac{\partial}{\partial t} - D_{visc,part} |\mathbf{k}|^2 \right) \tilde{\mathbf{u}}_{p,\mathbf{k}} = -\tilde{\xi}_{p,\mathbf{k}} + \tilde{\mathbf{F}}_{p,\mathbf{k}}, \tag{2.30}$$

where $\tilde{\xi}_{p,\mathbf{k}}$ is the transform for $(\nabla \times \mathbf{u}_p) \times \mathbf{u}_p + \nabla |\mathbf{u}_p|^2/2$.

Lastly, the advection–diffusion equation (2.21) for the particle concentration is written in spectral space as

$$\left(\frac{\partial}{\partial t} - D_{part} |\mathbf{k}|^2 \right) \tilde{r}_{\mathbf{k}} = -\tilde{\xi}_{r,\mathbf{k}}, \tag{2.31}$$

where $\tilde{\xi}_{r,\mathbf{k}}$ is the transform for $\nabla \cdot (\mathbf{u}_p r)$.

Once the equations are transformed in spectral space (as shown for the fluid velocity in Eq. 2.26, the particle velocity in Eq. 2.30, and the particle concentration in Eq. 2.31), we integrate the ODEs using an Adams-Bashforth backward-differentiation scheme with adaptive timestepping, with an additional condition so that the timestep cannot be larger than the particle stopping time.

We also note that as a result of modeling inertial particles that have a tendency to strongly concentrate in some regions of the fluid, one must account for a higher resolution in the code to avoid numerical instability. If the resolution is not sufficiently large, Gibbs oscillations are generated, and the particle concentration can be over- or underestimated (i.e. mass is not conserved). In all the simulations

presented in this thesis, we have ensured that the resolution is high enough to avoid Gibbs oscillations almost all of the time. However, they are very occasionally observed in a few of the simulations with large Stokes number. To ensure mass conservation despite these oscillations, we begin by measuring the total mass of the particles M_{init} at time $t = 0$. For each time step, we track the value of the current mass M_{curr} to ensure that mass is conserved ($M_{curr} = M_{init}$). In most cases, this condition is satisfied at each time step. However, lower resolution can induce the Gibbs phenomenon shown by Figure 2.1(a). This leads to regions of negative particle density which are unphysical, and $M_{curr} \neq M_{init}$. In the code, we remove the negative particle density regions depicted in 2.1(b) and multiply this now non-negative particle density by M_{init}/M_{curr}. In this manner, particle mass will be conserved during the simulation. Note that this "fix" is not necessary as long as the simulations are well-resolved, but is introduced to reduce errors in the rare occasions where the system does become under-resolved.

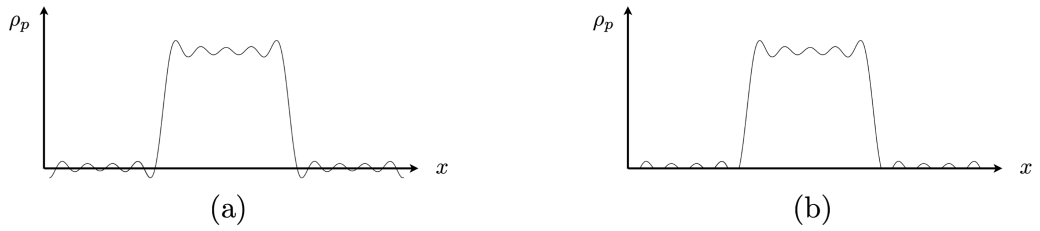

Figure 2.1: The schematic shows how we conserve mass in simulations. We measure the total mass of the particles M_{init} at time $t = 0$. If the resolution is not large enough to resolve simulations, we can encounter the Gibbs phenomenon (a), which may over- or under-estimate ρ_p in our system. We first correct this by removing negative values of ρ_p (b). Then, we adjust the particle density to M_{init} (not shown).

2.4 Thesis Outline

Preferential concentration of turbulent flows is abundant in a number of physical and industrial applications. Examples of these processes include droplet growth in clouds, sediment transport in turbidity currents, aerosol deposition in pharmaceutical sprays, and dust agglomeration in accretion disks. Although preferential clustering has been studied thoroughly in the past several decades, much less has been done in characterizing typical particle sizes and predicting the resulting particle concentration enhancement. In this thesis, we aim to answer these questions using various analytical methods such as dominant balance and asymptotic analysis as well as employing and analyzing numerical simulations using the two-fluid equations. We restrict our investigation to dilute suspensions of heavy, inertial particles whose motion follows Stokes' drag.

In Chapter 3, we study the evolution of particle concentration enhancement in the particle-induced Rayleigh-Taylor instability. The model setup consists of an unstable particle layer settling in a carrier fluid with a stable background temperature gradient. Using 2D Direct Numerical Simulations (DNSs), we conduct a systematic exploration of the parameter space to study the evolution of the bulk of the particle layer where preferential concentration is most effective. Motivated by arguments of dominant balance based on the two-fluid equations, we then find scaling laws to predict the maximum and typical particle concentration enhancement over the mean.

In Chapter 4, we investigate whether the results from Chapter 3 are also applicable in the presence of mechanically driven turbulence. We initialize the system with a uniform distribution of particles and drive the mean flow with an applied body force to render the system shear-unstable. We then use 3D DNSs to investigate preferential concentration once the system has reached a statistically

state. We confirm that the scaling laws that predict the maximum and typical particle concentration enhancement over the mean also apply in a system in which the turbulence is mechanically driven.

In Chapter 5, we aim to characterize clusters from the 3D DNSs presented in Chapter 4. In order to do so, we use a box counting method which first identifies clusters, and then extracts topological attributes such as cluster mass, thickness, and shape. We then analyze probability distribution functions of cluster properties to elucidate the results found in Chapter 4, and deduce properties of these clusters that may help better understand collisional growth in clouds and accretion disks, for instance.

Finally in Chapter 6, we summarize the results of this thesis and conclude with potential ideas for future work.

Chapter 3

Preferential concentration in the particle-induced convective instability

This chapter is composed of a reprint of Nasab & Garaud (2020) published in Physical Review Fluids (Vol. 5, Iss. 11 November 2020). A section of this reprint has been moved earlier in the document, and its contents can now be found in Section 2.1. Further changes to this chapter are marked in italics.

3.1 Introduction

Preferential concentration is the tendency for heavy particles to accumulate in regions of high strain rate and low vorticity due to their inertia (Csanady, 1963; Meek & Jones, 1973; Maxey, 1987). Investigations of the process date back to the 1980s and were performed using numerical experiments (Maxey & Corrsin, 1986; Squires & Eaton, 1991; Elghobashi & Truesdell, 1992) and laboratory experiments (Fessler et al., 1994; Kulick et al., 1994). For comprehensive reviews of the topic,

see for instance (Eaton & Fessler, 1994; Crowe et al., 1996; Balachandar & Eaton, 2010; Monchaux et al., 2012) and references therein.

Today, thanks to progress in high-performance computing, Direct Numerical Simulations (DNSs) are a particularly convenient tool for quantifying preferential concentration in particle-laden flows. A variety of techniques can be used, which can be loosely classified into two distinct approaches: the Lagrangian-Eulerian and Eulerian-Eulerian approaches (see Sections 2.1.1–2.1.2 for more detail). The Lagrangian-Eulerian (LE) approach is named for the fact that the particles are evolved individually by integrating their equations of motion, while the carrier fluid is evolved on an Eulerian mesh. Various degrees of sophistication exist, depending on whether the particles are modeled realistically using, for instance, immersed boundary techniques (Mittal & Iaccarino, 2005), or in a simplified way, as point particles (Toschi & Bodenschatz, 2009). In the latter case, particles can either be passively advected, or can react back on the fluid through drag. When particles are modeled exactly, the LE approach is capable of modeling particle-particle interactions, such as collisions. Otherwise, these interactions must be accounted for using simplified parameterizations instead. However, as the number of particles increases, the computational cost can be expensive. In the Eulerian-Eulerian (EE) approach by contrast, the particles are treated as a continuum field with its own momentum and mass conservation laws, which are evolved on an Eulerian mesh (Elghobashi, 1994; Crowe et al., 1996; Morel, 2015). Within the EE framework, various levels of approximation exist depending on the size of the particles, ranging from the so-called equilibrium Eulerian limit (Ferry & Balachandar, 2002; Ferry et al., 2003) in which particle inertia is neglected, to the two fluid limit (Elghobashi & Abou-Arab, 1983; Druzhinin & Elghobashi, 1998) which remains valid for somewhat larger particles.

In regions of the fluid that experience strong local enhancement in the particle number density, increased collision rates can result in rapid particle growth (Cuzzi et al., 2001). As such, preferential concentration is thought to play an important role in controlling the size distribution function of particles suspended in turbulent fluids. Prior works have focused on certain aspects of preferential concentration such as the enhancement of the particle settling velocity (Aliseda et al., 2002; Maxey, 1987; Wang & Maxey, 1993; Mei, 1994; Yang & Lei, 1998; Bosse et al., 2006), the resulting geometry of the dense particle clusters (Cuzzi et al., 2001; Monchaux et al., 2010; Goto & Vassilicos, 2006), and the underlying mechanisms responsible for inertial clustering of particles (Raju & Meiburg, 1995; Obligado et al., 2014; Goto & Vassilicos, 2008; Coleman & Vassilicos, 2009). Preferential concentration likely plays a key role in the warm rain formation in clouds (Pinsky & Khain, 2002; Falkovich et al., 2002; Riemer & Wexler, 2005), protoplanetary disks (Klahr & Henning, 1997; Chambers, 2010; Cuzzi et al., 2008), estuaries (Eisma, 1991; Voulgaris & Meyers, 2004), and industrial applications such as sprays (Cao et al., 2000; Vié et al., 2015). In all of these examples, some of the key questions that remain to be answered are: (1) What is the maximum particle concentration enhancement that can be achieved anywhere in the fluid? (2) What is the typical probability distribution of the volume density of particles? And, (3) how do these quantities depend on the turbulent properties of the carrier flow?

While these questions have been primarily investigated in forced turbulent flows so far (Squires & Eaton, 1991; Eaton & Fessler, 1994; Bosse et al., 2006), they have not been studied extensively to our knowledge in the context of particle-induced buoyancy instabilities (e.g. convective or Rayleigh-Taylor). Such instabilities are particularly relevant in particle-laden turbidity currents, which play an important role in sediment transport (Meiburg & Kneller, 2010). Although most

research to date on particle-laden buoyancy-driven flows has been performed using in-situ or laboratory experiments (Hoyal et al., 1999; Maxworthy, 1999; Parsons et al., 2001; Völtz et al., 2001), numerical experiments have only recently begun to be used in this context. The focus of these numerical studies can be categorized into two groups: (1) numerical tests, in which various formalisms (i.e. LE versus EE) are compared to one another (Chou et al., 2014a,a; Chou & Shao, 2016), and (2) application-driven studies, that investigate, for instance, how the rate of sedimentation is influenced by particle properties. It was shown that both particle size and particle volume fraction can control the resulting modes of instability (i.e. leaking, fingering, stable settling modes) from the initial RT instability configuration, affecting the subsequent evolution of the sedimentation process (Burns & Meiburg, 2012, 2015; Shao et al., 2017). However, numerical investigations whose primary focus is on preferential concentration in the particle-driven convective instability, specifically for two-way coupled systems, have not been performed.

In this paper, we therefore study preferential concentration in the two-way coupled two-fluid formalism using DNSs of particle-driven convective instabilities. *The original paper contained a section on the derivation of the two fluid formalism, that is now located in Chapter 2 of this thesis.* In Section 3.2, we introduce our model setup and its governing equations. In Section 3.3, we present the results of the DNSs and investigate how certain parameters influence preferential concentration and the underlying turbulence. In Section 3.4, we present a predictive model that captures maximum particle concentration enhancement as a function of time and space. In Section 3.5, we look at the probability distribution function (PDF) of the relative particle concentration. Section 3.6 summarizes our results and discusses them in the context of geophysical and astrophysical applications of particle-laden flows.

3.2 The Model

3.2.1 Model set-up

We investigate particle-driven convective instabilities in a dilute suspension using the two-fluid equations. For convenience, we rescale the particle density with the mean density of the fluid, which defines $r = \rho_p/\rho_f$. Having assumed that $\rho_s \gg \rho_f$, it is still possible to have r of order unity even though the volume fraction of particles is assumed to be very small. We assume that the carrier fluid has a constant stable background temperature gradient $T_{0z} > 0$ in the vertical direction, with the background temperature profile given by $T_0(z) = T_m + zT_{0z}$. This assumption was originally motivated by applications in which the carrier fluid is typically stratified, such as in warm clouds or rivers, but does not directly impact the results presented in this paper. Perturbations in the density of the carrier fluid ρ are caused by temperature fluctuations T around that background profile, and are related via $\rho/\rho_f = -\alpha T$, where $\alpha = -\rho_f^{-1}(\partial\rho/\partial T)$.

In the limit of the Boussinesq approximation, the governing dimensional equations are then

$$\frac{\partial \mathbf{u}}{\partial t} + \mathbf{u}\cdot\nabla\mathbf{u} = -\frac{\nabla p}{\rho_f} + \alpha g T\hat{\mathbf{e}}_z + r\frac{\mathbf{u}_p - \mathbf{u}}{\tau_p} + \nu\nabla^2\mathbf{u}, \tag{3.1}$$

$$\frac{\partial \mathbf{u}_p}{\partial t} + \mathbf{u}_p\cdot\nabla\mathbf{u}_p = \frac{\mathbf{u} - \mathbf{u}_p}{\tau_p} + \mathbf{g} + \nu_p\nabla^2\mathbf{u}_p, \tag{3.2}$$

$$\frac{\partial r}{\partial t} + \nabla\cdot(\mathbf{u}_p r) = \kappa_p\nabla^2 r, \tag{3.3}$$

$$\frac{\partial T}{\partial t} + \mathbf{u}\cdot\nabla T + wT_{0z} = \kappa_T\nabla^2 T, \tag{3.4}$$

$$\nabla\cdot\mathbf{u} = 0, \tag{3.5}$$

where $\mathbf{u} = (u, v, w)$ and $\mathbf{u}_p = (u_p, v_p, w_p)$.

Using this system of equations, we shall study the evolution of the relative particle density r. To do so in the context of the convective instability, we start with initial conditions that take the form of a Gaussian profile of amplitude r_0 and width σ:

$$r(x, y, z, 0) = r_0 \exp\left[\frac{(z - L_z/2)^2}{2\sigma^2}\right], \tag{3.6}$$

to which low amplitude random fluctuations are added, and where L_z is the height of the computational domain. The initial particle velocity is set to be the particle settling velocity w_s, while the carrier fluid is initialized with zero velocity.

3.2.2 Non-dimensionalization

We define the units of length $[l]$, relative particle concentration $[r]$, and temperature $[T]$ as

$$[l] = \sigma, \quad [r] = r_0, \quad [T] = \sigma T_{0z}. \tag{3.7}$$

We can define a characteristic velocity for the fluid by identifying its kinetic energy with an estimate of the potential energy of the unstable particle density distribution:

$$[u] = \sqrt{r_0 g \sigma}. \tag{3.8}$$

The characteristic distance and velocity can finally be used to construct a typical convective eddy turnover time

$$[t] = \left(\frac{\sigma}{r_0 g}\right)^{1/2}. \tag{3.9}$$

Thus, the non-dimensional equations are:

$$\frac{\partial \mathbf{u}}{\partial t} + \mathbf{u} \cdot \nabla \mathbf{u} = -\nabla p + R_\rho T \hat{\mathbf{e}}_z + \frac{1}{Re} \nabla^2 \mathbf{u} + r_0 \left(r \frac{\mathbf{u}_p - \mathbf{u}}{T_p} \right), \tag{3.10}$$

$$\frac{\partial \mathbf{u}_p}{\partial t} + \mathbf{u}_p \cdot \nabla \mathbf{u}_p = \frac{\mathbf{u} - \mathbf{u}_p}{T_p} - \frac{1}{r_0} \hat{\mathbf{e}}_z + \frac{1}{Re_p} \nabla^2 \mathbf{u}_p, \tag{3.11}$$

$$\frac{\partial r}{\partial t} + \nabla \cdot (\mathbf{u}_p r) = \frac{1}{Pe_p} \nabla^2 r, \tag{3.12}$$

$$\frac{\partial T}{\partial t} + \mathbf{u} \cdot \nabla T + w = \frac{1}{Pe_T} \nabla^2 T, \tag{3.13}$$

$$\nabla \cdot \mathbf{u} = 0, \tag{3.14}$$

where all the variables $(\mathbf{u}, \mathbf{u}_p, p, r, T)$ are from here on implicitly non-dimensional, and where the dimensionless parameters are defined as:

$$R_\rho = \frac{\alpha \sigma T_{0z}}{r_0} \qquad Re = \frac{(r_0 g)^{1/2} \sigma^{3/2}}{\nu} \qquad Pe_T = \frac{(r_0 g)^{1/2} \sigma^{3/2}}{\kappa_T}$$

$$T_p = \tau_p \left(\frac{r_0 g}{\sigma} \right)^{1/2} \qquad Re_p = \frac{(r_0 g)^{1/2} \sigma^{3/2}}{\nu_p} \qquad Pe_p = \frac{(r_0 g)^{1/2} \sigma^{3/2}}{\kappa_p}$$

$$W_s = \frac{T_p}{r_0}.$$

Four of these parameters describe diffusive effects: a Reynolds number for the fluid Re, a Reynolds number for the particles Re_p, the particle Péclet number Pe_p, and the temperature Péclet number Pe_T. In the fluid momentum equation, R_ρ is the density ratio, defined by analogy with double-diffusive systems to be the ratio of the density gradient due to temperature stratification αT_{0z} to the density gradient due to particle stratification, here estimated as r_0/σ. In addition, T_p is the non-dimensional stopping time, and W_s is the non-dimensional settling velocity of the particles. Note that our non-dimensionalization defines T_p as the ratio of the particle stopping time to the estimated turnover time of the layer-scale eddies. Thus, by construction, T_p is an estimate of the Stokes number St of the

convectively turbulent flow.

We define the non-dimensional total density (i.e. consisting of the fluid and the particles) in the system as

$$\rho_{tot} = \left(\frac{1}{\alpha \sigma T_{0z}} - z - T \right) + \frac{r}{R_\rho}, \tag{3.15}$$

so the non-dimensional total background density gradient is

$$\frac{d\rho_{tot}}{dz} = -\left(1 + \frac{dT}{dz} \right) + \frac{1}{R_\rho} \frac{dr}{dz}. \tag{3.16}$$

The total density gradient controls the development of the convective instability and, as shown above, is the sum of the density gradient due to the temperature stratification and the density gradient due to the particle stratification. At time $t = 0$, the non-dimensional initial condition for the particle concentration is

$$r(x, z, 0) = e^{-(z - L_z/2)^2/2}. \tag{3.17}$$

The particle density gradient is the most unstable at the lower inflection point of the Gaussian ($z = z_i$) when dr/dz reaches its maximum value, given by

$$\left. \frac{dr}{dz} \right|_{z=z_i} = e^{-1/2}. \tag{3.18}$$

Thus, the total density gradient at the lower inflection point $z = z_i$ at $t = 0$ is

$$\left. \frac{d\rho_{tot}}{dz} \right|_{z=z_i, t=0} = -1 + \frac{e^{-1/2}}{R_\rho}. \tag{3.19}$$

Using this information, we define a Rayleigh number as

$$Ra = \left(\frac{1}{\rho_f} \frac{d\rho_{tot}}{dz}\bigg|_{z=z_i} \right) \frac{g\sigma^4}{\kappa_p \nu}, \tag{3.20}$$

where all the quantities on the right-hand side are dimensional. We can then express (3.20) in terms of the previously defined dimensionless parameters as

$$Ra = \left(\frac{e^{-1/2}}{R_\rho} - 1 \right) RePe_p. \tag{3.21}$$

To ensure that overturning convection (rather than double-diffusive instabilities) takes place in all that follows, we set $R_\rho = 0.5 < e^{-1/2}$. We shall then vary Ra by varying either Re or Pe_p, ensuring in all cases that Ra is sufficiently large for turbulent convection to take place. Finally, the Prandtl number will be fixed and equal to one for the flow to be fairly turbulent for all simulations. This choice fixes the relationship between Re and Pe_T:

$$Pr = \frac{Pe_T}{Re} \equiv 1. \tag{3.22}$$

3.3 Numerical Simulations

Since our goal is to characterize preferential concentration of the particles by the fluid, which is an inherently nonlinear phenomenon, we must use DNSs. In order to do so, we use the triply periodic pseudospectral PADDI code (Stellmach et al., 2011; Traxler et al., 2011b) which has been extensively used to study fingering as well as a number of astrophysical instabilities such as semi-convection and shear (Moll et al., 2016; Garaud & Kulenthirarajah, 2016). A slightly modified version of the code was also used to study fingering convection in the equilibrium

Eulerian regime (Reali et al., 2017). We have modified the PADDI code further by adding a particle field which evolves according to the two fluid equations (3.1) - (3.5), and refer to the new version of this code as PADDI-2F. Salient properties of PADDI, as well as the modifications made to include the two-fluid formalism, are briefly described in Appendix 3.7.

In what follows, we present 2D and 3D simulations with specifications listed in Table 3.2. We limit the exploration of parameter space to $T_p \leq 0.3$ since the two-fluid equations are not representative of the full dynamics for larger T_p (as discussed in Ferry & Balachandar, 2001). As described in Section 2.1.2, Re_p (or ν_p) accounts for the intrinsic dissipation in particle momentum due to Brownian motion and long-range interactions among particles. Since we are focusing our investigation to inertial particles, we can fix $Re_p = 1000$ to be sufficiently large to neglect these dissipative effects for all simulations. The size of the computational domain is selected based on the following considerations: (1) since the code is triply-periodic, the domain height must be sufficiently large to avoid unphysical interactions between the particles that leave the domain at the bottom and re-enter it at the top. With that in mind, we present simulations with height ranging from $L_z = 10$ to $L_z = 20$. (2) The domain width must be chosen to be large enough to ensure that there are enough convective eddies in the horizontal direction to have meaningful statistics. In all the simulations presented below $L_x = 10$, and for 3D simulations, we further choose $L_y = 2$. At this point, we bring attention to the fact that since most simulations will be in 2D, the term "turbulence" is used in a loose sense, to describe the inherent nonlinear and chaotic properties of the flow, rather than in the strict sense.

3.3.1 Two-fluid code validation against Eulerian simulations

To validate the PADDI-2F code, we begin by comparing a two-fluid simulation with low T_p solving equations (3.10)–(3.14) with that of an equilibrium Eulerian simulation solving (2.15)–(2.18) (used in Reali et al., 2017). In both codes, we set $W_s = 0.1, R_\rho = 0.5, Re = 1000, Pr = 1$, $Pe_T = PrRe$, $Re_p = 1000$, and $Pe_p = 1000$ (corresponding to $Ra \approx 10^6$); for the two-fluid simulation, we additionally set the particle stopping time to be $T_p = 0.005$, which should be sufficiently small to be in the limit where the equilibrium Eulerian formalism is valid. We first compare the two codes using 2D simulations (see Section 3.3.4 for a comparison of 2D vs. 3D simulations). We set the resolution of the 2D runs to be 768×1536 equivalent grid points in the $x-$ and $z-$ directions, respectively, and set the domain width and height as $L_x = 10$ and $L_z = 20$.

In the snapshots presented in Figure 3.1, we see the evolution of the particle concentration and the horizontal component of the fluid velocity u in the two-fluid simulation. Snapshots of the Eulerian simulation (not shown) taken at the same times look very similar to the two-fluid simulation (bearing in mind the chaotic nature of the system). The initially unstable total density stratification $\rho_{tot}(z, 0)$ drives the growth of convective eddies, which become visible in the second snapshot ($t = 27$). The particle layer then rapidly spreads vertically under the effect of turbulent mixing in the third snapshot ($t = 40$), reducing the unstable particle gradient. Although there are horizontal inhomogeneities in the particle concentration, these remain small compared with the horizontal mean. In particular, r never exceeds the initial maximum value of one, consistent with the expected properties of an advection-diffusion equation when $\nabla \cdot \mathbf{u}_p \simeq 0$. This shows qualitatively that for sufficiently small T_p, the two-fluid simulation recovers behavior

Figure 3.1: Snapshots of the particle concentration r (top row) and the horizontal component of the fluid velocity u (bottom row) at various times in a two-fluid simulation with $T_p = 0.005$, $W_s = 0.1, R_\rho = 0.5, Re = 1000$, $Re_p = 1000$, $Pe_p = 1000$, and $Pr = 1$.

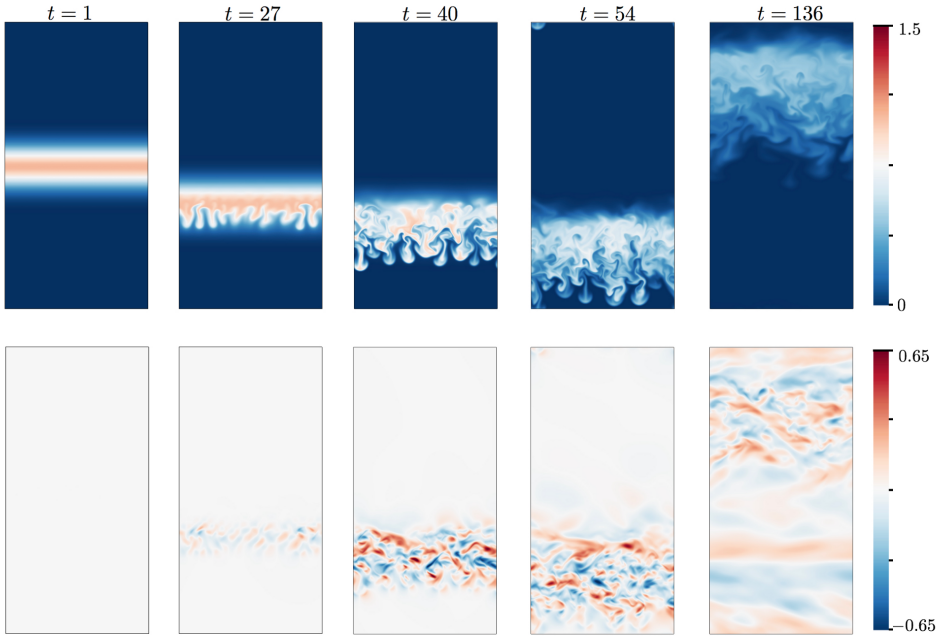

expected in the absence of particle inertia.

We now compare these simulations more quantitatively by examining the behavior of both the particle concentration and the fluid velocity. In order to do so, we define a number of diagnostic quantities (for convenience listed in Table 3.1). We first define the maximum particle concentration and maximum horizontal fluid velocity in the domain at any point in time as

$$r_{sup}(t) = \max_{x,z} r(x, z, t) \quad \text{and} \quad u_{sup}(t) = \max_{x,z} u(x, z, t). \tag{3.23}$$

We have selected to look at the behavior of the horizontal component of the velocity, rather than its vertical component or total amplitude, because it is not directly influenced by the particle settling motion.

Table 3.1: Terms defined from text.

Definition	Description
$\overline{r}(z.t) = \overline{r(x,z,t)} = \frac{1}{L_x}\int r(x,z,t)$	Horizontal average of the particle concentration at a given height at time t.
$r_{max}(z,t) = \max_x r(x,z,t)$	Maximum value of the particle concentration at a given height at time t.
$r_{rms}(z,t) = \left[\overline{[r(x,z,t) - \overline{r}(z,t)]^2}\right]^{1/2}$	Typical enhancement over $\bar{r}$ at a given height at time t.
$u_{rms}(z,t) = [\overline{u(x,z,t)^2}]^{1/2}$	Root mean square of the $x-$component of the fluid velocity at a given height at time t.
$r_{rel}(x,z,t) = \frac{r(x,z,t)}{\bar{r}(z,t)}$	Relative particle concentration at time t.
Extracted in the bulk of the particle layer:	
$z_{max}(t)$	Height corresponding to the maximum value of $\overline{r}$ at time t.
$\overline{r}^*(t) = \overline{r}(z_{max},t)$	Maximum value of $\overline{r}$ at time t.
$u^*_{rms}(t) = u_{rms}(z_{max},t)$	Value of u_{rms} measured at z_{max} at time t.
$r_{sup}(t) = \max_{x,z} r(x,z,t)$	Maximum particle concentration in the domain at time t.
$u_{sup}(t) = \max_{x,z} u(x,z,t)$	Maximum value of the horizontal velocity of the fluid at time t.

In order to study the evolution of the bulk of the particle layer, we next define the horizontally averaged particle concentration profile $\overline{r}(z,t)$, where the overbar denotes a horizontal average, as in $\overline{q}(z,t) = \frac{1}{L_x}\int q(x,z,t)dx$ for any quantity q. The quantity $\overline{r}$ can be compared to the corresponding analytical expression obtained when the particles evolve purely diffusively, namely when

$$\frac{\partial r_{\text{diff}}}{\partial t} - W_s\frac{\partial r_{\text{diff}}}{\partial z} = \frac{1}{Pe_p}\nabla^2 r_{\text{diff}}. \tag{3.24}$$

The solution of (3.24) in an infinite domain with initial condition given by (3.17) is

$$r_{\text{diff}}(z,t) = \frac{1}{\sqrt{\frac{2}{Pe_p}t+1}}\exp\left[-\frac{[z-(L_z/2-W_st)]^2}{2[(2/Pe_p)t+1]}\right]. \tag{3.25}$$

As long as $2t/Pe_p \ll L_z$, this solution is also a good approximation to the diffusive solution in the periodic domain.

We also extract the maximum value of $\overline{r}$ at time t, which occurs at the height $z = z_{max}(t)$

$$\overline{r}^*(t) = \overline{r}(z_{max},t) = \max_z \overline{r}(z,t). \tag{3.26}$$

In what follows, the asterisk will always indicate a quantity measured at the position $z_{max}(t)$. We can compare r_{sup} and $\overline{r}^*$ to the maximum value of the diffusive solution, namely

$$r_{\text{diff,sup}}(t) = \max_z r_{\text{diff}}(z,t) = \frac{1}{\sqrt{\frac{2}{Pe_p}t+1}}. \tag{3.27}$$

Finally, we define the root mean square of the $x-$component of the fluid velocity at a particular height z and time t, expressed as

$$u_{rms}(z,t) = \left[\overline{u(x,z,t)^2}\right]^{1/2}. \tag{3.28}$$

Figure 3.2: Low $T_p = 0.005$ two-fluid simulation versus an equilibrium Eulerian simulation with $W_s = 0.1, R_\rho = 0.5, Re = 1000, Re_p = 1000, Pe_p = 1000$, and $Pr = 1$, comparing various diagnostics of the particle concentration (a) and of the horizontal component of fluid velocity (b).

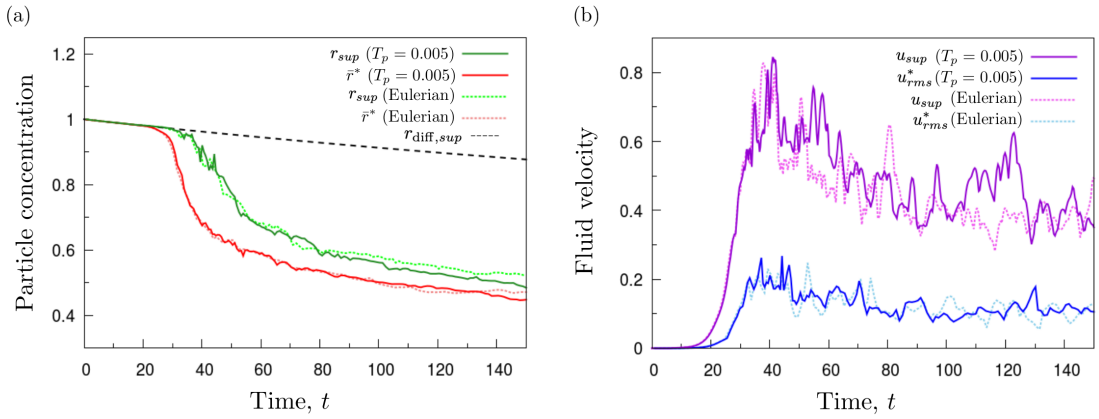

We can study turbulence in the *bulk* of the particle layer over time by extracting the corresponding value of u_{rms} at the position $z = z_{max}$, defined by

$$u^*_{rms}(t) = u_{rms}(z_{max}, t). \tag{3.29}$$

Figure 3.2 shows a comparison of $\overline{r}^*$ and r_{sup} for the particle concentration (Figure 3.2a) and u^*_{rms} and u_{sup} for the fluid velocity (Figure 3.2b) for both the two-fluid and equilibrium Eulerian simulations. Notably, we see that all the measured quantities are statistically consistent with one another in the two cases, verifying that the two-fluid formalism recovers the equilibrium Eulerian formalism for small T_p. At early times ($t = 0-25$) prior to the development of the convective instability, $\overline{r}^*$ and r_{sup} follow the purely diffusive solution $r_{\mathrm{diff,sup}}$, shown as the black dotted line given by (3.27). Later, we see that $\overline{r}^*$ and r_{sup} decrease rapidly (at times $t = 30 - 50$), then more slowly again after $t = 60$. During that time $\overline{r}^*$ and r_{sup} roughly decay at the same rate.

Figure 3.3: Evolution of the mean particle concentration $\overline{r}$ and of the rms fluid velocity u_{rms} (defined in the main text) profiles for the two-fluid $T_p = 0.005$ (red) and equilibrium Eulerian simulations (green) with $W_s = 0.1, R_\rho = 0.5, Re = 1000, Re_p = 1000, Pe_p = 1000$, and $Pr = 1$. The black dotted Gaussian curve (first row) represents the purely diffusive solution (3.25) for comparison.

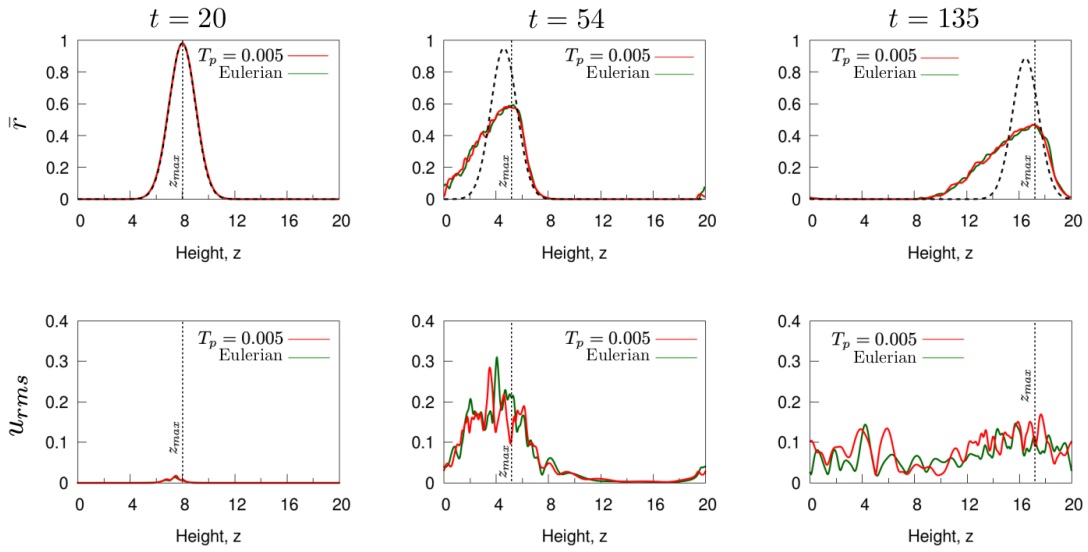

Looking at the eddy velocities, we see that the intermediate phase ($t = 30-60$) corresponds to the peak of the mixing event. The corresponding u_{sup} reaches a maximum value of $u_{sup} \approx 0.8$ with the rms velocity reaching $u^*_{rms} \approx 0.25$. The fact that u_{sup} and u^*_{rms} are both of order unity actually holds for all runs (see later), and proves that the non-dimensionalization selected is appropriate. By $t = 80$, the main mixing event is over and the turbulence (as measured both by u^*_{rms} or u_{sup}) now gradually decays on a much longer timescale.

We can also look at how the particles and the fluid velocity evolve spatially over time. Figure 3.3 shows the profiles of $\overline{r}$ and u_{rms} at three instants in time for both simulations, with the black dotted curve representing r_{diff} (3.25). Recall that the domain is periodic in both directions so the particle layer re-emerges at the top after leaving from the bottom. The dotted vertical line z_{max} marks the position of the maximum of $\overline{r}$. We clearly see that the two-fluid and equilibrium Eulerian simulations behave in a quantitatively similar way. In both cases, the particle layer settles roughly at the expected rate set by the value of W_s, but its vertical density profile $\overline{r}$ becomes asymmetric and wider than in the purely diffusive case (black dotted line). The extended tail of $\overline{r}$ below the bulk of the layer is associated with more rapidly-moving particle-rich plumes that can clearly be seen penetrating into the lower particle-free fluid in Figure 3.1. Focusing on the evolution of the u_{rms} profile, we see that at early times the turbulence develops in the bulk of the particle layer as expected. However, the fluid remains turbulent even after the particles have settled through a region, which explains why the size of the turbulent region is much larger than that of the particle layer at late times (e.g. $t = 135$). This can be understood by noting that the time it takes for turbulent motions to decay viscously is much larger than the time it takes for the particles to settle across the bottom of the box.

This section has illustrated the interplay between the turbulence and the particle field for short stopping times. Both the qualitative and quantitative evidence confirm that the two-fluid model for very low T_p and the equilibrium Eulerian model have similar dynamics, conclusively validating our two-fluid code.

3.3.2 Comparison between low and high T_p simulations

We now look at the effect of larger stopping time on the evolution of the particle layer. We continue to work in 2D and choose $T_p = 0.1$ with the same resolution (i.e. 768×1536 grid points) keeping the remaining parameters and domain size the same as in the simulation from Section 3.3.1 (i.e. $W_s = 0.1, R_\rho = 0.5, Re = 1000$, $Re_p = 1000$, $Pe_p = 1000$, $Pr = 1$; and $L_x = 10$, $L_z = 20$). Snapshots of the particle concentration field as well as the evolution of r_{sup} and $\overline{r}^*$ with time are shown in Figure 3.4. We clearly see the emergence of regions of much higher particle concentration than at low T_p, located in narrow, wisp-like structures (see for instance the snapshot at $t = 54$) with r_{sup} reaching values of as high as 5. The fact that this is much larger than the initial maximum value of r in the domain is a distinct signature of preferential concentration, since this only occurs when $\nabla \cdot \mathbf{u}_p$ is non-zero. This also shows that regions of strongly enhanced particle concentration can develop even when the mean particle concentration in the bulk of the layer is decreasing. After the main mixing event (around $t = 80$), r_{sup} drops again to values that are lower than one, though remains substantially higher than $\overline{r}^*$. This raises the interesting question of what determines the maximum possible value of the particle concentration field at any given time in the simulation (which will be further discussed in Section 3.4).

Turning our attention to the evolution of u_{sup} and u^*_{rms}, we see that for larger T_p at the peak of the mixing event, $u_{sup} \approx 1.1$ and $u^*_{rms} \approx 0.3$, whereas in the

Figure 3.4: Top: Snapshots of the particle concentration r at various times in a simulation with $T_p = 0.1, W_s = 0.1, R_\rho = 0.5, Re = 1000, Re_p = 1000, Pe_p = 1000$, and $Pr = 1$. Bottom: Diagnostic properties of the particle concentration and fluid velocity as a function of time for the same simulation.

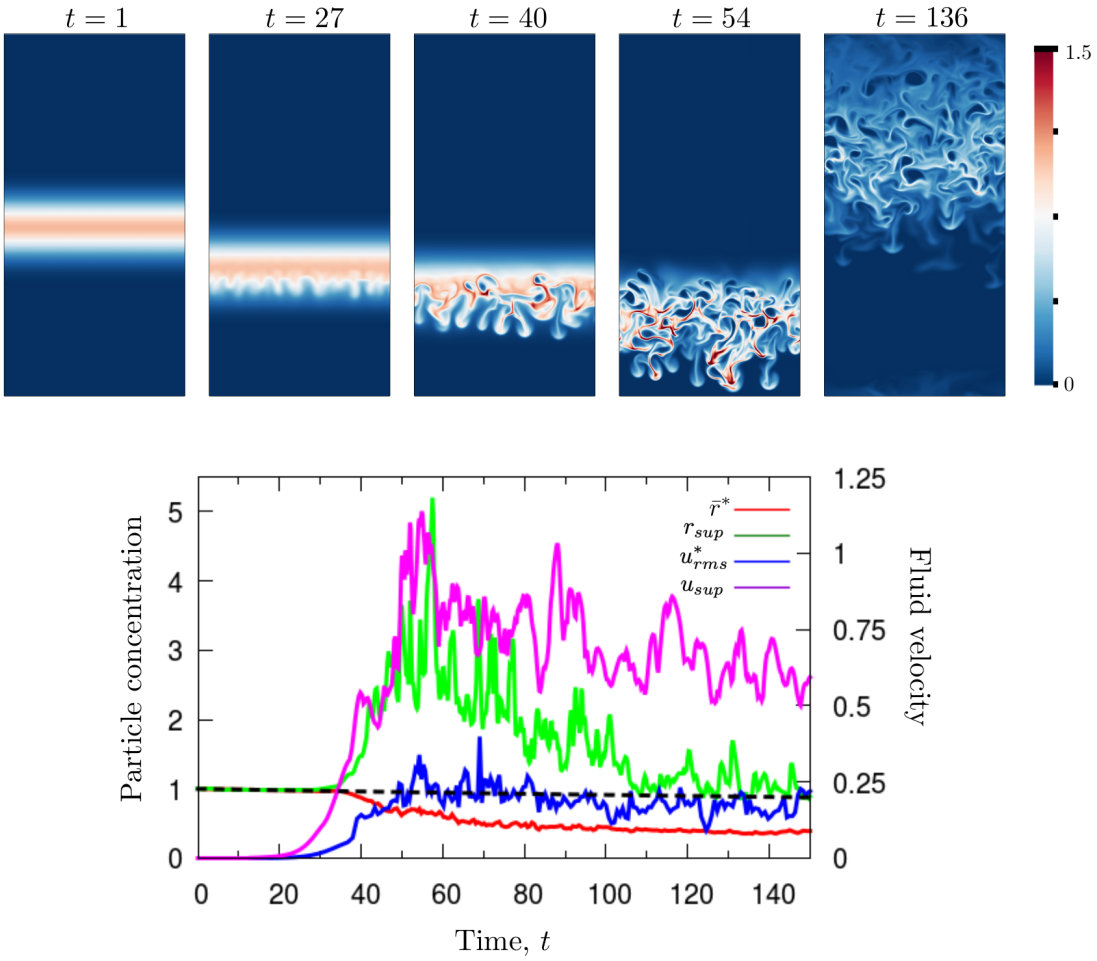

lower T_p case the corresponding values were $u_{sup} \approx 0.8$ and $u^*_{rms} \approx 0.25$. This suggests that T_p does not have a major effect on the turbulence of the system (at least for the parameters explored).

We can measure the maximum particle concentration at a given height in the domain using

$$r_{max}(z,t) = \max_x r(x,z,t). \tag{3.30}$$

In addition, we can also measure the typical (rather than the maximum) enhancement over the mean $\overline{r}$ as a function of height using

$$r_{rms}(z,t) = \left[\overline{[r(x,z,t) - \overline{r}(z,t)]^2}\right]^{1/2}. \tag{3.31}$$

Figure 3.5 compares the maximum particle concentration r_{max} with both the mean particle concentration $\overline{r}$ and one standard deviation above the mean, $\overline{r}+r_{rms}$, as a function of height, for two simulations with $T_p = 0.005$ and $T_p = 0.1$. We see that for both cases, $\overline{r}$ and $\overline{r} + r_{rms}$ have similar profiles. For the low T_p case, $\overline{r} + r_{rms}$ typically remains below one. In addition, the profile of r_{max} also follows that of $\overline{r}$, and lies about two standard deviations above it. As such, it is largest in the bulk of the particle layer. For high T_p, r_{max} is also largest in the bulk of the particle layer, with values peaking at $r_{sup} \approx 2.25$ at this particular instant in time. However, r_{max} is now several standard deviations above $\overline{r}$, implying that the probability density distribution of the particle concentration has a longer tail (see Section 3.5 for more on this point).

Figure 3.6 more generally compares the maximum particle concentration r_{sup} obtained in several simulations with increasing particle stopping time T_p. The simulations continue to be in 2D with 768×1536 grid points, and all other parameters remain unchanged (i.e. $W_s = 0.1, R_\rho = 0.5, Re = 1000, Re_p = 1000, Pe_p =$

Figure 3.5: Measures of particle concentration at $t = 54$ of two-fluid simulations for $T_p = 0.005$ and $T_p = 0.1$ with otherwise identical parameters $W_s = 0.1, R_\rho = 0.5, Re = 1000, Re_p = 1000, Pe_p = 1000$, and $Pr = 1$.

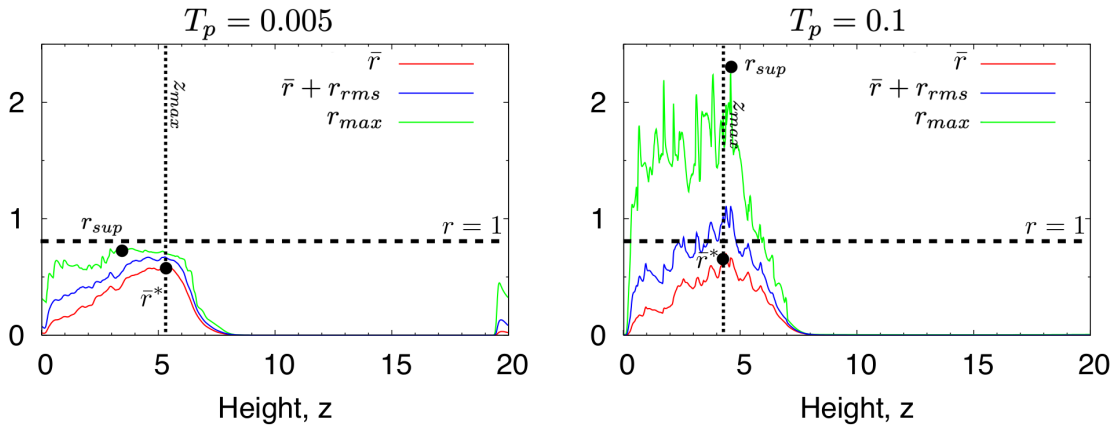

1000, $Pr = 1$). The black dotted line represents $r = 1$. As expected, we find that r_{sup} increases with T_p as a result of preferential concentration. Furthermore, we see that r_{sup} remains above unity for longer times, signifying that dense particle regions persist in the simulations. On the other hand, we find that preferential concentration is negligible for $T_p \leq 0.01$, and r_{sup} is almost indistinguishable from that obtained in the equilibrium Eulerian limit.

3.3.3 Impact of Pe_p and Re

We next look at the impact of the fluid Reynolds number Re and the particle Péclet number Pe_p on the evolution of the particle concentration. We continue to focus on 2D simulations, choosing a relatively large stopping time to ensure that inertial effects are important. We use $T_p = 0.1$ with the remaining parameters and domain size set as $W_s = 0.1, R_\rho = 0.5$, $Pr = 1$, $L_x = 10$, and $L_z = 20$. The resolution selected for these simulations increases with both Re and Pe_p, and is listed in Table 3.2. Figure 3.7 presents snapshots of the particle concentration at $t = 54$ for simulations with Pe_p and Re both varying between 1000 and 10,000.

Figure 3.6: Comparison of r_{sup} for 2D simulations with varying T_p. Remaining parameters: $W_s = 0.1, R_\rho = 0.5, Re = 1000, Re_p = 1000, Pe_p = 1000, Pr = 1$. An equilibrium simulation marked "Eulerian" is shown for comparison.

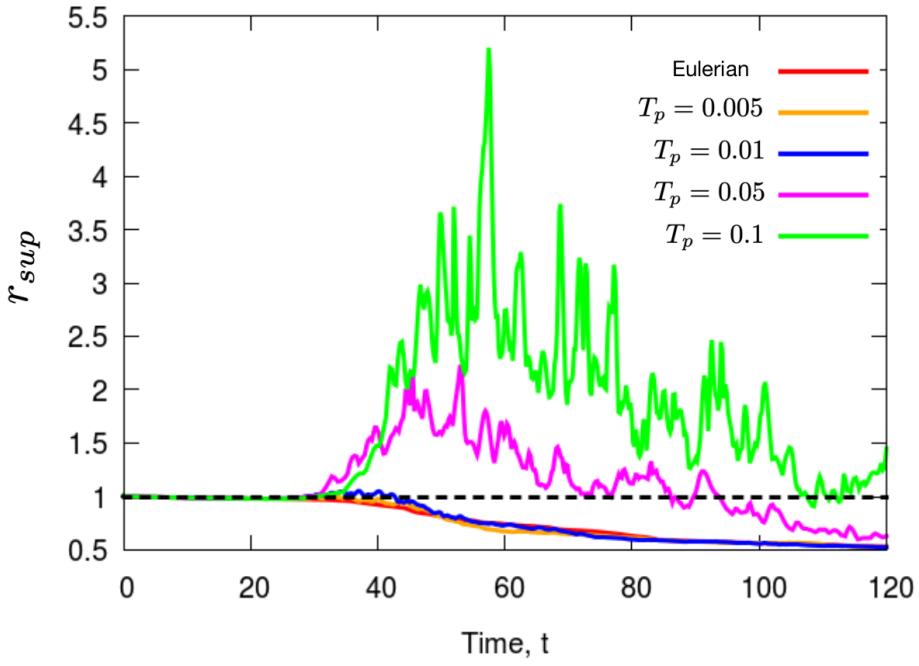

Figure 3.7: Snapshots of the particle concentration field for varying Re and Pe_p with fixed $T_p = 0.1$ taken at $t \approx 54$. Only the vicinity of the particle layer is shown. Remaining parameters: $W_s = 0.1, R_\rho = 0.5, Re_p = 1000, Pr = 1$.

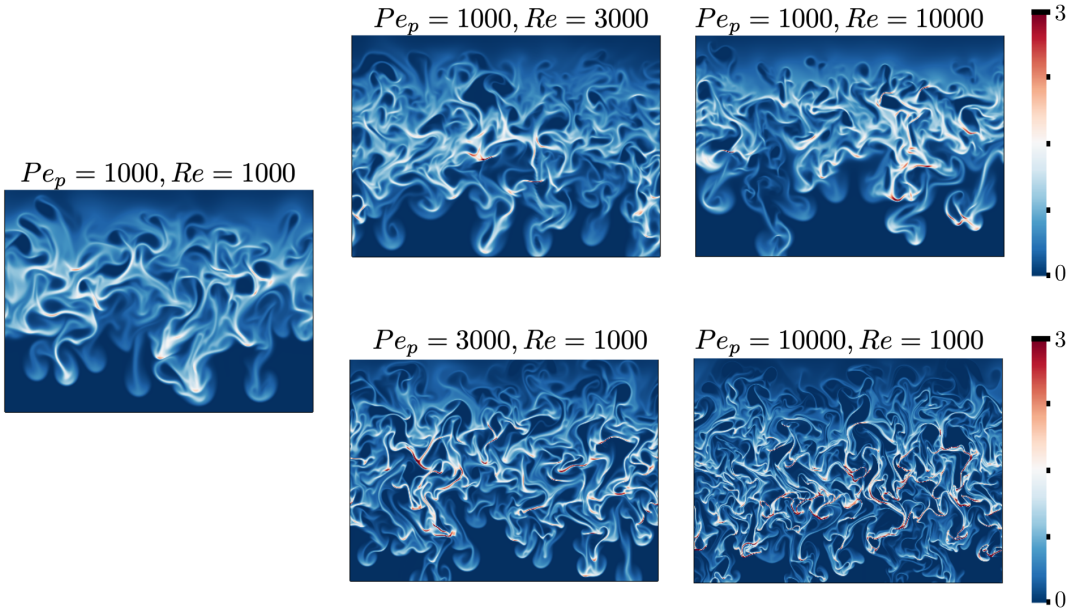

When we fix $Pe_p = 1000$ and increase Re, the particle concentration snapshots appear qualitatively similar, consisting of narrow structures comparable in size and density. The maximum particle concentration enhancement appears relatively unaffected by the fluid viscosity (at least, for this range of Re, and within the context of the two-fluid equations). In contrast, if we fix $Re = 1000$ and increase Pe_p, we see a striking difference in both the geometry of the wisps, as well as the maximum concentration achieved in the wisps. That is, as Pe_p increases, these structures become more numerous and narrower, with a corresponding increase in the maximum particle concentration.

These qualitative trends are confirmed more quantitatively in Figure 3.8, which shows the maximum particle concentration r_{sup} as a function of time for each of these five simulations. We see that the evolution of r_{sup} is more or less independent of the Reynolds number but increases with Péclet number. This trend will be

Figure 3.8: Comparison of r_{sup} for 2D simulations with varying Pe_p and Re for $T_p = 0.1$. Remaining parameters: $W_s = 0.1, R_\rho = 0.5, Re_p = 1000, Pr = 1$.

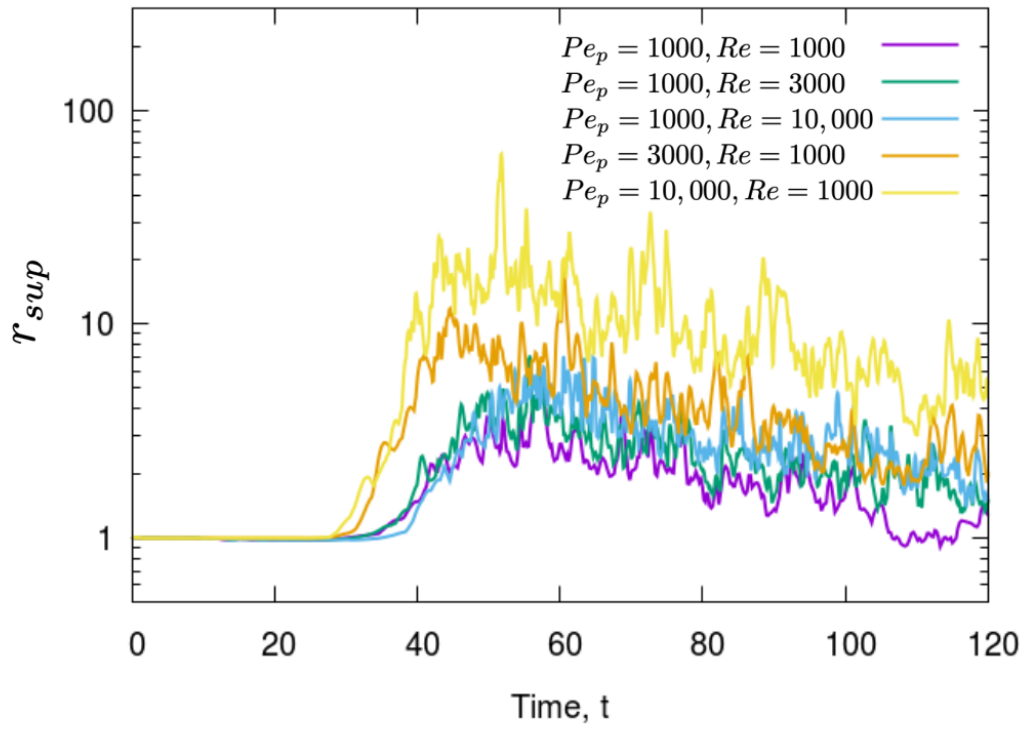

explained by the theory presented in Section 3.4.

In order to gain a more quantitative insight into the two-way coupling between the particles and the turbulence at all scales, we look at the power spectra of the particle concentration field and of the fluid velocity field. This time we restrict our analysis to an interval $[t_0, t_f]$ where $t_f - t_0 = 20$, during the peak of the mixing event when the particle concentration is largest. We define the time-averaged horizontal power spectrum for any state variable ξ as

$$\mathcal{P}_\xi(k_x) = \frac{1}{t_f - t_0} \int_{t_0}^{t_f} \sum_{k_z} \hat{\xi}(k_x, k_z, t) \hat{\xi}^*(k_x, k_z, t) dt, \tag{3.32}$$

where the $\hat{\xi}(k_x, k_z, t)$ is the discrete Fourier transform of ξ and $\hat{\xi}^*(k_x, k_z, t)$ is the

Figure 3.9: Power spectra of the particle concentration field (a) and the fluid velocity field (b) as a function of the horizontal wavenumber k_x for varying Re and Pe_p. Remaining parameters are $T_p = 0.1$, $W_s = 0.1, R_\rho = 0.5, Re_p = 1000$, and $Pr = 1$. The errorbars indicate the rms temporal variability of the spectrum.

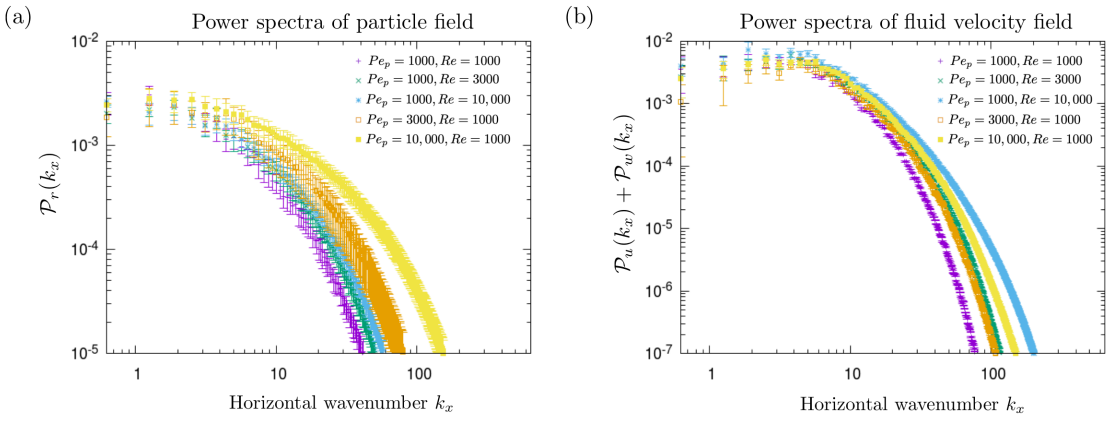

complex conjugate of $\hat{\xi}(k_x, k_z, t)$. Figure 3.9a shows the mean horizontal power spectrum of the particle concentration field $\mathcal{P}_r(k_x)$ with corresponding error bars representing one standard deviation around the mean. When Pe_p is fixed and Re increases, we observe a slight increase of power in the range $k_x = 10 - 100$, but the effect of Re is small. On the other hand, for fixed Re and large values of Pe_p, there is substantially more power in the higher wavenumbers, consistent with the predominance of smaller scales seen in the snapshots.

In Figure 3.9b, we plot the power spectrum of the total fluid velocity field $\mathcal{P}_u(k_x) + \mathcal{P}_w(k_x)$ as function of k_x with corresponding error bars. Unlike the particle concentration field, the spectrum here is affected by *both* Pe_p and Re. That is, the amount of energy at small scales increases when either Pe_p or Re increases. This can be explained by the fact that the strength of convection in our system is directly related to the Rayleigh number, which is proportional to the product of Pe_p and Re (3.21). It is therefore not surprising to find that the energy spectrum depends on the product Pe_pRe rather than Pe_p and Re individually.

Figure 3.10: Power spectra of the particle concentration field (left) and the fluid velocity field (right) as a function of the horizontal wavenumber k_x for varying T_p. Remaining parameters are $W_s = 0.1, R_\rho = 0.5, Re = 1000, Re_p = 1000, Pe_p = 1000$, and $Pr = 1$. The errorbars indicate the rms temporal variability of the spectrum (as in the previous figure).

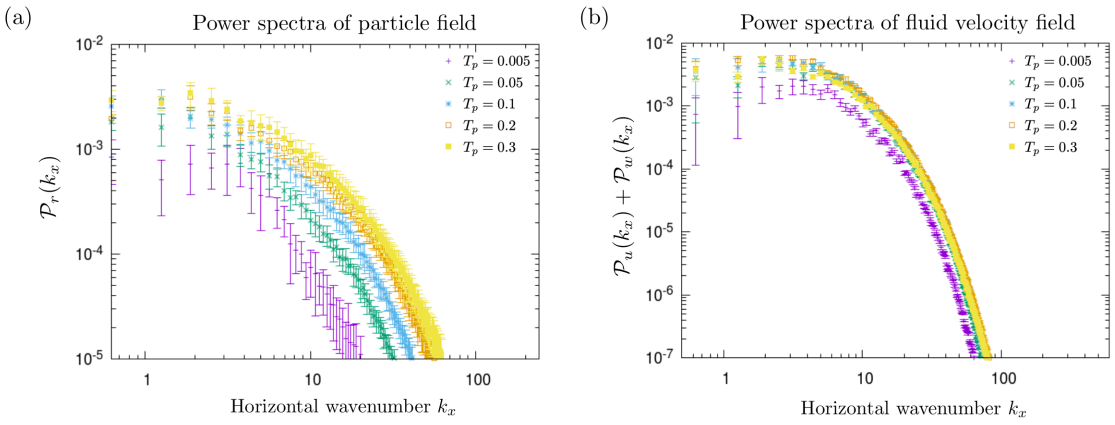

We also look at how the particle stopping time T_p affects the horizontal power spectra of the particle concentration and velocity fields. Figure 3.10 shows these power spectra (taken, as before, during the peak of the mixing event), for five simulations at varying T_p and otherwise fixed parameters (i.e. $W_s = 0.1, R_\rho = 0.5, Re = 1000$, $Pe_p = 1000$, Pr $= 1$; and $L_x = 10$, $L_z = 20$ with resolution for simulations found in Table 3.2). In Figure 3.10a, we see more power at large k_x as T_p increases. We see this as further evidence that the particles increasingly concentrate in narrower wisps as T_p increases. In Figure 3.10b, profiles of the total velocity power spectrum, i.e. $\mathcal{P}_u(k_x) + \mathcal{P}_w(k_x)$, are strikingly similar to one another. Thus, T_p does not appear to affect the turbulence in the system which is somewhat unexpected given the two-way coupling; instead, the velocity power spectrum is primarily dependent on Ra, at least for the range of parameters explored here.

3.3.4 Comparison between 2D and 3D simulations

Owing to the high resolution needed for the two-fluid simulations, especially for higher T_p, Re, and Pe_p, 3D simulations are typically prohibitive. However, we have run several 3D simulations at moderate $Re = 1000$, $Re_p = 1000$, and $Pe_p = 1000$ in order to compare the 3D results with the 2D ones. In this manner, we can determine whether 2D results can at least qualitatively capture the properties of the particle layer evolution. For all 3D simulations, we set the non-dimensional length, width, and height as $L_x = 10$, $L_y = 2$, and $L_z = 10$, respectively. In this section, we focus on two simulations with $T_p = 0.005$ and $T_p = 0.1$, respectively. The resolution of the low T_p case is $384 \times 72 \times 384$ grid points, while the high T_p case has a resolution of $768 \times 144 \times 768$ grid points. The remaining parameters are fixed to be $W_s = 0.1$ and $R_\rho = 0.5$.

Figure 3.11 shows that the values of u_{sup} achieved in the 2D simulation are consistently larger than the 3D simulation by 30-50% (for both low and high T_p cases). This result is consistent with those of (van der Poel et al., 2013) for Rayleigh-Bénard convection (where the rms velocities in 2D are systematically larger than in 3D by a factor of about 2). As a result, turbulent mixing and preferential concentration are both more energetic in 2D than in 3D at otherwise similar parameters. For low T_p where preferential concentration is not present, enhanced turbulent mixing results in r_{sup} being slightly smaller in 2D than in 3D. By contrast at high T_p, r_{sup} is slightly larger in 2D than in 3D due to the enhanced preferential concentration. Generally speaking, however, the dimensionality of the model does not appear to affect preferential concentration by more than a constant factor of a few (see more on this below), suggesting that 2D simulations are appropriate, at least as far as extracting scaling laws is concerned.

Figure 3.11: Comparison of the fluid velocity u_{sup} and particle concentration r_{sup} (defined in the text) between 2D and 3D simulations with settling velocity $W_s = 0.1, R_\rho = 0.5, Re = 1000, Re_p = 1000, Pe_p = 1000$, and $Pr = 1$. Left figure: $T_p = 0.005$. Right figure: $T_p = 0.1$.

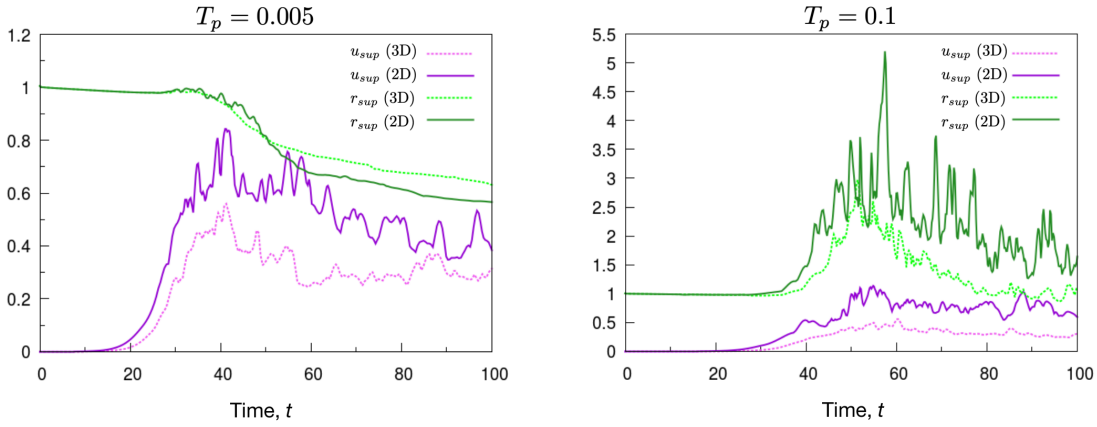

3.4 Predicting maximum particle concentration

We now present a simple model to quantify the effects of preferential concentration in convective particle-driven instabilities. We begin with the particle concentration equation (3.12), substituting $r = \overline{r}(z,t) + r'(\mathbf{x},t)$ (where $\mathbf{x}$ is the position vector):

$$\frac{\partial(\overline{r}+r')}{\partial t} + (\overline{r}+r')\nabla\cdot\mathbf{u}_p + \mathbf{u}_p\cdot\nabla(\overline{r}+r') = \frac{1}{Pe_p}\nabla^2(\overline{r}+r'). \tag{3.33}$$

By expanding the divergence term, we note that only the second term on the left-hand side contributes to preferential concentration (when $\nabla\cdot\mathbf{u}_p \neq 0$). We next assume that in the fully turbulent high T_p flow, the formation of regions of particularly strong particle concentration enhancement results from a dominant balance between the preferential concentration of the mean particle density and

diffusion terms of the perturbations so that

$$\overline{r}\nabla \cdot \mathbf{u}_p \sim \frac{1}{Pe_p}\nabla^2 r'. \tag{3.34}$$

We then express the particle velocity $\mathbf{u}_p$ in terms of T_p and $\mathbf{u}$, using a standard asymptotic expansion in T_p (Maxey, 1987):

$$\mathbf{u}_p = \mathbf{u} - W_s\hat{\mathbf{e}}_z - T_p\left(\mathbf{u}\cdot\nabla\mathbf{u} + \frac{\partial \mathbf{u}}{\partial t}\right) + O(T_p^2), \tag{3.35}$$

and thus,

$$\nabla \cdot \mathbf{u}_p = -T_p\nabla\cdot(\mathbf{u}\cdot\nabla\mathbf{u}) + O(T_p^2). \tag{3.36}$$

Substituting (3.36) in (3.34) results in

$$\overline{r}\nabla\cdot(\mathbf{u}\cdot\nabla\mathbf{u})T_p \sim \frac{1}{Pe_p}\nabla^2 r'. \tag{3.37}$$

Assuming that the length scales of the inertial concentration and diffusion terms are the same, we finally get

$$\frac{r'}{\overline{r}} \sim |\mathbf{u}|^2 T_p Pe_p \sim \frac{u_{rms}^2\tau_p}{\kappa_p}, \tag{3.38}$$

where the third part of this equation is expressed dimensionally. In this model, we therefore predict that strong particle concentration enhancements above the mean only depend on the magnitude of the fluid velocity $\mathbf{u}$, the particle stopping time T_p, and the assumed particle diffusion coefficient Pe_p. The prediction (3.38) made for $r'/\overline{r}$ should hold in a large-scale sense (i.e. a scale greater than several eddy scales), and can help quantify the expected spatiotemporal evolution of r' as long as that of $\overline{r}$ and $|\mathbf{u}|$ is known.

In order to test our model, we have run a large number of 2D simulations (with a few 3D ones) at different values of W_s, T_p, and Pe_p, listed in Table 3.2. Since the particle layer is not much wider than the size of an eddy, we investigate the validity of the model here only as a function of time, focusing on the behavior within the bulk of the particle layer (i.e. near $z = z_{max}$). To estimate the maximum particle concentration enhancement in the bulk of the particle layer, we let $r'(z,t) = r_{max}(z,t) - \overline{r}(z,t)$ and find the maximum value of $r'/\overline{r}$ at each instant in time to obtain

$$\left(\frac{r'}{\overline{r}}\right)_{max} \simeq \max_{z\in[z_{max}-1, z_{max}+1]} \frac{r_{max}(z,t) - \overline{r}(z,t)}{\overline{r}(z,t)}. \tag{3.39}$$

To estimate the corresponding typical fluid velocity, we define the rms total fluid velocity found within the particle layer, defined as

$$U_{rms}(t) = \left(\frac{1}{2L_xL_y}\int_{z_{max}-1}^{z_{max}+1}\int_0^{L_y}\int_0^{L_x}\left[u^2(\mathbf{x},t) + v^2(\mathbf{x},t) + w^2(\mathbf{x},t)\right]dx\,dy\,dz\right)^{1/2}, \tag{3.40}$$

where $L_y = 1$ and $v(\mathbf{x},t) = 0$ for 2D simulations.

In Figure 3.12, we plot $(r'/\bar{r})_{max}$ versus $U_{rms}^2 T_p Pe_p$ for one simulation ($T_p = 0.3, W_s = 0.1, R_\rho = 0.5, Re = 1000, Re_p = 1000, Pe_p = 1000$, and $Pr = 1$). Note that each data point represents an instant in time for which the full velocity and particle fields are available. Points start from the lower left corner and move up to the right as U_{rms} increases with time during the development of the convective instability. During the most turbulent stage of the simulation when particle concentration enhancement occurs, the points are clustered on the upper right-hand side of the plot. The dashed line represents the scaling relationship $(r'/\bar{r})_{max} \propto U_{rms}^2 T_p Pe_p$, shown here for ease of comparison with later figures.

Comparisons between $(r'/\overline{r})_{max}$ and $U_{rms}^2 T_p Pe_p$ are next shown in Figure 3.13

Figure 3.12: Maximum particle concentration enhancement over the mean as function of $U_{rms}^2 T_p Pe_p$ for a simulation with parameters $T_p = 0.3, W_s = 0.1, R_\rho = 0.5, Re = 1000, Re_p = 1000, Pe_p = 1000$, and $Pr = 1$. Each dot represents an instant in time, with points moving from the bottom-left corner to the top-right corner over time. The black solid line shows $(r'/\bar{r})_{max} = (1/4)U_{rms}^2 T_p Pe_p$.

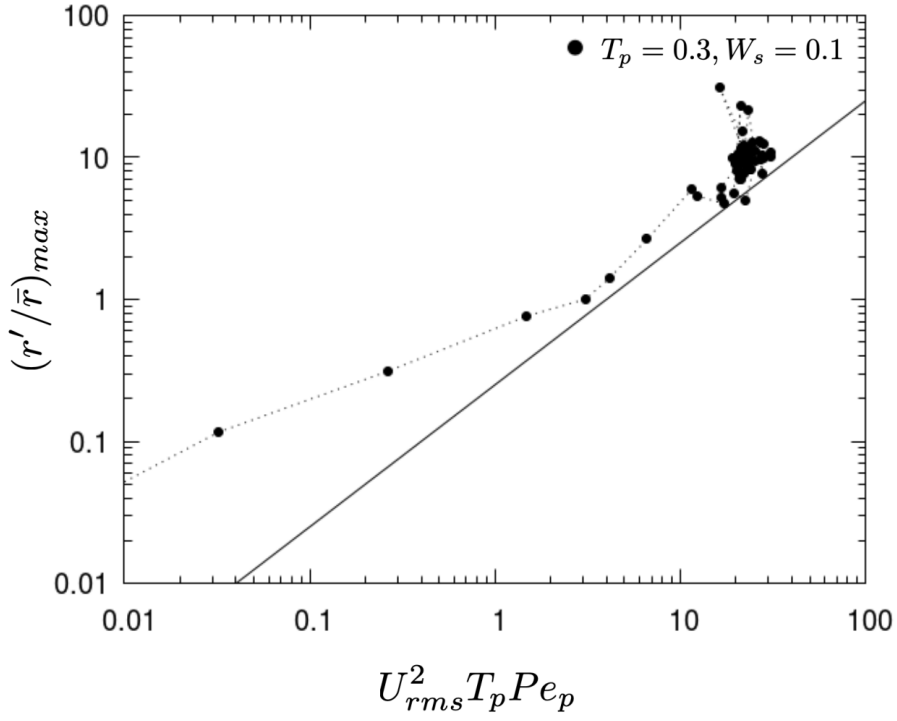

Table 3.2: Summary of salient parameters for the numerical simulations. In all cases, $R_\rho = 0.5$ and $Re_p = 1000$. The first four columns show W_s, T_p, Pe_p, and Re. The last column shows the effective number of mesh points used in each direction. All 2D simulations in this table were run with $L_x = 10$ and $L_z = 20$, and all 3D simulations were run with $L_x = 10$, $L_y = 2$, and $L_z = 10$.

(a) 2D Simulations

W_s	T_p	Pe_p	Re	$N_x \times N_z$
0.1	0.005	1000	1000	768×1536
0.1	0.005	10,000	1000	768×1536
0.1	0.005	100,000	1000	3072×6144
0.1	0.01	1000	1000	768×1536
0.1	0.05	1000	1000	768×1536
0.1	0.1	1000	1000	768×1536
0.1	0.1	3000	1000	1536×3072
0.1	0.1	10,000	1000	3072×6144
0.1	0.1	1000	3000	1536×3072
0.1	0.1	1000	10,000	3072×6144
0.1	0.2	1000	1000	1536×3072
0.1	0.3	1000	1000	1536×3072
0.3	0.005	1000	1000	768×1536
0.3	0.01	1000	1000	768×1536
0.3	0.05	1000	1000	768×1536
0.3	0.1	1000	1000	1152×2304
0.3	0.2	1000	1000	1536×3072
0.3	0.3	1000	1000	1536×3072

(b) 3D Simulations

W_s	T_p	Pe_p	Re	$N_x \times N_y \times N_z$
0.1	0.005	1000	1000	$384 \times 72 \times 384$
0.1	0.1	1000	1000	$768 \times 144 \times 768$
0.1	0.2	1000	1000	$768 \times 144 \times 768$

for all available simulations that have $R_\rho = 0.5, Re = 1000, Re_p = 1000, Pe_p = 1000$, and $Pr = 1$. Here, the color of the points represents T_p, the shape of the points represents W_s, and the size of the points corresponds to the dimensionality (2D vs. 3D), see legend for detail. For a given simulation, each point corresponds to a particular instant in time selected after the onset of the convective instability, but before the bulk of the particle layer has traveled more than one domain height (to avoid it interacting with itself). The solid line shows the relationship $(r'/\overline{r})_{max} = (1/4)U_{rms}^2 T_p Pe_p$, where the proportionality constant 1/4 was selected to fit (approximately) the 2D data in the higher T_p runs.

Focusing our attention first on the low T_p 2D simulations (shown in red and orange), we see that they do not fit the model, regardless of the values of W_s. This is as expected, since we have found that preferential concentration is negligible for $T_p \leq 0.01$ (e.g. Figure 3.8), and so the dominant balance assumed in deriving the model in equation (3.38) does not apply. Turning to the remaining 2D simulations, we see the data fits the predicted model well albeit with a significant scatter that is expected given the method we are using to extract r' and U_{rms}. We also see that even for cases with larger T_p, there appears to be a threshold (namely $U_{rms}^2 T_p Pe_p \approx 1$) below which the model is not valid. Above that threshold, the scaling law proposed correctly predicts how $(r'/\overline{r})_{max}$ evolves in a simulation as a function of time, or how the same quantity depends on input parameters. Finally, we have run several 3D simulations represented by the larger filled circles, and see that they also fit the model. We therefore conclude that equation (3.38) provides a reliable method for estimating the maximum possible particle concentration enhancement over the mean in a turbulent fluid (within the two-fluid formalism).

Figure 3.14 explores the dependence of the model on Re, Pe_p, and temperature stratification. As before, the low T_p simulations (in red) do not fit the model while

Figure 3.13: Maximum particle concentration enhancement over the mean as function of $U_{rms}^2 T_p Pe_p$, for varying W_s and T_p (with fixed $R_\rho = 0.5, Re = 1000, Re_p = 1000, Pe_p = 1000, Pr = 1$). The black solid line represents $(r'/\overline{r})_{max} = (1/4)U_{rms}^2 T_p Pe_p$. Details of simulations can be found in Table 3.2.

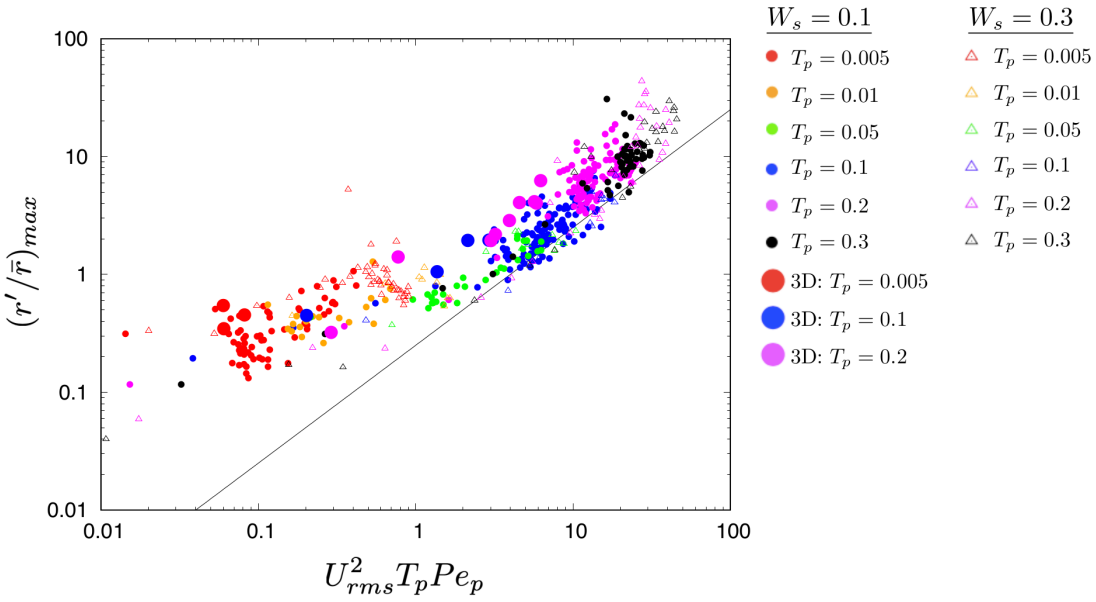

those at higher T_p (all other colors) do. We also see that, as discussed in Section 3.3.3, $(r'/\overline{r})_{max}$ is more or less independent of Re, but increases with Pe_p. Finally, simulations run in the same model setup but without a background temperature gradient (black stars) continue to satisfy the same scaling laws.

3.5 Typical particle concentration and pdfs of the relative particle concentration field

Having constructed a simple analytical model for the maximum particle concentration enhancement allowable in the system, we may wonder whether this model might also provide insight into the typical concentration enhancement. To do so, we define the typical concentration enhancement within the particle layer

Figure 3.14: Maximum particle concentration enhancement over the mean as function of $U_{rms}^2 T_p Pe_p$, for varying T_p, Re, and Pe_p (with $W_s = 0.1, R_\rho = 0.5, Pr = 1, Re_p = 1000$). The black solid line represents $(r'/\overline{r})_{max} = (1/4)U_{rms}^2 T_p Pe_p$. Details of simulations can be found in Table 3.2.

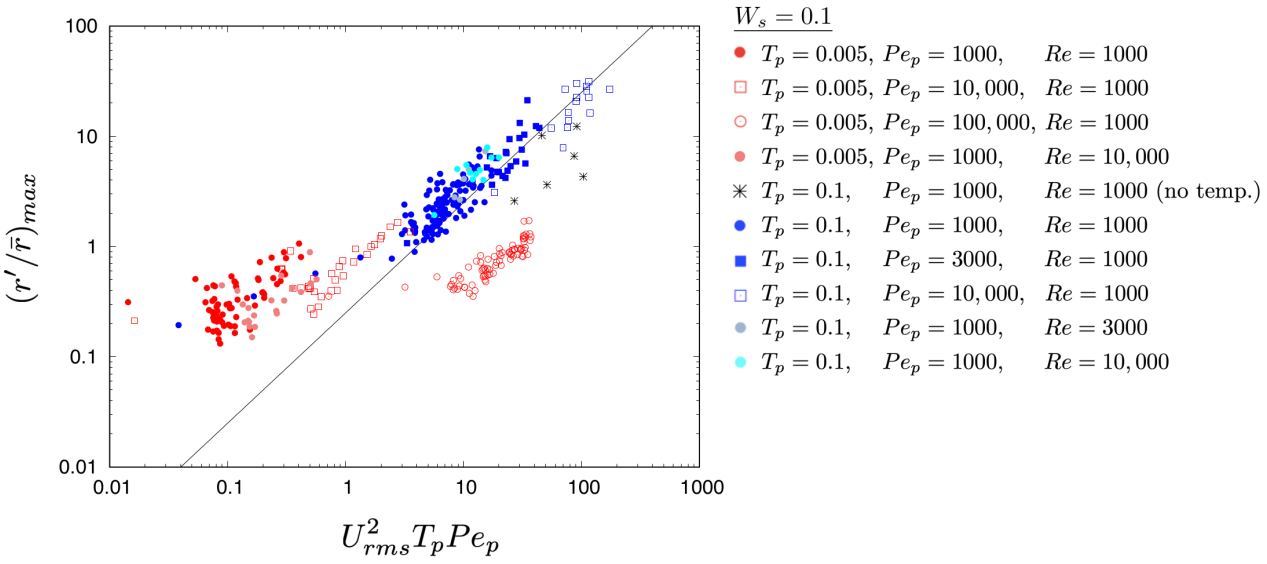

as:

$$\left(\frac{r'}{\overline{r}}\right)_{rms} = \frac{1}{2}\int_{z_{max}-1}^{z_{max}+1} \frac{r_{rms}(z,t)}{\overline{r}(z,t)} dz, \tag{3.41}$$

where r_{rms} was defined in (3.31). Results are shown in Figure 3.15, with the same black line as in Figure 3.13 also plotted to ease the comparison. Here, we see the data points do not fit this model, and seem to scale as $(r'/\overline{r})_{rms} \sim (U_{rms}^2 T_p Pe_p)^{1/2}$ instead (shown by the blue line). It is interesting to note that although we are capturing the *typical* enhancement, this model still depends on the same combination of parameters (i.e. the product of U_{rms}, T_p, and Pe_p) arising from the model discussed in Section 3.5. This strongly suggests that the typical particle concentration enhancement is related to the maximum particle concentration enhancement, though exactly how remains to be determined. We also see here that the low T_p simulations (in red and orange) do not follow the same scaling law as the high T_p cases.

More insight into the problem can be gained by looking at the probability distribution function (PDF) of the relative particle concentration:

$$r_{rel}(x,z,t) = \frac{r(x,z,t)}{\overline{r}(z,t)} = 1 + \frac{r'(x,z,t)}{\overline{r}(z,t)}. \tag{3.42}$$

We focus on values of r_{rel} within the bulk of the particle layer in the range $z \in [z_{max}(t) - 1,\, z_{max}(t) + 1]$. Figure 3.16 shows PDFs of r_{rel} for the low and high T_p cases presented in Section 3.3.4 at various times during the respective simulations. Prior to the onset of turbulence the PDF of r_{rel} is a δ-function centered at $r_{rel} = 1$ since $r = \overline{r}$. The distribution then widens once the instability develops, and the maximum value achievable by r_{rel} is equal to the value $(r'/\overline{r})_{max} + 1$ discussed in Section 3.5.

For the low T_p case, we see from Figure 3.16a that the PDF is more or less

Figure 3.15: Typical particle concentration enhancement for varying W_s and T_p with $R_\rho = 0.5, Pr = 1, Re = 1000, Re_p = 1000, Pe_p = 1000$, unless otherwise denoted. The black solid line represents $(r'/\bar{r})_{rms} = (1/4)U_{rms}^2 T_p Pe_p$, and the blue line represents $(r'/\bar{r})_{rms} = (1/5)(U_{rms}^2 T_p Pe_p)^{1/2}$. Details of simulations can be found in Table 3.2.

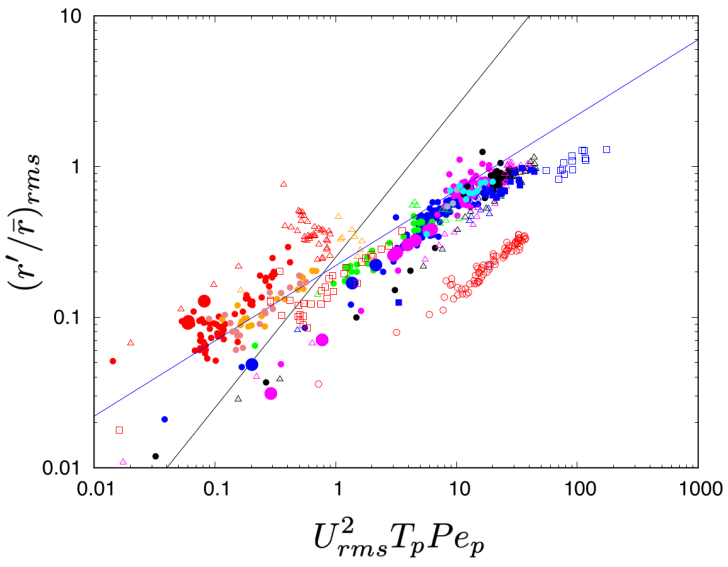

$W_s = 0.1$	T_p	Pe_p	Re
	0.005	1000	1000
	0.005	10,000	1000
	0.005	100,000	1000
	0.005	1000	10,000
3D:	0.005	1000	1000
	0.01	1000	1000
	0.05	1000	1000
	0.1	1000	1000
	0.1	3000	1000
	0.1	10,000	1000
	0.1	1000	3000
	0.1	1000	10,000
3D:	0.1	1000	1000
	0.2	1000	1000
3D:	0.2	1000	1000
	0.3	1000	1000

$W_s = 0.3$	T_p	Pe_p	Re
	0.005	1000	1000
	0.01	1000	1000
	0.05	1000	1000
	0.1	1000	1000
	0.2	1000	1000
	0.3	1000	1000

Figure 3.16: Probability distribution functions for the function r_{rel} (3.42) at various times during two simulations with $W_s = 0.1, R_\rho = 0.5, Pr = 1, Re = 1000, Re_p = 1000$, and $Pe_p = 1000$ for $T_p = 0.005$ (a) and $T_p = 0.1$ (b).

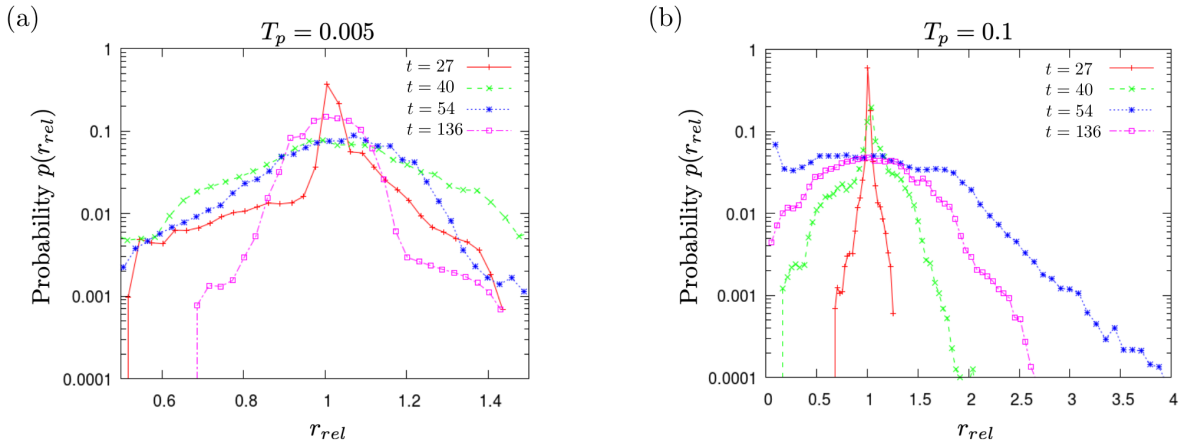

symmetric about $r_{rel} = 1$ at all times, and remains relatively narrow around this mean value (at least, compared with the high T_p case described below). As the simulation proceeds, the width of the PDF first increases and then decreases with time, as a result of the concurrent increase and decrease of the turbulent fluid velocity u^*_{rms} (3.29) in the bulk of the layer during the convective mixing event. In contrast, for the high T_p simulation shown by Figure 3.16b, the PDF widens considerably during the convective mixing event and becomes asymmetric. A long tail of rare events associated with preferential concentration appears. The shape of the tail appears to be exponential, consistent with what is commonly found in Eulerian-Lagrangian simulations of preferential concentration (e.g. Shotorban & Balachandar, 2006; Zaichik & Alipchenkov, 2005).

To explore the properties of this exponential tail, we present PDFs of r_{rel} taken during the peak of the mixing event for different simulations at fixed $Re = 1000$ and $Pe_p = 1000$ for varying T_p in Figure 3.17a. We observe that as T_p increases, the slope of the exponential tail becomes shallower as the maximum value of r_{rel}

Figure 3.17: Time-averaged PDFs of r_{rel} (see Equation 3.42) during the peak of the mixing event. (a) At fixed $W_s = 0.1, R_\rho = 0.5, Re = 1000, Re_p = 1000, Pe_p = 1000$, and $Pr = 1$ and varying T_p. (b) At fixed $T_p = 0.1, W_s = 0.1, R_\rho = 0.5, Re_p = 1000$, and $Pr = 1$ and varying Re and Pe_p.

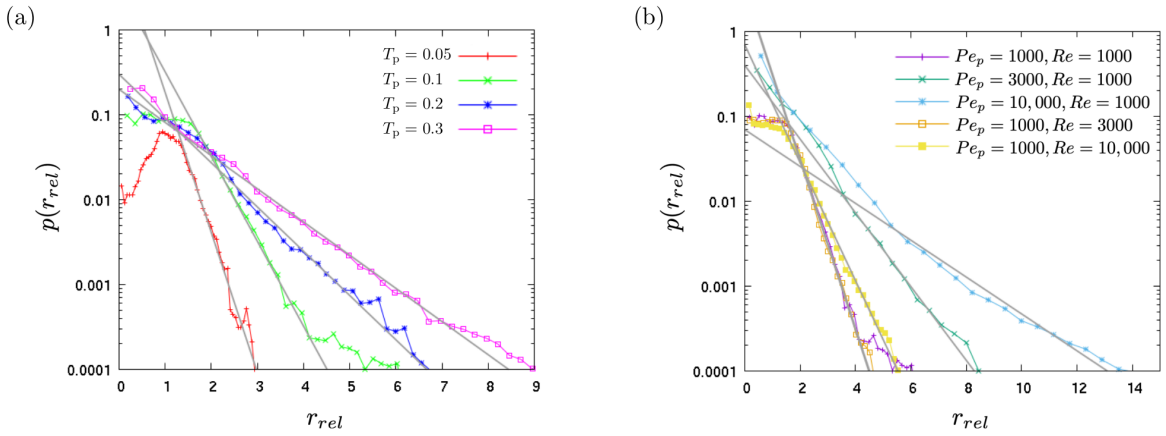

achieved in the simulation increases. In Figure 3.17b, we present PDFs of r_{rel} for varying Re and Pe_p at fixed $T_p = 0.1$, taken again at the maximum of the mixing event. We see that the tail widens with increasing Pe_p but not with Re, which is consistent with our finding that Re does not directly influence the maximum particle concentration achievable (at these parameter values and in this model), but Pe_p on the other hand does.

We have fitted an exponential function $f(x) \propto e^{-bx}$ to the tail of the PDF for each of the cases described above. Figure 3.18 shows b as a function of $U_{rms}^2 T_p Pe_p$ (where U_{rms} and b are computed at the same times). We find that the data points follow the red solid line $b \sim (U_{rms}^2 T_p Pe_p)^{-1/2}$, which is the same scaling as $(r'/\overline{r})_{rms}^{-1}$. This is perhaps not a coincidence, since the rms of $r_{rel} = 1 + r'/\overline{r}$ would be equal to $1/b$ if the distribution was exactly exponential with slope b.

Figure 3.18: The slope b of the exponential tail of the PDF of r_{rel} as a function of $U_{rms}^2 T_p Pe_p$ for simulations at various T_p, Re, and Pe_p with $W_s = 0.1, R_\rho = 0.5, Re_p = 1000$, and $Pr = 1$. In all cases, the the PDF is computed during the peak of the mixing event. The red solid line shows $b = 7(U_{rms}^2 T_p Pe_p)^{-1/2}$.

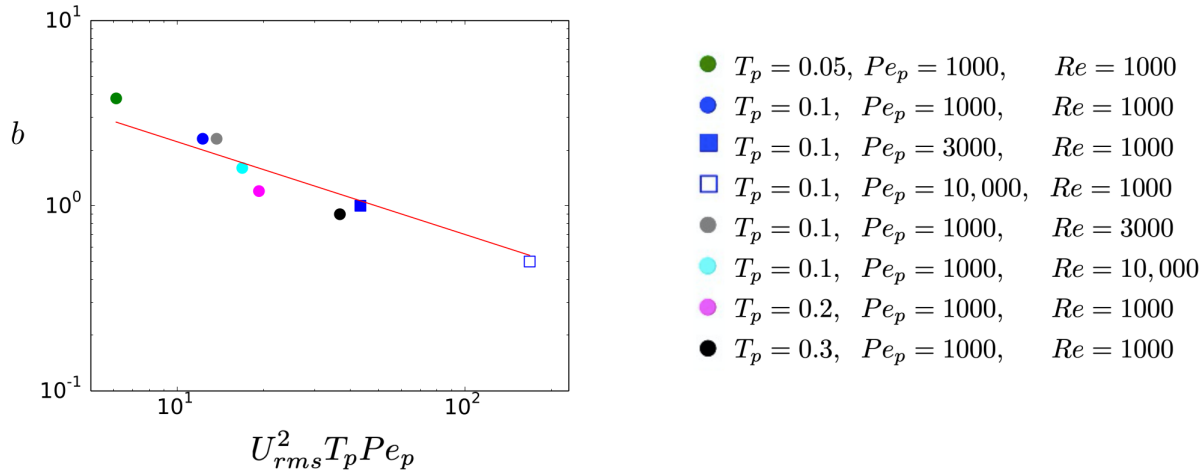

3.6 Summary, applications, and discussion

3.6.1 Summary

In this work, we studied preferential concentration in a two-way coupled particle-laden flow subject to the particle-driven convective instability, using DNSs of the two-fluid equations. We constructed an estimate of the typical turbulent eddy velocity in the mixing event as $u_{rms} = \sqrt{r_0 g \sigma}$ (written here dimensionally), where r_0 is the ratio of the typical particle mass density excess in the layer to the fluid density, g is gravity, and σ is the unstable layer height. Using this, we then constructed an estimate of the particle Stokes number as $T_p = \tau_p (r_0 g/\sigma)^{1/2}$, where τ_p is the dimensional particle stopping time. We found that for $T_p \leq 0.01$, the system properties are indistinguishable from those obtained using the equilibrium Eulerian formalism, while for $T_p \geq 0.01$, preferential concentration can cause an increase in the particle density in regions of low vorticity or high strain rate, as

predicted by (Maxey, 1987). The maximum particle concentration enhancement over the local mean, $\max(\rho_p'/\bar{\rho}_p)$, can be predicted from simple arguments of dominant balance to scale as $\max(\rho_p'/\bar{\rho}_p) \sim u_{rms}^2 \tau_p/\kappa_p$, where κ_p is the dimensional particle diffusivity used in the two-fluid model. We verified that this scaling holds for a range of simulations with varying input parameters, as long as $T_p > 0.01$, and $u_{rms}^2 \tau_p/\kappa_p > 1$. In this regime, we also found that the probability distribution function of the quantity $\rho_p'/\bar{\rho}_p$ has a root mean square value that scales as $(u_{rms}^2 \tau_p/\kappa_p)^{1/2}$ and an exponential tail whose slope scales as $(u_{rms}^2 \tau_p/\kappa_p)^{-1/2}$.

3.6.2 Applications

We can use the model proposed in Section 3.4 to predict the maximum particle concentration enhancement over the mean for several applications, where the main source of turbulence is the particle-driven convective instability. It is important to note that our model can only be applied to inertial particles that follow the conditions used for the two-fluid formalism, namely that (1) particles follow Stokes' law; and (2) the Stokes number is less than about 0.3.

We first look at ash created by volcanic eruptions, droplets in stratus clouds, and sediments suspended in turbidity currents. In all these cases, the particle stopping time is given by

$$\tau_p = \frac{m_p}{6\pi s_p \rho_f \nu}, \tag{3.43}$$

where s_p is the particle radius, and so, the terminal settling velocity is given by

$$w_s = \tau_p \left(\frac{\rho_s - \rho_f}{\rho_s} \right) g = \frac{2}{9} \left(\frac{\rho_s - \rho_f}{\rho_f} \right) \frac{g}{\nu} s_p^2. \tag{3.44}$$

Ash particles are generated by volcanic eruptions and have widespread environmental and health implications. Ash particles are transported upwards in the

volcanic plume, and eventually spread laterally to form an umbrella cloud in the stratosphere (Sparks & Wilson, 1976; Woods, 1995). In recent years, there has been renewed interest in predicting the rate of sedimentation of the ash, which is known to depend on preferential concentration (Cerminara et al., 2016; Carazzo & Jellinek, 2013; Webster et al., 2012). Suspended ash particles vary widely in radius, especially between the volcanic plume (where s_p ranges from 0.1 mm to 1 mm (Harris & Rose Jr, 1983)) and the umbrella cloud (where s_p ranges from 0.1 to 10 μm, since the larger particles have settled out (Carazzo & Jellinek, 2013; Webster et al., 2012)). Similarly, the typical particle concentration ρ_p ranges from 0.1 μg/m^3 to 1 mg/m^3 (see Carazzo & Jellinek, 2013 and references therein) within the umbrella cloud with larger concentration values closer to the eruption site (observed to be 50 mg/m^3 from Harris & Rose Jr, 1983, for instance). We therefore estimate the Stokes number from (3.43) as T_p given by

$$T_p \approx (2 \times 10^{-7}) \left(\frac{\rho_p}{1 \text{ mg/m}^3} \right)^{1/2} \left(\frac{\sigma}{1 \text{ km}} \right)^{-1/2} \left(\frac{s_p}{10 \ \mu\text{m}} \right)^2 . \tag{3.45}$$

To arrive at this formula, we have used commonly accepted values for certain parameters, i.e. $(\rho_s - \rho_f)/\rho_f \approx 1000$, $\nu \approx 10^{-5}$ m^2/s, and $g \approx 10$ m/s^2. We see that for values characteristic of the umbrella cloud, namely ρ_p of order 1 mg/m^3, σ of order 1 km and s_p of order 10 μm, $T_p \sim O(10^{-7}) \ll O(0.1)$. Such a small value of T_p does not fall in the inertial regime of our model, and thus the effects of preferential concentration due to particle-driven convective instability are negligible. Closer to the volcanic plume, $s_p \sim 0.25$ mm and $\rho_p \sim 50$ mg/m^3. Keeping the remaining parameters as before, we find that $T_p \approx 0.01$, which lies at the boundary of the inertial regime, suggesting that preferential concentration is possible in this case. To determine the maximum particle concentration enhancement, we then

use

$$\left(\frac{\rho_p'}{\bar{\rho}_p}\right)_{max} = \frac{1}{4}\frac{|\mathbf{u}|^2\tau_p}{\kappa_p} = 25\left(\frac{\rho_p}{1\ \mathrm{mg/m^3}}\right)\left(\frac{\sigma}{1\ \mathrm{km}}\right)\left(\frac{s_p}{10\ \mu\mathrm{m}}\right)^{-1} \tag{3.46}$$

where $|\mathbf{u}|$ is calculated from (3.8) and $\kappa_p \sim w_s s_p$ (see Ham & Homsy, 1988; Nicolai et al., 1995; Segre et al., 2001). Thus, from equation (3.46) for conditions closer to the volcano with ∼0.25 mm ash particle and $\rho_p \sim 50$ mg/m^3, we obtain $(\rho_p'/\bar{\rho}_p)_{max} \approx O(100)$, and so, the inertial concentration mechanism may be important in this case.

We also considered other geophysical applications in which particle-driven convection could be relevant, such as stratus clouds and turbidity currents. Using commonly accepted values for these systems, we found that the estimated Stokes number T_p is always very small, and therefore does not fall under the inertial regime where preferential concentration takes place (see Appendix 3.7 for details).

A more interesting application of our model can be found in the astrophysical context of a collapsing protostar, i.e. a contracting cloud composed of a mixture of gas and dust particles that will eventually lead to the formation of a star. The contraction is usually slow and quasi-hydrostatic, and the gas is generally stably stratified. However, we expect that waves or shocks propagating through it would create inhomogeneities in the dust concentration, that are conceivably gravitationally unstable to particle-driven convective instabilities. With this in mind, we consider typical interstellar dust particles to have a radius of size $s_p \sim 10$ μm and solid density $\rho_s \sim O(10^3)$ kg/m^3. The gas density within a cloud of radius R astronomical units (AU, where 1 AU $= 10^{11}$ m) is typically of order $\rho_f \sim O(10^{-12})$ kg/m^3. The dust-to-gas mass ratio in these clouds is of order $r_0 \sim 0.01$, and we anticipate large-scale perturbations above this mean value driven by waves or shocks to be of the same order of magnitude.

Given that the size of the dust particles in this case is much smaller than the

mean free path of the gas, the stopping time is now given by

$$\tau_p = \frac{s_p \rho_s}{c \rho_f}, \tag{3.47}$$

where c is the sound speed (i.e. $c \approx k_B T/m_H$, where $k_B = 1.38 \times 10^{-23}$ m^2 kg s^{-2} K^{-1} is the Boltzmann constant, $m_H \approx 10^{-27}$ kg is the mass of a hydrogen molecule, and T is the local temperature, which is of the order 10 K in clouds (Tobin et al., 2012)). Using $g = GM_\star/R^2$ in (3.47), where $G = 6.7 \times 10^{-11}$ m^3 kg^{-1} s^{-2} is the gravitational constant and $M_\star$ is the mass of the core of the protostar, we then find that the non-dimensional stopping time is given by

$$T_p = (10^{-1})\left(\frac{s_p}{10\ \mu\text{m}}\right)\left(\frac{\rho_s}{10^3\ \text{kg/m}^3}\right)\left(\frac{\rho_f}{10^{-12}\ \text{kg/m}^3}\right)^{-1} \left(\frac{T}{10\ \text{K}}\right)^{-1/2}\left(\frac{r_0}{0.01}\right)^{1/2}\left(\frac{M_\star}{M_\odot}\right)^{1/2}\left(\frac{R}{100\ \text{AU}}\right)^{-1}\left(\frac{\sigma}{0.01\ \text{AU}}\right)^{-1/2},$$

where $M_\odot = 2 \times 10^{30}$ kg is the mass of the Sun. Here, we see that by using typical values for a protostar and assuming that the particle density inhomogeneities are initially of size 0.01 AU, then T_p lies within the inertial regime. The relative maximum particle concentration can be then written as

$$\left(\frac{r'}{\bar{r}}\right)_{max} = (10^{11})\left(\frac{s_p}{10\ \mu\text{m}}\right)^3\left(\frac{\rho_s}{10^3\ \text{kg/m}^3}\right)\left(\frac{r_0}{0.01}\right) \left(\frac{T}{10\ \text{K}}\right)^{-1}\left(\frac{M_*}{M_\odot}\right)\left(\frac{R}{100\ \text{AU}}\right)^{-2}\left(\frac{\sigma}{0.01\ \text{AU}}\right).$$

While this relative enhancement is huge, it is not sufficient to bring particles in contact with one another. Indeed, the associated volume fraction of particles would be $\Phi' = r_0(\rho_f/\rho_s)(r'/\bar{r})_{max} \approx 10^{-6}$. Nevertheless, this does imply that the particle collision rate within these enhanced regions would dramatically in-

crease, suggesting that preferential concentration due to particle-driven convective instabilities could play a role in star and planet formation.

3.6.3 Discussion

Assuming that the model described in Section 3.4 and summarized in 3.6.1 is generally valid in particle-laden turbulent flows, it provides a very simple way of estimating the expected enhancement in the local particle density due to preferential concentration, which could be very useful for predicting its impact on other processes, such as particle growth or enhanced settling, as demonstrated in 3.6.2. However, several caveats of the model need to be kept in mind before doing so. First and foremost is the fact that the maximum particle concentration enhancement over the local mean depends explicitly on the particle diffusivity κ_p, which is derived from a simplistic model of the interaction between the particles and the fluid, as well as among the particles themselves. In the limit where Brownian motion is the dominant contribution to the particle diffusivity, then the model is likely to be valid. This is the case for instance in astrophysical applications. However, when the interaction of the particle with its own wake or with the wakes of other particles dominates, then the simple diffusion model $\kappa_p \nabla^2 \rho_p$ presumably fails to capture some of their more subtle consequences and should only be used with considerable caution. Comparisons of the model with particle-resolving simulations will help elucidate whether any of our results still holds for more realistic situations.

Another caveat of the model is the fact that it has only been validated so far in moderately turbulent flows, for which the inertial range is fairly limited. In more turbulent systems, where the inertial range spans many orders of magnitude in scales, the Stokes number at the injection scale could be quite different from

the Stokes number at the Kolmogorov scale. Assuming a Kolmogorov power spectrum for the kinetic energy, for instance, it is easy to show that the Stokes number increases weakly with wavenumber, and can be substantially larger at the Kolmogorov scale than at the injection scale when the Reynolds number is very large. This raises the question of whether the model remains applicable when this is the case. Finally, we note that the model has so far only been tested in the context of particle-driven convection, where the two-way coupling between the particles and the fluid likely influence the turbulent cascade. It remains to be determined whether the same scalings are found in flows where the source of the turbulence is independent of the particles (such as mechanically driven turbulence, or thermal convection, for instance). If this is the case, our findings may have further implications for engineering or geophysical flows. Both of these questions will be the subject of future work.

There are also several other questions that remain to be answered. The simulations presented in Section 3.3.3, for instance, clearly show that the particle Péclet number influences the typical width and separation of the regions of high particle density, but this effect remains to be explained and modeled. This will require a better understanding of the influence of the two-way coupling between the particles and the fluid on the turbulent energy cascade from the injection scale to the dissipation scale. In particular, it is clear from a cursory inspection of the kinetic energy spectrum (see Figure 3.9) that the extent of the inertial range depends on the Reynolds number and, as expected, but also on the particle Péclet number, suggesting that this two-way coupling dominates the flow dynamics at small scales. Although this is perhaps not surprising, it deserves to be investigated further. Moreover, it would be interesting to see whether the same effect occurs in a system in which the turbulence is not driven by the particles themselves.

S.N. acknowledges funding by NSF AST-1517927 grant. S.N. was also partially supported by the NSF-MSGI summer program at Lawrence Berkeley Laboratory under the supervision of A. Myers and A. Almgren. Simulations were run on a modified version of the PADDI code, originally written by S. Stellmach, on the UCSC Hyades cluster and the NERSC Cori supercomputer. The authors thank Eckart Meiburg and Doug Lin for helpful discussions and the referees for their suggestions on how to improve the paper.

3.7 Appendix

Properties of PADDI

The governing equations are solved in spectral space using a third-order semi-implicit Adams-Bashforth backward-differencing scheme. Diffusive terms are treated implicitly. Nonlinear terms and drag terms are first computed in real space, then transformed into spectral space using FFTW libraries, and advanced explicitly. Drag terms are tracked and computed in a way that ensures the total momentum is conserved (other than the dissipation terms) throughout the simulations.

We encountered various numerical obstacles during the implementation of the two-fluid equations in PADDI-2F that are worth mentioning here. Due to the fact that particle inertia tends to increase particle concentration in certain regions for large enough T_p, one must use a very high spatial resolution to avoid numerical instability. Even when the resolution is large enough to ensure numerical stability, a slight under-resolution can result in the particle concentration being slightly over- or underestimated, resulting in the total mass not being exactly conserved. Indeed, in a spectral code, low resolution can induce the Gibbs phenomenon which can create regions of unphysical negative particle density near the edges of a

particle front. In the code, we zero out the negative particle density regions and rescale the particle concentration r at every point in space to ensure that the total particle mass is equal to its initial value at each time step. Note that this "fix" is generally not necessary as long as the simulations are well-resolved, but is introduced to reduce errors in the rare occasions where the system does become slightly under-resolved.

Other geophysical applications

We looked at the applicability of our model for the preferential concentration of water droplets found in stratus clouds. These clouds are a more relevant application of our model than convective clouds (i.e. cumulus and cumulonimbus) in which turbulence is primarily driven by thermal convection rather than particle-driven convection. We estimate r_0 and T_p as

$$r_0 = (2.5 \times 10^{-4})\left(\frac{\rho_p}{0.25 \text{ g/m}^3}\right), \tag{3.48}$$

$$T_p \approx (3.5 \times 10^{-6})\left(\frac{\rho_p}{0.25 \text{ g/m}^3}\right)^{1/2}\left(\frac{1 \text{ km}}{\sigma}\right)^{1/2}\left(\frac{s_p}{10\ \mu\text{m}}\right)^2, \tag{3.49}$$

where ρ_p here is otherwise known as the liquid water content which is typically of the order of 0.25 g/m^3 for stratus clouds (Frisch et al., 2000). We have also applied commonly accepted values for certain parameters for these formulas (i.e. $\rho_s/\rho_f \approx 1000$, $\nu \approx 10^{-5}$ m^2/s, $g \approx 10$ m/s^2). According to (3.49), we see that for any reasonable droplet size, T_p is in the regime where preferential concentration would not occur due to the particle-driven convective instability.

We now look at particle concentration in the context of turbidity currents which play a vital role in the global sediment cycle. We consider sediments consisting of clay, silt, or sand that vary in radius from $O(10^{-4}) - O(10^{-1})$ cm (where

clay is found at the lower end of this range, while sand particles are found at the larger end) with solid density typically around $\rho_s \approx 2000$ kg/m^3. For a particle volume fraction Φ in the dilute regime, $\Phi \lesssim 0.01$ and so, $r_0 \lessapprox 0.02$, and

$$T_p \approx (2 \times 10^{-4}) \left(\frac{10 \text{ m}}{\sigma} \right)^{1/2} \left(\frac{s_p}{0.1 \text{ mm}} \right)^2 \left(\frac{\Phi}{0.01} \right)^{1/2}, \tag{3.50}$$

in which we have assumed that $(\rho_s - \rho_f)/\rho_f \sim O(1)$. We therefore see that even for the largest particle size and for the maximum volume fraction allowable, for any reasonable value of σ, $T_p \ll 0.1$ so preferential concentration due to particle-driven convective instabilities is again negligible.

Chapter 4

Preferential concentration by mechanically-driven turbulence in the two-fluid formalism

This chapter is composed of a working revision after comments by the referees of Nasab & Garaud (2021), which has been submitted to Physical Review Fluids.

4.1 Introduction

Particle-laden flows are a special class of two-phase fluid flows, characterized by a continuous carrier phase and a dispersed, and typically dilute, particle phase. They appear in numerous physical and engineering applications, including for instance clouds, turbidity currents, protoplanetary disks, and industrial sprays. An important physical process in such flows is the tendency of inertial particles to accumulate in regions of high strain and low vorticity (Maxey, 1987), otherwise known as preferential concentration. This process is thought to play a fundamental role in promoting collisional growth. In clouds for example, the growth of micron-

size to millimeter size droplets is not quite understood. Although processes such as Brownian motion and condensation can contribute to droplet growth, it is thought that they alone cannot promote sufficient growth to initiate rainfall. For this reason, preferential concentration is considered to be the key process that may result in the enhanced collision rates required for larger raindrop formation (Wang et al., 2008; Devenish et al., 2012; Grabowski & Wang, 2013). Similarly in accretion disks, preferential concentration is widely hypothesized to be a vital process for the growth of dust particles into planetesimals (Birnstiel et al., 2016; Weidenschilling & Cuzzi, 1993). Thus, our primary goal is to investigate and quantify particle concentration enhancement due to preferential concentration in turbulent flows.

In this work (as also in Nasab & Garaud, 2020), we use the two-fluid formalism and treat the particles as a continuous phase of the system that is distinct from the carrier fluid (see Crowe et al., 1996; Elghobashi, 1994; Morel, 2015 and references within). This continuum approximation is derived by applying techniques motivated by kinetic theory in which the positions and velocities of the particles are statistically averaged to create a local particle density ρ_p and velocity $\mathbf{u}_p$. We focus on the case where the solid density of the particle ρ_s is much greater than the mean density of the carrier flow ρ_f, which is true for many applications. In this limit, the importance of particle inertia is traditionally measured by the Stokes number $St = \tau_p/\tau_e$, defined as the ratio of the particle stopping time τ_p to the eddy turnover time τ_e. It has been established that the two-fluid formalism is valid provided that $St \leq 0.3$ (Ferry & Balachandar, 2002). For larger St, the particles become increasingly uncorrelated with the fluid, and in turn, with one another. When this occurs, the continuum treatment is no longer appropriate.

Using the two-fluid formalism, we recently explored preferential concentration

in the context of the particle-induced convective instability (Nasab & Garaud, 2020). Our model setup consisted of a carrier fluid with an assumed stable temperature gradient, to which a layer of small and dense inertial particles was added to create linearly unstable initial conditions. We restricted our study to particles with $St \leq 0.3$ in order to stay within the limit of validity of the two-fluid model. In addition, due to the high computational cost required to resolve fine particle structures, we primarily ran 2D Direct Numerical Simulations (DNS). In all cases, we ran the simulations long enough to study the development of the Rayleigh-Taylor instability, and measured the maximum and typical particle concentration enhancement above the horizontally-averaged particle density.

Most notably, we found that the maximum particle concentration enhancement above the mean is related to the particle stopping time τ_p, the rms fluid velocity in the turbulent layer u_{rms}, and the assumed particle diffusivity κ_p, scaling as $u_{rms}^2\tau_p/\kappa_p$. Additionally, we showed that the typical particle concentration enhancement over the mean scales as $(u_{\mathrm{rms}}^2\tau_p/\kappa_p)^{1/2}$. We also computed the probability distribution function (pdf) of the particle concentration enhancement above the mean and found that in the presence of inertial particles, the tail of the pdf appears to be an exponential whose slope scales as $(u_{\mathrm{rms}}^2\tau_p/\kappa_p)^{-1/2}$. We then explained the importance of the parameter group $u_{\mathrm{rms}}^2\tau_p/\kappa_p$ using arguments of dominant balance between the inertial concentration and diffusion terms in the particle transport equation (more details can be found in Section 4.4). Although we showed that the model was quite useful in predicting the maximum particle concentration in turbulent flows, our study was limited to flows where the turbulence was driven by the particles themselves. Therefore, whether these results are more generally applicable to any turbulent particle-laden flow remained to be established. This crucial question is answered in the present paper.

The paper is organized as follows. In Section 4.2 we introduce the model setup and the governing equations based on the two-fluid formalism. In Section 4.3 we present DNS for varying governing parameters (such as the Stokes number and the fluid Reynolds number, for instance), and explore how they affect both preferential concentration and the energetics of the system. In Section 4.4 we briefly review the predictive model for maximum particle concentration enhancement presented in Nasab & Garaud (2020) and compare it to the new DNSs. We further look at the typical particle concentration enhancement and the associated pdf of the particle concentration. Section 4.5 briefly summarizes and presents applications of our model. We discuss the implications of these results and conclude with final remarks.

4.2 The Model

In this work we use the two-fluid model described in Nasab & Garaud (2020) to study the dynamics of a dilute monodisperse suspension of particles in a turbulent carrier fluid once it reaches a statistically stationary state. For simplicity, we assume that the inertial particles have a solid density that is much larger than the mean fluid density such that $\rho_s \gg \rho_f$. We also assume that they are sufficiently small so that Stokes' law can be applied, in which case $\tau_p = \rho_s d_p^2/18\rho_f\nu$, where d_p is the diameter of the particle, ρ_f and ν are the mean density and the kinematic viscosity of the fluid, respectively. Since the particles are much denser than the fluid, effects incorporated in terms such as the Basset history, Faxen correction, and added mass can be neglected (Maxey & Riley, 1983). We additionally require that the particle stopping time τ_p should be much smaller than the typical eddy turnover time of the carrier fluid τ_e, so $St \ll 1$.

We use the Boussinesq approximation (Boussinesq, 1903a) for the carrier fluid

and obtain the following governing equations after a suitable approximation of the particle equations (see Nasab & Garaud, 2020):

$$\frac{\partial \mathbf{u}}{\partial t} + \mathbf{u} \cdot \nabla \mathbf{u} = -\frac{\nabla p}{\rho_f} + r\frac{\mathbf{u}_p - \mathbf{u}}{\tau_p} + \nu \nabla^2 \mathbf{u} + \frac{1}{\rho_f}\mathbf{F}, \tag{4.1}$$

$$\frac{\partial \mathbf{u}_p}{\partial t} + \mathbf{u}_p \cdot \nabla \mathbf{u}_p = \frac{\mathbf{u} - \mathbf{u}_p}{\tau_p} + \nu_p \nabla^2 \mathbf{u}_p, \tag{4.2}$$

$$\frac{\partial r}{\partial t} + \nabla \cdot (\mathbf{u}_p r) = \kappa_p \nabla^2 r, \tag{4.3}$$

$$\nabla \cdot \mathbf{u} = 0, \tag{4.4}$$

where the fluid velocity is $\mathbf{u} = (u, v, w)$, p is the pressure, and the particle velocity is $\mathbf{u}_p = (u_p, v_p, w_p)$. Within this formalism, we define the local number density of particles to be n_p, and the corresponding mass density to be $\rho_p = n_p m_p$, where m_p is the mass of a single particle. For convenience, we refer to $r = \rho_p/\rho_f$ as the rescaled particle density with respect to the mean density of the carrier fluid (see Nasab & Garaud, 2020 for details).

By treating the particles as a continuum, we need to account for the stochastic aspect of particle trajectories, such as Brownian motion and the interaction of a particle with its own or another particle's wake. Generally these interactions are complex in nature, and thus, difficult to implement realistically and numerically. Here we assume that they take the form of a diffusion operator in the equations for the particle density and velocity and set the corresponding diffusivities ν_p and κ_p to be constant. This approximation is actually valid in the limit where Brownian motion is dominant, but is used for simplicity otherwise.

We initialize the particles with a uniform distribution in r such that $r = r_0$ everywhere in the domain. In this study, we choose to explore the range $0.1 \leq r_0 \leq 10$. Note that $r_0 = \Phi_0 \rho_s/\rho_f$, where the initial volume fraction of the particles Φ_0 is small so that the system is well within the dilute limit. Smaller values of

r_0 correspond to systems such that $\rho_s/\rho_f \lesssim O(1)$. In this case, particle settling due to gravity is negligible, and can thus be ignored. Values of $r_0 > 1$ can in principle be obtained when $\rho_s \gg \rho_f$, such as is the case for aerosols or dust in accretion disks. However, particle settling should be taken into account in that limit. Therefore for simplicity, we also omit gravity from the particle momentum equation (4.2) to avoid the effect of settling on the dynamics of the system.

Lastly in this work, we drive the turbulence mechanically, by forcing the flow to be shear-unstable. We drive the mean flow using a constant body force given by $\mathbf{F} = F_0 \sin(k_s z)\hat{\mathbf{e}}_x$, where F_0 is the forcing amplitude and $k_s = 2\pi/L_z$ is the wavenumber corresponding to the domain height L_z. By selecting a non-cubic domain (where $L_x > L_z$), the Kolmogorov flow thus generated is linearly unstable for large enough Reynolds number (Beaumont, 1981).

4.2.1 Nondimensionalization

In what follows, we define the characteristic length and velocity scales to be

$$L_c = \frac{1}{k_s} = \frac{L_z}{2\pi} \quad \text{and} \quad U_c = \left(\frac{L_z F_0}{2\pi\rho_f}\right)^{1/2}, \tag{4.5}$$

and by construction, the typical eddy turnover time is

$$\tau_c = \left(\frac{L_z \rho_f}{2\pi F_0}\right)^{1/2}. \tag{4.6}$$

This choice effectively assumes a balance in the carrier fluid momentum equation between the inertial terms and the forcing, such that $\mathbf{u}\cdot\nabla u \sim F_0/\rho_f$. After using (4.5) and (4.6) to scale Eqs. (4.1)-(4.4), the nondimensional governing equations

are

$$\frac{\partial \hat{\mathbf{u}}}{\partial t} + \hat{\mathbf{u}} \cdot \nabla \hat{\mathbf{u}} = -\nabla \hat{p} + r_0 \hat{r} \frac{\hat{\mathbf{u}}_p - \hat{\mathbf{u}}}{T_p} + \frac{1}{Re} \nabla^2 \hat{\mathbf{u}} + \sin(z) \hat{\mathbf{e}}_x, \tag{4.7}$$

$$\frac{\partial \hat{\mathbf{u}}_p}{\partial t} + \hat{\mathbf{u}}_p \cdot \nabla \hat{\mathbf{u}}_p = \frac{\hat{\mathbf{u}} - \hat{\mathbf{u}}_p}{T_p} + \frac{1}{Re_p} \nabla^2 \hat{\mathbf{u}}_p, \tag{4.8}$$

$$\frac{\partial \hat{r}}{\partial t} + \nabla \cdot (\hat{\mathbf{u}}_p \hat{r}) = \frac{1}{Pe_p} \nabla^2 \hat{r}, \tag{4.9}$$

$$\nabla \cdot \hat{\mathbf{u}} = 0, \tag{4.10}$$

where the hatted quantities (as well as the independent variables) are now nondimensional, where $\hat{r} = r/r_0$, and where

$$T_p = \frac{\tau_p}{\tau_c} \tag{4.11}$$

is the nondimensional stopping time, which can be viewed as an estimate of the Stokes number based on the turnover time of the energetically-dominant eddies. Additionally, the diffusion terms are now characterized by a Reynolds number for the fluid Re, a Reynolds number for the particles Re_p, and the particle Péclet number Pe_p respectively defined by

$$Re = \frac{U_c L_c}{\nu}, \qquad Re_p = \frac{U_c L_c}{\nu_p}, \qquad Pe_p = \frac{U_c L_c}{\kappa_p}. \tag{4.12}$$

4.3 Numerical simulations

4.3.1 The PADDI-2F code

We use Direct Numerical Simulations to investigate the effects of preferential concentration in the model described in Section 4.2. We use a modified version of the pseudospectral PADDI code, which was originally developed to study

double-diffusive phenomena in oceanic contexts (Traxler et al., 2011b,a; Stellmach et al., 2010), and later extended to astrophysical applications (Moll et al., 2016; Garaud & Kulenthirarajah, 2016) and to particle-laden flows (Nasab & Garaud, 2020). PADDI-2F solves the governing equations (4.7)-(4.10) in spectral space. Specifically, diffusion terms are treated implicitly in spectral space, whereas both nonlinear and drag terms are first computed in real space, transformed into spectral space, and then, integrated explicitly using a third-order Adams-Bashforth backward-differencing scheme. Drag terms are computed in a way that ensures the total momentum is conserved (other than the dissipation terms) throughout the simulations.

The computational domain is triply-periodic, with $(L_x, L_y, L_z) = (4\pi, 2\pi, 2\pi)$ to ensure that the flow is linearly unstable under the selected forcing. All simulations are run until a statistically steady state has been reached, either starting from the initial conditions as described in Section 4.2, or starting from the end of another simulation at nearby parameters. Due to the high cost of running simulations in 3D and the resolution needed to resolve fine-scale particle structures, we restrict our simulations to $Re \leq 600$ and up to moderate values of the Stokes number $T_p \leq 0.03$ in which the two-fluid formalism is valid. Specifications of all simulations are listed in Table 4.1.

4.3.2 The effect of Re on the turbulence in the absence of particles

Shear-driven turbulence, created in the model setup selected here, is not as commonly used as homogeneous isotropic turbulence for the study of particle-laden flows. For this reason, we begin by presenting some of the properties of the fluid in the absence of particles, in particular with respect to variations of

the Reynolds number. Note that studies of the onset of turbulence in this type of Kolmogorov flow were presented by Platt et al. (1991); Tithof et al. (2017); van Veen & Goto (2016), while studies of stratified turbulence in the same system were presented by Garaud et al. (2015).

In this section, we therefore only use the momentum equation (4.7) and the divergence-free condition (4.10), and set $r_0 = 0$. We set the resolution of the 3D runs to be $768 \times 384 \times 384$ equivalent grid points in the $x-$, $y-$, and $z-$directions, respectively. Once the simulations have reached a statistically stationary state, they have a well-defined mean flow $\bar{u}(z)$ (where the overbar denotes a horizontal average) in the x direction that varies sinusoidally in the z direction, as expected. The amplitude of the mean flow is roughly equal to one, again as expected from the non-dimensionalization selected. It is maintained by a balance between the unidirectional forcing term and the turbulent Reynolds stresses, which are generated by the shear instability. Figure 4.1 illustrates this in the simulation with $Re = 600$.

Figure 4.1: Mean flow $\bar{u}$ and Reynolds stress $\overline{uw}$ as function of height z for a simulation in the absence of particles with $Re = 600$. The blue curve represents the temporal average of the gray curves, which have been extracted at various times after the system has reached a statistically steady state.

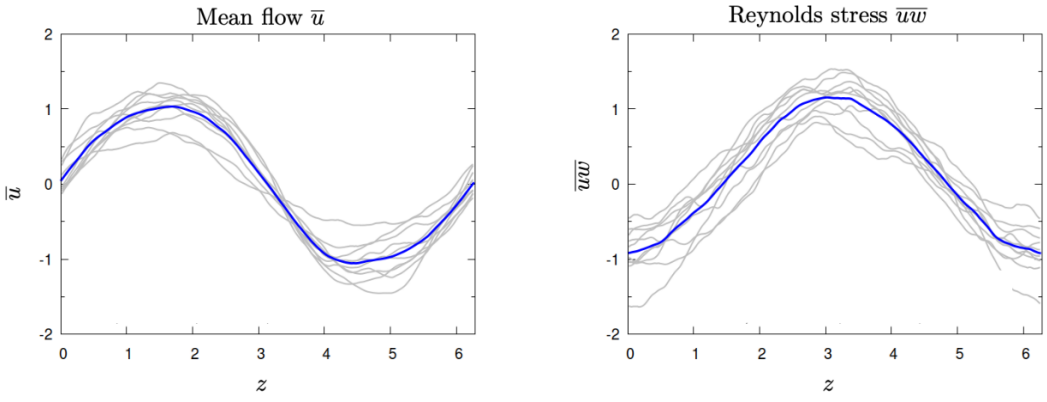

Energy in this system is input at the largest possible scale, and dissipated at

the smallest scales by the turbulence. In a statistically stationary state, and in the absence of particles, we have the balance

$$\langle \hat{\mathbf{F}} \cdot \hat{\mathbf{u}} \rangle = \langle \sin(z)\hat{u} \rangle = \hat{\epsilon} = Re^{-1} |\nabla \hat{\mathbf{u}}|^2, \tag{4.13}$$

where the angular brackets denote a volume average, and where $\hat{\epsilon}$ is the kinetic energy dissipation rate. The latter is roughly equal to 0.5 for all simulations without particles regardless of Re, consistent with the fact that the mean flow $\bar{u} \simeq \sin(z)$.

We can examine the power spectra of the fluid velocity field once the system has reached a statistically steady state, and compare the results for different Reynolds numbers. We define the power in mode $\mathbf{k}$ for a scalar quantity $\hat{\xi}$ (e.g. $\hat{u}, \hat{v}$, and $\hat{w}$) as

$$\mathcal{P}_{\hat{\xi}}(\mathbf{k}, t) = \tilde{\xi}(\mathbf{k}, t)\tilde{\xi}^*(\mathbf{k}, t) \tag{4.14}$$

where $\mathbf{k} = (k_x, k_y, k_z)$ is the nondimensional wavevector and $\tilde{\xi}(\mathbf{k}, t)$ and $\tilde{\xi}^*(\mathbf{k}, t)$ are the Fourier transform of $\hat{\xi}$ and its complex conjugate, respectively. For Figures 4.2, 4.4, 4.5, 4.6, and 4.8 we present the power spectra $\mathcal{P}_{\hat{\xi}}(|\mathbf{k}|, t)$ as a function of the total wavenumber $|\mathbf{k}| = (k_x^2 + k_y^2 + k_z^2)^{1/2}$, where $\mathcal{P}_{\hat{\xi}}(|\mathbf{k}|, t)$ is the power contained in all the modes whose amplitudes lie between $|\mathbf{k}|$ and $|\mathbf{k}| + 1$.

Figure 4.2 presents the power spectra of the total fluid velocity field $\mathcal{P}_{\hat{u}}(|\mathbf{k}|) + \mathcal{P}_{\hat{v}}(|\mathbf{k}|) + \mathcal{P}_{\hat{w}}(|\mathbf{k}|)$ extracted at an instant in time after the system has reached a statistically steady state for three simulations with $Re = 100, 300$, and 600, respectively. For sufficiently large Re, the system exhibits a well-known energy cascade whose inertial range scales as $|\mathbf{k}|^{-5/3}$, shown here by the black line for ease of comparison. This suggests that the turbulence is relatively isotropic at larger wavenumbers, a fact that has been verified by comparing the power spectra

of $\hat{u}$, $\hat{v}$, and $\hat{w}$ (not shown).

With this in mind, we can estimate the Taylor microscale and Kolmogorov scale using the standard formula from homogeneous isotropic turbulence. The non-dimensional Taylor microscale is given by $\hat{\lambda} = \sqrt{5/\hat{\epsilon}Re}\hat{U}_{rms}$ where $\hat{U}_{rms} \simeq 1$ is the nondimensional time-averaged rms velocity of the fluid (see Section 4.3.7 for detail). This corresponds to $k_\lambda = 2\pi/\hat{\lambda}$, which is equal to $k_\lambda \approx 20$ for $Re = 100$, $k_\lambda \approx 35$ for $Re = 300$, and $k_\lambda \approx 50$ for $Re = 600$. The associated Reynolds numbers based on the Taylor microscale are $Re_\lambda = \hat{U}^2_{rms}\sqrt{5Re/3\hat{\epsilon}} \simeq 18, 30$ and 45, respectively. Similarly, we can compute the Kolmogorov scale using the formula $\hat{\eta} = (\hat{\epsilon}Re^3)^{-1/4}$. This corresponds to $\hat{\eta} \simeq 0.037$ for $Re = 100$, $\hat{\eta} \simeq 0.016$ for $Re = 300$, and $\hat{\eta} \simeq 0.01$ for $Re = 600$. The product of largest resolved nondimensional wavenumber with the nondimensional Kolmogorov scale is larger than one for all cases (though admittedly quite close to one for $Re = 600$), showing that simulations are resolved.

In geophysical and astrophysical applications, Re and Re_λ are much larger, with an established inertial range spanning many orders of magnitude, which we do not see for the simulations presented here. Therefore, one must be careful about extrapolating the results obtained in this paper to systems with $Re \gg 10^3$ (see Section 4.5.2 for more details).

4.3.3 The effect of T_p on preferential concentration

We now add particles and explore how the various input parameters affect preferential concentration, and how this in turn alters the energetics of the system. We first look at how the non-dimensional stopping time, which is also a proxy for the Stokes number of the particles, affects the system by comparing a 3D simulation with a very low $T_p = 0.005$ to another at a higher $T_p = 0.03$. To

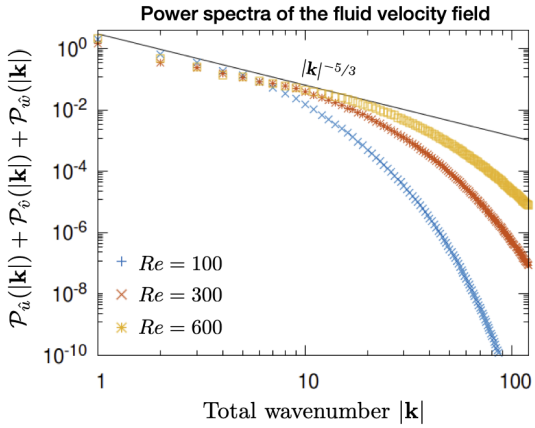

Figure 4.2: Instantaneous power spectra of the total fluid velocity field as function of $|\mathbf{k}|$ for simulations in the absence of particles for $Re = 100$, 300, and 600. The black solid line scales as $|\mathbf{k}|^{-5/3}$.

do so, we use the PADDI-2F code using Eqs. (4.7)–(4.10), with the remaining parameters set as $r_0 = 0.1, Re = 100, Re_p = 600$, and $Pe_p = 600$. The resolution and domain size for the simulations are set to $768 \times 384 \times 384$ equivalent grid points, and as before, $L_x = 4\pi$ and $L_y = L_z = 2\pi$ (see Table 4.1 for more details).

We present snapshots in Figure 4.3 of the particle concentration field after the system has reached a statistically steady state. In the volume renderings shown in Figures 4.3(a) and 4.3(b), we highlight areas of relatively higher particle concentration in red. In both simulations the particle field develops sheet-like structures which appear to be about the same size, but denser for the high T_p case. We can see the particle structures in more detail in Figures 4.3(c) and 4.3(d), which show the particle concentration deviation from the mean (namely, $\hat{r} - 1$) in a slice taken at $y = 0$. We clearly see that the denser particle structures indeed appear to be the same size for both simulations. The densest structures for the high T_p case have values of $\hat{r} - 1 \approx 3$ compared to $\hat{r} - 1 \approx 0.5$ for structures found in the low T_p case.

The fact that preferential concentration is more efficient at higher values of T_p

recovers the well-known results of Maxey (1987), which are expressed as follows in the two-fluid formalism. Using the particle momentum equation (4.9), we can express $\hat{\mathbf{u}}_p$ in terms of $\hat{\mathbf{u}}$ and T_p using an asymptotic expansion in T_p:

$$\hat{\mathbf{u}}_p = \hat{\mathbf{u}} - T_p\left(\hat{\mathbf{u}}\cdot\nabla\hat{\mathbf{u}} + \frac{\partial\hat{\mathbf{u}}}{\partial t} - \frac{1}{Re_p}\nabla^2\hat{\mathbf{u}}\right) + O(T_p^2). \tag{4.15}$$

Taking the divergence of (4.15), we then obtain

$$\nabla\cdot\hat{\mathbf{u}}_p = -T_p\nabla\cdot(\hat{\mathbf{u}}\cdot\nabla\hat{\mathbf{u}}) + O(T_p^2), \tag{4.16}$$

which shows that $\nabla\cdot\hat{\mathbf{u}}_p$ is non zero even though $\nabla\cdot\hat{\mathbf{u}} = 0$, and furthermore depends linearly on T_p for small T_p. It is easy to see (from Eq. 4.9) that the particle concentration grows (or decays) exponentially since

$$\frac{\partial\hat{r}}{\partial t} = -\hat{r}(\nabla\cdot\hat{\mathbf{u}}_p) + ..., \tag{4.17}$$

showing that the growth or decay rate of $\hat{r}$ is given by $|\nabla\cdot\hat{\mathbf{u}}_p|$. Figure 4.3 compares the particle concentration enhancement $\hat{r}-1$ (panels 4.3(c) and 4.3(d)) to the value of $\nabla\cdot\hat{\mathbf{u}}_p$ (panels 4.3(e) and 4.3(f)) at the same time. We see that areas where $\nabla\cdot\hat{\mathbf{u}}_p < 0$ (shown in blue) correspond to regions where $\hat{r}-1$ is maximal, while regions with $\nabla\cdot\hat{\mathbf{u}}_p > 0$ (shown in red) correspond to regions where $\hat{r}$ is close to 0 (equivalently, $\hat{r}-1$ is close to -1), as expected from the argument above.

We next compare the power spectra (using Eq. 4.14) of the particle concentration and fluid velocity fields for simulations with varying T_p, with the remaining parameters fixed as $r_0 = 0.1, Re = 100, Re_p = 600$ and $Pe_p = 600$. Figure 4.4(a) shows the power spectrum of the total fluid velocity field $\mathcal{P}_{\hat{u}}(|\mathbf{k}|)+\mathcal{P}_{\hat{v}}(|\mathbf{k}|)+\mathcal{P}_{\hat{w}}(|\mathbf{k}|)$. The solid black line represents the Kolmogorov spectrum given by $|\mathbf{k}|^{-5/3}$.

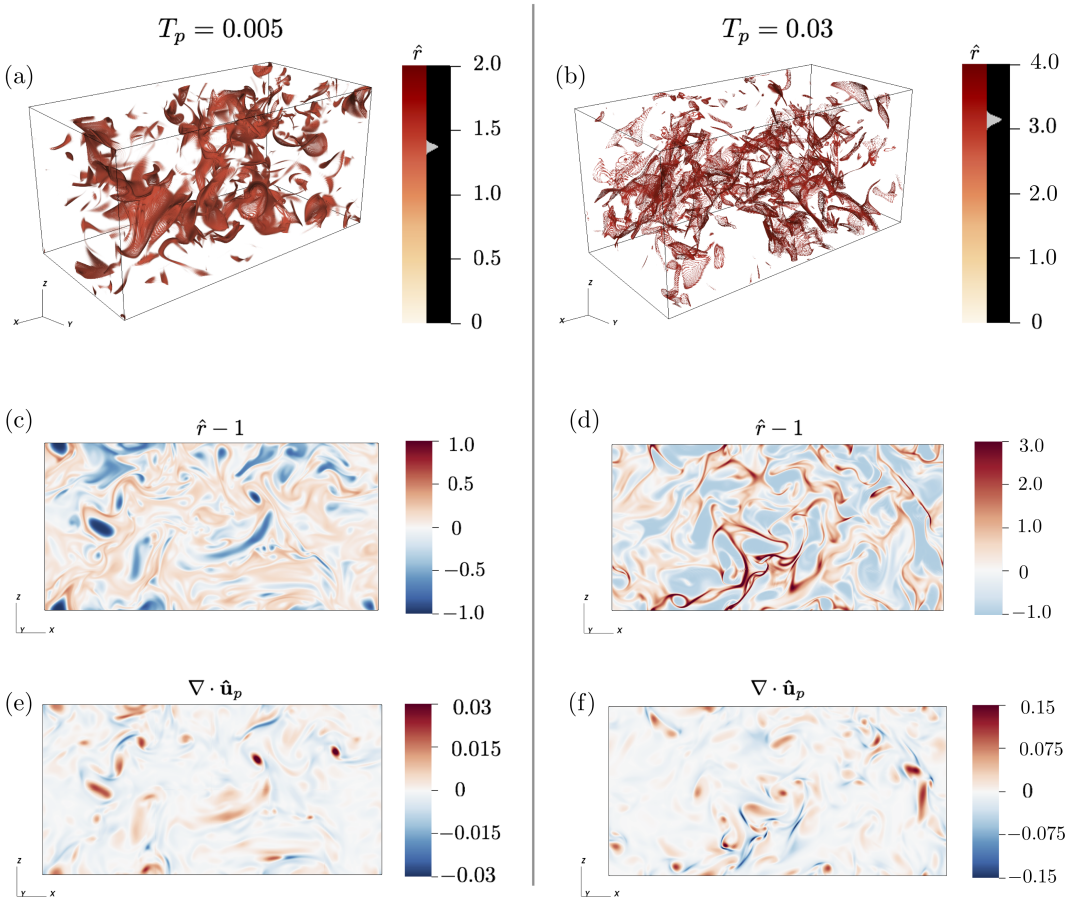

Figure 4.3: Comparison of particle concentration snapshots for low $T_p = 0.005$ (left column) and high $T_p = 0.03$ (right column) simulations. Each snapshot was extracted once the system has reached a statistically steady state. (a)-(b): volume rendering of $\hat{r}$; (c)-(d): snapshots of the particle concentration enhancement $\hat{r} - 1$ at $y = 0$; (e)-(f): snapshots of $\nabla \cdot \hat{\mathbf{u}}_p$ at $y = 0$. The remaining parameters are: $r_0 = 0.1, Re = 100, Re_p = 600, Pe_p = 600$.

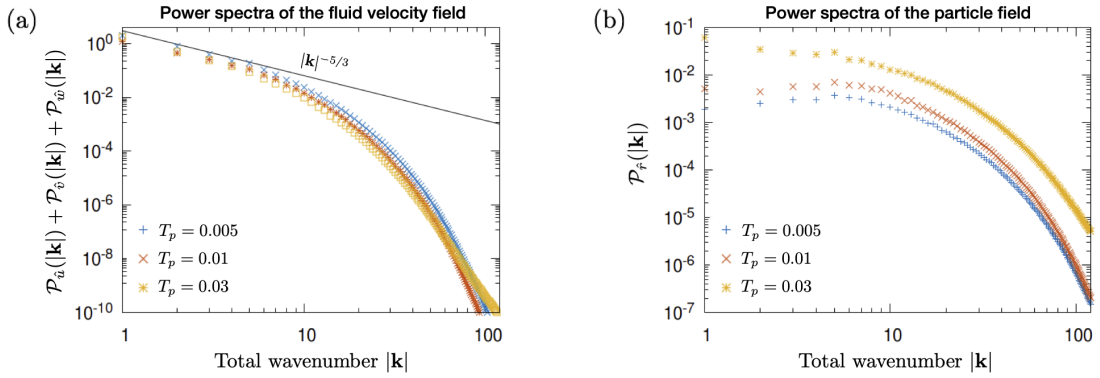

Figure 4.4: Instantaneous power spectra of (a) the total fluid velocity field and (b) the particle concentration field as a function of the total wavenumber $|\mathbf{k}|$ for varying T_p. The remaining parameters are $r_0 = 0.1, Re = 100, Re_p = 600$, and $Pe_p = 600$.

Although there is a subtle decrease in power across all scales for larger T_p, the velocity spectrum appears to be overall relatively unaffected.

Figure 4.4(b) shows the power spectrum of the particle concentration $\mathcal{P}_{\hat{r}}(|\mathbf{k}|)$. We see that increasing T_p causes an increase in $\mathcal{P}_{\hat{r}}(|\mathbf{k}|)$ at all scales, with the exception of the $\mathbf{k} = \mathbf{0}$ mode whose amplitude instead decreases (not shown here). This is consistent with our expectation that increasing inertia causes an increase in preferential concentration, and is directly related to the snapshots in Figure 4.3: comparable-sized particle structures are denser (higher $\hat{r}$) for large T_p than for small T_p.

4.3.4 The effect of r_0 on preferential concentration

We next look at the effect of the particle mass loading fraction r_0 on the energetics of the system. We set $T_p = 0.01, Re = 100, Re_p = 600$, and $Pe_p = 600$ (see Table 4.1 for more details) and present the power spectra of the particle concentration and total fluid velocity fields (using Eq. 4.14) in Figures 4.5(a) and 4.5(b), respectively.

Turning first to the power spectrum of the velocity field in Figure 4.5(a), we see that r_0 has a strong effect on the total energy of the turbulent flow. The inertial range still shows the usual $|\mathbf{k}|^{-5/3}$ power law as in the case without particles ($r_0 = 0$ with $Re = 100, Re_p = 600, Pe_p = 600$ in Figure 4.2), but its amplitude decreases with increasing r_0. In order to understand why increasing r_0 reduces the turbulent energy, note that in a statistically stationary state, the momentum equation (4.1) reaches a balance between the inertial terms and body force terms, expressed dimensionally as $\rho_f(\mathbf{u} \cdot \nabla \mathbf{u}) \sim \mathbf{F}$. With the addition of particles that are well-coupled to the fluid (i.e. if $T_p \to 0$), the dominant balance becomes $(\rho_f + \rho_p)(\mathbf{u} \cdot \nabla \mathbf{u}) \sim \mathbf{F}$. In the nondimensionalization presented in Section 4.2.1, this balance implies $(1 + r_0)\hat{\mathbf{u}}^2 \simeq O(1)$. With this in mind, we can then expect that $\mathcal{P}_{\hat{u}}(|\mathbf{k}|) + \mathcal{P}_{\hat{v}}(|\mathbf{k}|) + \mathcal{P}_{\hat{w}}(|\mathbf{k}|)$ ought to scale like $1/(1+r_0)$ at the injection scale. The scaling is confirmed in Figure 4.5 for $r_0 = 0.1, r_0 = 1$, and $r_0 = 10$ given by the solid, dashed, and dotted lines, respectively.

Figure 4.5(b) shows the power spectrum of the particle concentration field $\mathcal{P}_{\hat{r}}(|\mathbf{k}|)$, and we see that larger r_0 corresponds to smaller $\mathcal{P}_{\hat{r}}(|\mathbf{k}|)$ across all scales (except the $\mathbf{k} = \mathbf{0}$ mode which is not shown). This is consistent with the fact that larger r_0 results in a decrease in the turbulence intensity (and therefore preferential concentration) across all scales, as observed from the velocity power spectrum.

4.3.5 The effect of Re on preferential concentration

In this section, we investigate how varying the fluid Reynolds number affects the energetics, while fixing the other parameters to be $T_p = 0.01$, $r_0 = 0.1, Re_p = 600$, and $Pe_p = 600$ (see Table 4.1 for more details). Figures 4.6(a) and 4.6(b) show the power spectra of the total fluid velocity and particle concentration fields, respectively (using Eq. 4.14).

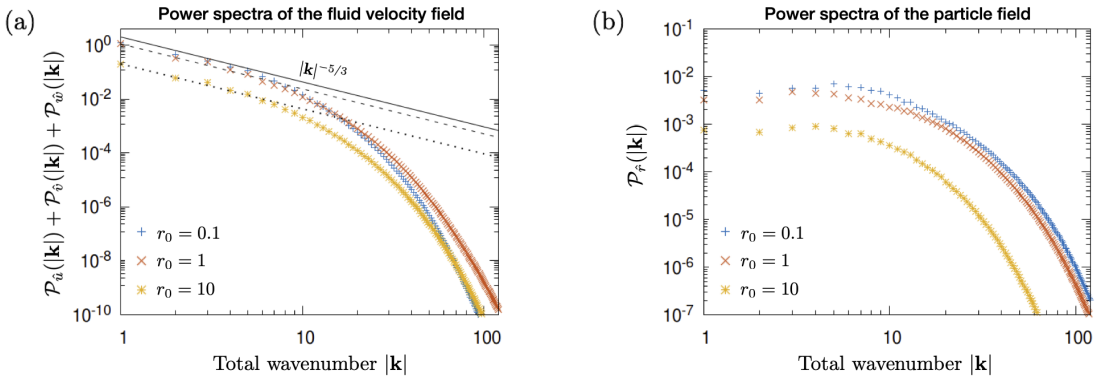

Figure 4.5: Instantaneous power spectra of (a) the total fluid velocity field and (b) the particle concentration field as a function of the total wavenumber $|\mathbf{k}|$ for varying r_0. The remaining parameters are $T_p = 0.01, Re = 100, Re_p = 600$, and $Pe_p = 600$. The solid, dashed, and dotted lines represents the predicted scaling for the power at the injection scale for $r_0 = 0.1, 1$, and 10, respectively (see main text for details).

In Figure 4.6(a), the velocity spectra shown are more or less indistinguishable from those of the corresponding fluid-only simulations presented in Section 4.3.2. This is not surprising since the value of $r_0 = 0.1$ chosen for these simulations is quite small. Because a larger Re extends the inertial range, finer scales of turbulence are generated. Consequently in Figure 4.6(b), we also see substantially more power in the particle density field at smaller scales when Re increases. More precisely, we see that the spectrum of the particle concentration increases mildly with $|\mathbf{k}|$ at low wavenumber, and appears to peak around $|\mathbf{k}| \simeq k_\lambda/3$. Beyond that, $\mathcal{P}_{\hat{r}}(|\mathbf{k}|)$ drops rapidly with increasing wavenumber. This suggests that the typical scale of particle structures ought to be more closely related to the Taylor microscale than to the Kolmogorov scale. This is confirmed in the snapshots of the particle concentration enhancement $(\hat{r} - 1)$ shown in Figure 4.7, which compare simulations with $Re = 100$ and $Re = 600$. The finer scales of turbulence for larger Re cause the denser particle structures to appear overall more fragmented and convoluted. We note, however, that the densest filamentary regions (shown in

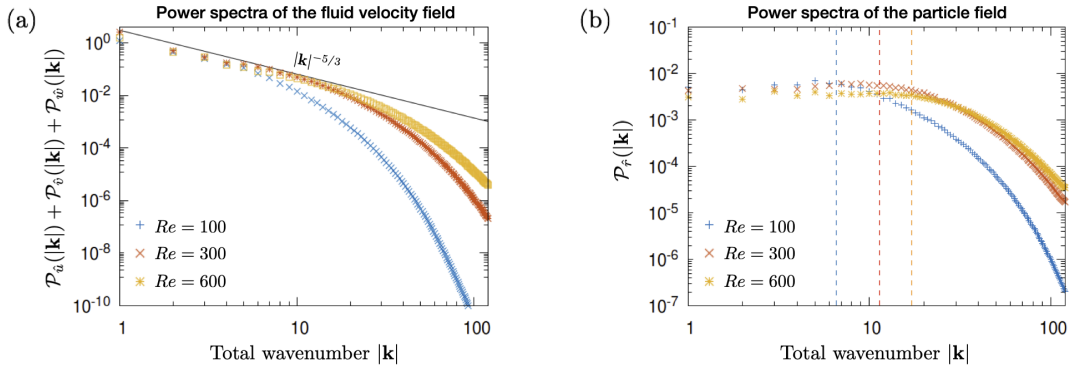

Figure 4.6: Instantaneous power spectra of (a) the total fluid velocity field and (b) the particle concentration field as a function of the total wavenumber $|\mathbf{k}|$ for varying Re. The remaining parameters are $T_p = 0.01, r_0 = 0.1, Re_p = 600$, and $Pe_p = 600$. On the right plot, we mark $k_\lambda/3$ given by the vertical dashed line with the same color as the corresponding simulation.

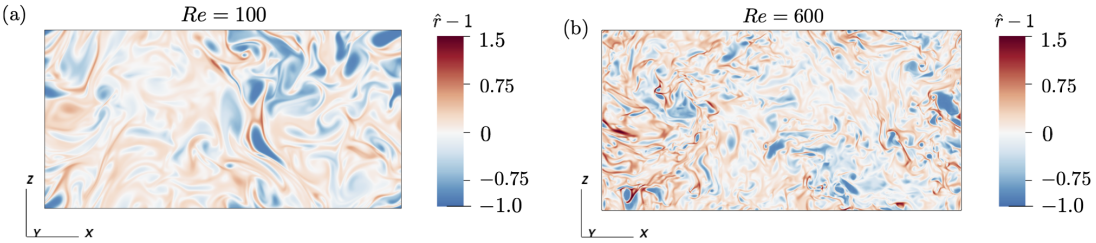

Figure 4.7: Snapshots of the particle concentration enhancement above the mean $\hat{r} - 1$ for two different simulations with $Re = 100$ and $Re = 600$. The remaining parameters are $T_p = 0.01, r_0 = 0.1, Re_p = 600$, and $Pe_p = 600$.

dark red) have comparable thickness for varying Re.

4.3.6 The effect of Pe_p and Re_p on preferential concentration

Finally, we examine how the particle diffusion coefficients Pe_p and Re_p affect the energetics of the system. As described in Section 4.2, the particle concentration and momentum diffusivities are necessary when modeling the particles as a continuum, but their origin is grounded in the notion that the particle velocities

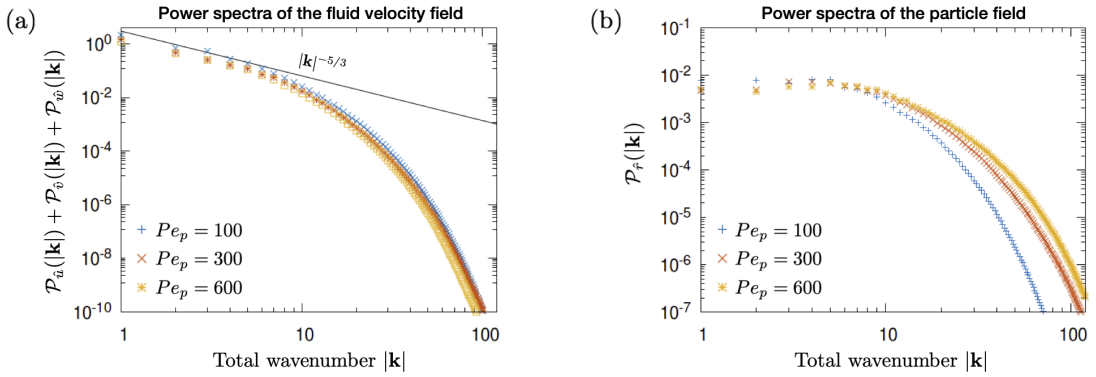

Figure 4.8: Instantaneous power spectra of (a) the total fluid velocity field and (b) the particle concentration field as a function of the total wavenumber $|\mathbf{k}|$ for varying Pe_p. The remaining parameters are $T_p = 0.01, r_0 = 0.1$, $Re = 100$, and $Re_p = Pe_p$.

have a stochastic component in addition to the mean $\hat{\mathbf{u}}_p$. Since the origin of the particle diffusivity is likely the same as that of the momentum diffusivity, we may expect Pe_p and Re_p to be related, and close to one another. In what follows, we take $Pe_p = Re_p$ for simplicity.

Figure 4.8 shows the power spectra of the particle concentration field and the total fluid velocity field. In Figure 4.8(b), we see that a larger Pe_p (equivalently, a lower particle diffusivity) results in significantly larger $\mathcal{P}_{\hat{r}}(|\mathbf{k}|)$ across all scales, and thus, the presence of smaller-scale structures in the particle concentration field. By contrast, we see in Figure 4.8(a) that Pe_p does not affect the velocity power spectrum significantly, other than a slight decrease in energy across all scales for larger Pe_p.

4.3.7 Quantifying particle concentration enhancement

In what follows, we quantify particle concentration enhancement by first defining several terms:

$$\hat{r}_{sup}(t) = \max_{\mathbf{x}} \hat{r}(\mathbf{x}, t) \tag{4.18}$$

Symbol	T_p	r_0	Re	Pe_p	$\hat{r}_{sup}$	$\hat{r}_{rms}$	$\hat{U}_{rms}$	b
–	–	–	100	–	–	–	2.42 ± 0.05	–
–	–	–	300	–	–	–	2.43 ± 0.16	–
–	–	–	600	–	–	–	2.50 ± 0.18	–
○	0.005	0.1	100	1000	2.04 ± 0.11	0.23 ± 0.005	2.17 ± 0.08	10.92 ± 0.18
○	0.005	0.1	100	600	1.92 ± 0.11	0.22 ± 0.01	2.28 ± 0.07	18.04 ± 0.05
○	0.005	0.1	600	1000	3.84 ± 0.43	0.29 ± 0.01	2.26 ± 0.08	8.14 ± 0.01
△	0.005	1	600	1000	2.35 ± 0.18	0.21 ± 0.01	1.80 ± 0.09	14.79 ± 0.03
□	0.005	10	600	1000	1.27 ± 0.03	0.06 ± 0.004	0.71 ± 0.01	51.72 ± 0.85
○	0.01	0.1	100	100	1.85 ± 0.18	0.22 ± 0.03	2.20 ± 0.06	13.65 ± 0.05
○	0.01	0.1	100	300	2.56 ± 0.35	0.31 ± 0.03	2.20 ± 0.09	9.25 ± 0.01
○	0.01	0.1	100	600	3.17 ± 0.36	0.37 ± 0.03	2.22 ± 0.025	10.18 ± 0.01
○	0.01	0.1	300	600	5.61 ± 1.21	0.41 ± 0.014	2.31 ± 0.07	5.58 ± 0.004
○	0.01	0.1	600	600	6.36 ± 1.14	0.40 ± 0.01	2.16 ± 0.056	5.52 ± 0.007
△	0.01	1	100	1000	2.40 ± 0.27	0.23 ± 0.02	1.58 ± 0.025	11.60 ± 0.025
△	0.01	1	100	600	2.10 ± 0.17	0.23 ± 0.01	1.63 ± 0.02	13.96 ± 0.03
△	0.01	1	600	600	2.93 ± 0.22	0.26 ± 0.01	1.69 ± 0.02	9.32 ± 0.01
□	0.01	10	100	1000	1.53 ± 0.08	0.10 ± 0.006	0.82 ± 0.05	33.91 ± 0.21
□	0.01	10	100	600	1.31 ± 0.03	0.09 ± 0.002	0.69 ± 0.004	31.77 ± 0.30
□	0.01	10	600	600	1.39 ± 0.05	0.08 ± 0.002	0.69 ± 0.002	45.47 ± 0.48
○	0.03	0.1	100	300	9.81 ± 2.50	0.64 ± 0.03	2.16 ± 0.06	2.50 ± 0.003
○	0.03	0.1	100	600	8.46 ± 1.81	0.61 ± 0.014	2.05 ± 0.07	2.92 ± 0.004
△	0.03	1	100	1000	6.95 ± 0.81	0.49 ± 0.02	1.57 ± 0.03	3.36 ± 0.01

Table 4.1: Characteristics of the numerical simulations. The first column represents the markers for Figures 4.10, 4.11, and 4.13. The second to fifth columns show T_p, r_0, Re, and Pe_p (where we have set $Re_p = Pe_p$). The sixth to eighth columns show temporally averaged values for $\hat{r}_{sup}$, $\hat{r}_{rms}$, and $\hat{U}_{rms}$ once the system has reached a statistically steady state, and the errors represent a standard deviation around the mean. The last column corresponds to the slope b and its standard error of the exponential tail of the pdfs presented in Section 4.4.2. All 3D simulations were run with $(L_x \times L_y \times L_z) = (4\pi \times 2\pi \times 2\pi)$ with the corresponding number of mesh points used in each direction as $(N_x \times N_y \times N_z) = (768 \times 384 \times 384)$.

representing the maximum particle concentration across the domain,

$$\hat{r}_{rms}(t) = \left[\frac{1}{L_x L_y L_z}\iiint (\hat{r}-1)^2\, dxdydz\right]^{1/2}, \tag{4.19}$$

defined as the standard deviation around the mean particle density $\hat{r} = 1$, and the rms fluid velocity defined as

$$\hat{U}_{rms}(t) = \left[\frac{1}{L_x L_y L_z}\iiint [\hat{u}^2(\mathbf{x},t) + \hat{v}^2(\mathbf{x},t) + \hat{w}^2(\mathbf{x},t)]\, dxdydz\right]^{1/2}. \tag{4.20}$$

We first look at how the two measures of particle concentration enhancement defined above, as well as the rms fluid velocity, vary with respect to T_p, r_0, Re, and Pe_p (assuming as above that $Re_p = Pe_p$). For each simulation presented, we take a temporal average of the quantities defined by Eqs. (4.18) – (4.20) after the system has reached a statistically steady state over a time range Δt, and report the means as $\hat{r}_{sup}, \hat{r}_{rms}$, and $\hat{U}_{rms}$ in Table 4.1. We then take the standard deviation around this temporal average as an estimate of the errorbar (quantifying the variability). Figure 4.9 presents the temporally averaged values of $\hat{r}_{sup} - 1$, $\hat{r}_{rms}$, and $\hat{U}_{rms}$ for selected simulations. In Figure 4.9(a), we present simulations for varying T_p, while holding $r_0 = 0.1, Re = 100, Re_p = 600$, and $Pe_p = 600$ constant. We see that both $\hat{r}_{sup} - 1$ and $\hat{r}_{rms}$ increase with T_p, while $\hat{U}_{rms}$ is overall unaffected. This is consistent with the observation in Section 4.3.3 that T_p only has a small effect on the overall power spectrum of the turbulence, but directly controls the rate of preferential concentration. In Figure 4.9(b), r_0 is varied, while $T_p = 0.01, Re = 100, Re_p = 600$, and $Pe_p = 600$ are held constant. We see that all quantities decrease with increasing r_0. This can be explained by the fact that an increase in r_0 corresponds to a decrease in the turbulent fluid velocity, resulting in a subsequent decrease in the particle concentration

enhancement (see Section 4.3.4). Moving on to Figure 4.9(c) where Re is varied while $T_p = 0.01, r_0 = 0.1, Re_p = 600$, and $Pe_p = 600$ are held constant, we see that $\hat{U}_{rms}$ and $\hat{r}_{rms}$ are overall unchanged, at least within the range of Re shown. In contrast, we see a slight increase of $\hat{r}_{sup} - 1$ with Re. Finally in 4.9(d), where Pe_p (and Re_p) is varied while $T_p = 0.01, r_0 = 0.1$, and $Re = 100$ are held constant, we see that both $\hat{r}_{sup} - 1$ and $\hat{r}_{rms}$ increase with Pe_p, while $\hat{U}_{rms}$ is unchanged (see Section 4.3.6). Therefore, we see that the quantities $\hat{r}_{sup}$, $\hat{r}_{rms}$, and $\hat{U}_{rms}$ for varying parameters are consistent with the spectra shown in Sections 4.3.3-4.3.6.

4.4 Predictive model

As discussed in Section 4.1, Nasab & Garaud (2020) found that the maximum particle concentration in a fluid where the turbulence is driven by the particle Rayleigh-Taylor instability scales as $u_{rms}^2 \tau_p / \kappa_p$, and presented theoretical arguments of dominant balance that support this law. For pedagogical purposes, we reproduce the arguments here, and then verify whether the same scaling law applies for particles in mechanically-driven (shear-induced) turbulence as studied in this paper.

We start with the particle concentration equation (4.9) and substitute $\hat{r} = 1 + \hat{r}'$ to get

$$\frac{\partial \hat{r}'}{\partial t} + (1 + \hat{r}')\nabla \cdot \hat{\mathbf{u}}_p + \hat{\mathbf{u}}_p \cdot \nabla \hat{r}' = \frac{1}{Pe_p} \nabla^2 \hat{r}', \tag{4.21}$$

where $\hat{r}'$ is the particle concentration enhancement over the mean.

As in Nasab & Garaud (2020), we assume that in regions of maximal concentration enhancement there is a dominant balance between the inertial concentration

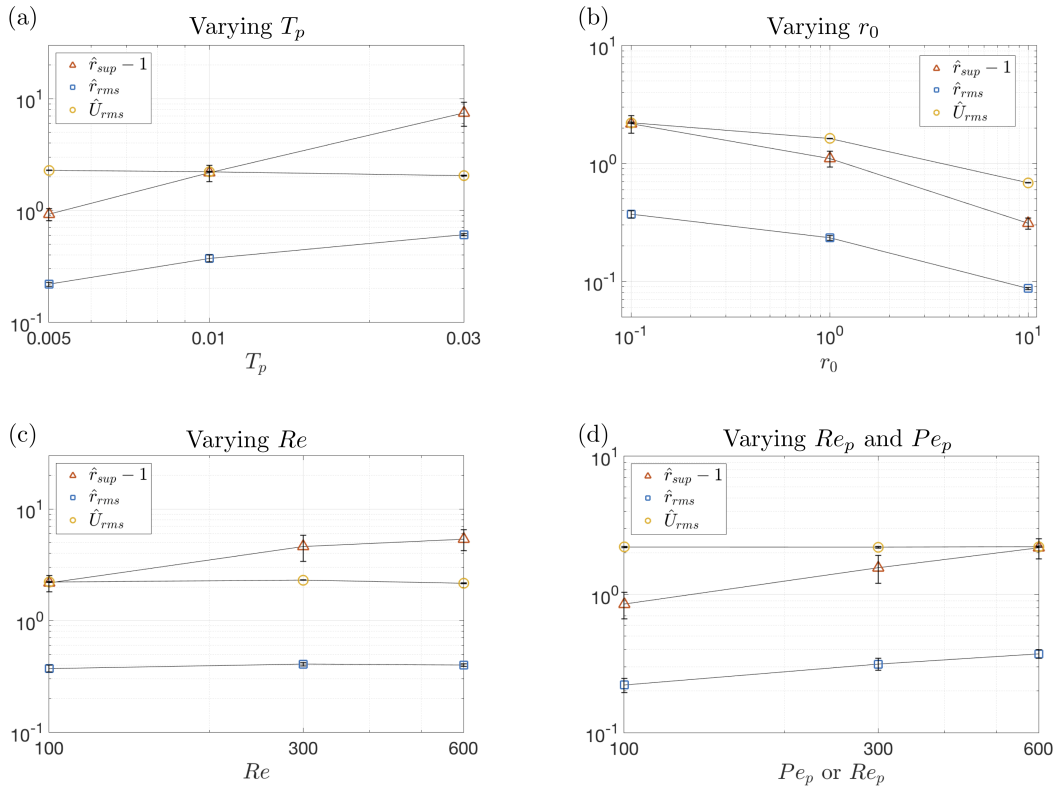

Figure 4.9: Temporally averaged maximum and typical particle concentration enhancement ($\hat{r}_{sup} - 1$ and $\hat{r}_{rms}$, respectively) and the temporally averaged rms fluid velocity $\hat{U}_{rms}$ for (a) varying T_p, (b) varying r_0, (c) varying Re, and (d) varying Pe_p and Re_p from simulations that have reached a statistically steady state. Error bars represent one standard deviation around the mean. Unless otherwise stated, $T_p = 0.01, r_0 = 0.1$, $Re = 100$, $Pe_p = 600$, and $Re_p = 600$ (see main text). More details of the simulations can be found in Table 4.1.

term and the diffusion term expressed as

$$\nabla \cdot \hat{\mathbf{u}}_p \sim \frac{1}{Pe_p} \nabla^2 \hat{r}'. \tag{4.22}$$

Using Eq. (4.16) in Eq. (4.22), we obtain

$$-T_p \nabla \cdot (\hat{\mathbf{u}} \cdot \nabla \hat{\mathbf{u}}) \sim \frac{1}{Pe_p} \nabla^2 \hat{r}'. \tag{4.23}$$

Assuming that the characteristic lengthscale involved in the inertial term and the diffusive term are the same, dimensional analysis reveals that

$$\hat{r}' \sim \hat{U}_{rms}^2 T_p Pe_p, \tag{4.24}$$

where $\hat{U}_{rms}$ represent the characteristic fluid velocity of the system (see Eq. 4.20). Dimensionally, this expression becomes

$$\left(\frac{\rho_p'}{\bar{\rho}_p} \right)_{max} \sim \frac{u_{rms}^2 \tau_p}{\kappa_p}, \tag{4.25}$$

where $\rho_p' = \hat{r}' r_0 \rho_s$ is the local particle density enhancement over the mean $\bar{\rho}_p = r_0 \rho_s$ (see Nasab & Garaud, 2020 for more details) and u_{rms} is the dimensional rms fluid velocity. We now have a scaling law relating particle concentration enhancement $\hat{r}'$ to only three properties of the flow: the characteristic fluid velocity, the particle stopping time, and the particle diffusivity.

4.4.1 Maximum particle concentration enhancement

As in Nasab & Garaud (2020), we compare the scaling law (4.24) to our selected measure of maximum particle concentration enhancement $\hat{r}_{sup} - 1$ (see Eq. 4.18). In Figure 4.10, we present $\hat{r}_{sup} - 1$ versus $\hat{U}_{rms}^2 T_p Pe_p$ (with the legend and

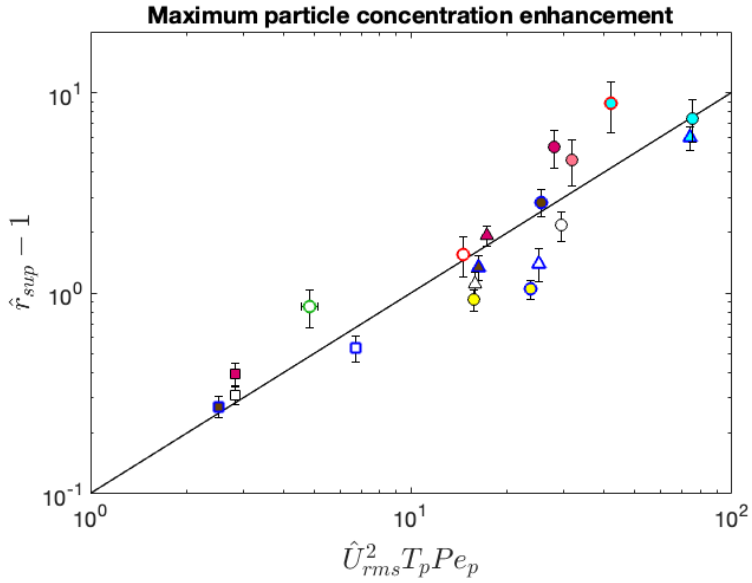

Figure 4.10: Maximum particle concentration enhancement over the mean as function of $\hat{U}^2_{rms} T_p Pe_p$ with varying parameters (i.e. T_p, r_0, Re, Re_p, and Pe_p). The black solid line represents $\hat{r}_{sup} - 1 = (1/10)\hat{U}^2_{rms} T_p Pe_p$. The legend and details of simulations can be found in Table 4.1.

simulation details found in Table 4.1). Each point corresponds to one simulation, where the values of $\hat{r}_{sup}$ and $\hat{U}_{rms}$ were extracted after the system has reached a statistically steady state. Various marker types represent varying T_p, r_0, Re, Pe_p, and Re_p: the color represents the value for T_p or Re, the shape represents r_0, and colored outlines represent Pe_p (or equivalently Re_p, since $Re_p = Pe_p$). The solid line represents the scaling $\hat{r}' \sim \hat{U}^2_{rms} T_p Pe_p$.

Our main conclusion is that the scaling law proposed by Nasab & Garaud (2020) in the context of the particle-driven convective instability also holds more generally in mechanically-driven turbulent flows, which is perhaps not surprising, but needed to be established. As expected, we see points for larger T_p or smaller r_0 have larger $\hat{r}_{sup}$, while larger r_0 results in a smaller $\hat{U}_{rms}$, and therefore smaller $\hat{r}_{sup}$, as discussed in Section 4.3.7. We also see that for larger Re, $\hat{U}_{rms}$ increases slightly, resulting in larger $\hat{r}_{sup}$.

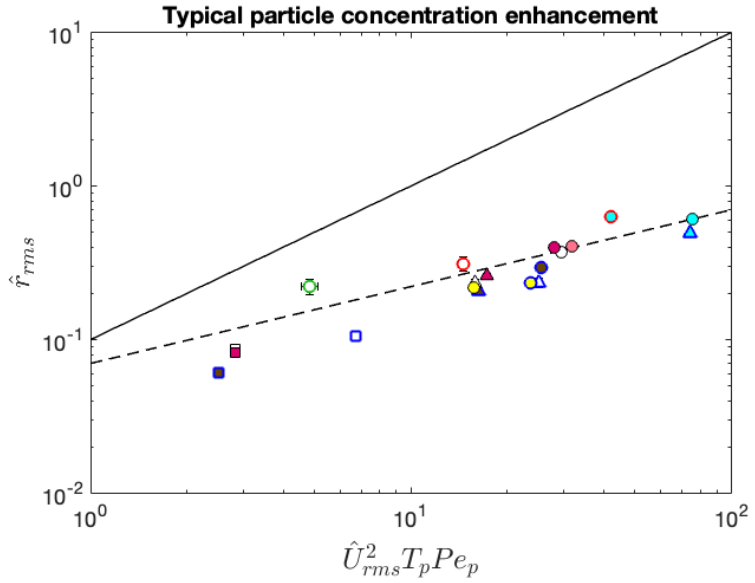

Figure 4.11: Typical particle concentration enhancement over the mean as a function of $\hat{U}^2_{rms} T_p Pe_p$ with varying parameters (i.e. T_p, r_0, Re, Re_p, and Pe_p). The black dotted line represents $\hat{r}_{rms} = (0.07)\hat{U}_{rms}(T_p Pe_p)^{1/2}$ and the solid line represents $\hat{r}_{rms} = (1/10)\hat{U}^2_{rms} T_p Pe_p$. The legend and details of simulations can be found in Table 4.1.

4.4.2 Typical particle concentration enhancement

In our previous work (Nasab & Garaud, 2020), we also showed that the typical particle concentration enhancement $\hat{r}_{rms}$ did not follow the scaling law given by Eq. (4.24), but instead scaled like

$$\hat{r}_{rms} \sim \sqrt{\hat{U}^2_{rms} T_p Pe_p}, \tag{4.26}$$

which dimensionally is

$$\left(\frac{\rho'_p}{\bar{\rho}_p}\right)_{rms} \sim \left(\frac{u^2_{rms}\tau_p}{\kappa_p}\right)^{1/2}. \tag{4.27}$$

We see that this result also holds for this work in Figure 4.11. The data points do not follow the scaling law (4.24) shown by the solid line, and instead follow the dashed line representing $\hat{r}_{rms} \sim \hat{U}_{rms}\sqrt{T_p Pe_p}$.

As argued by Nasab & Garaud (2020), the fact that $\hat{r}_{rms}$ depends on the same *combination* of parameters as $\hat{r}_{sup} - 1$ (albeit with a different power law) strongly suggests that the entire pdf of the concentration enhancement depends on the combination $\hat{U}_{rms}^2 T_p Pe_p$. To see whether a similar argument applies here, Figure 4.12 presents pdfs of $\hat{r}$ for selected simulations of varying (a) T_p and (b) r_0 (with simulation details in Table 4.1). These pdfs represent the probability of one pixel in the simulation to have a concentration whose value lies between $\hat{r}$ and $\hat{r} + \Delta\hat{r}$, where $\Delta\hat{r} = 0.002$. The pdf would take the form of a delta function centered on $\hat{r} = 1$ in the absence of preferential concentration ($T_p \to 0$), since the particle density in that case remains equal to one everywhere and at all times.

On the other hand when preferential concentration is present, the pdf broadens as the particle density becomes more inhomogeneous. We see in Figure 4.12(a), where T_p is varied while holding $r_0 = 0.1, Re = 100, Pe_p = 600$, and $Re_p = 600$ constant, that the pdf appears relatively narrow around the mean value $\hat{r} = 1$ for small T_p. As T_p increases, the spatial distribution of the particles becomes more heterogeneous due to preferential concentration, and the pdf widens considerably. We also see an increase in the probability of events of no particles (when $\hat{r} \simeq 0$) and the appearance of an elongated tail capturing extreme events where the particle concentration is largest. The tail is exponential, of the form $p(\hat{r}) \propto e^{-b\hat{r}}$ (see Nasab & Garaud, 2020). Moving to Figure 4.12(b) in which r_0 is varied while $T_p = 0.01, Re = 100, Pe_p = 600$, and $Re_p = 600$, we see that increasing r_0 causes the pdf to become narrower. This is consistent with the fact that a larger r_0 lowers the amplitude of the turbulence in the system, and consequently, weakens preferential concentration.

Nasab & Garaud (2020) studied more quantitatively the exponential tail of the pdf, which seems to be almost ubiquitous, and found that its decay rate b scales as

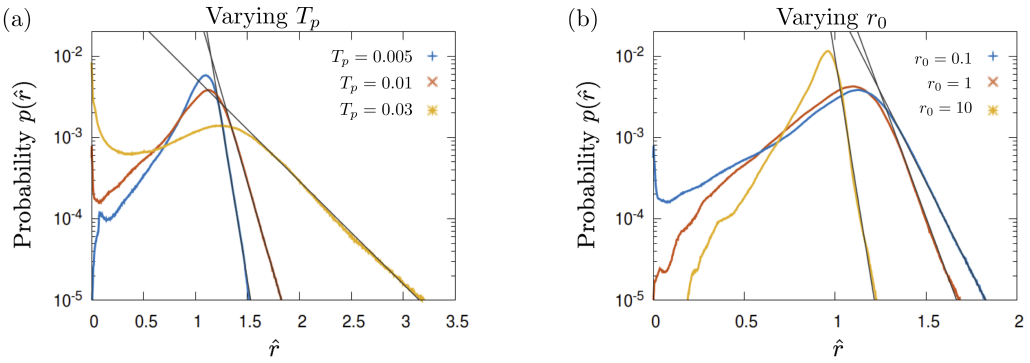

Figure 4.12: Probability distribution functions for $\hat{r}$, computed from simulations that have reached a statistically steady state (a) for varying T_p with $r_0 = 0.1, Re = 100, Pe_p = 600, Re_p = 600$ and (b) for varying r_0 with $T_p = 0.01, Re = 100, Pe_p = 600, Re_p = 600$. The gray lines fit the tail of each pdf and are of the form $p(\hat{r}) \propto e^{-b\hat{r}}$. Values of b and simulation details can be found in Table 4.1.

$(\hat{U}^2_{rms} T_p Pe_p)^{-1/2}$. In Figure 4.13, we present b as a function of $\hat{U}^2_{rms} T_p Pe_p$, where b was found by fitting a decaying exponential function to the pdfs presented in Figure 4.12, along with additional pdfs computed from simulations with varying Re, Pe_p, and Re_p. Each simulation is represented by one data point with the same marker type used in Figures 4.10 and 4.11 (with simulation details in Table 4.1), where the errors on b are not shown since they are much smaller than the marker size. The data points appear to follow the blue line given by $(\hat{U}^2_{rms} T_p Pe_p)^{-1/2}$, consistent with results from Nasab & Garaud (2020). This demonstrates that $\hat{r}_{rms} \sim 1/b$, a result that is not entirely surprising since it would actually be exact if the pdfs were purely exponential.

4.5 Summary, Applications, and Discussion

4.5.1 Summary

In Nasab & Garaud (2020) we studied preferential concentration in a two-way coupled particle-laden flow in the context of the particle-driven convective insta-

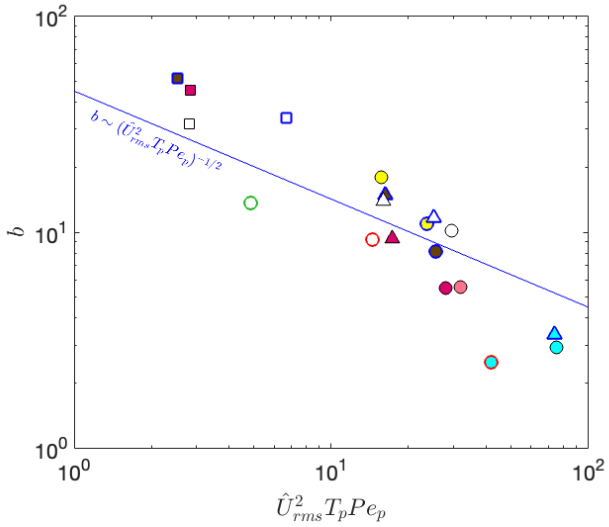

Figure 4.13: The slope b of the exponential tail of the pdf of $\hat{r}$ as a function of $\hat{U}^2_{rms}T_pPe_p$ for simulations at various T_p, r_0, Re, Re_p, and Pe_p (where $Re_p = Pe_p$). The blue solid line shows $b \sim (\hat{U}^2_{rms}T_pPe_p)^{-1/2}$. See Table 4.1 for more details.

bility. We found that the maximum particle concentration enhancement above the mean scales as $u^2_{rms}\tau_p/\kappa_p$, where u_{rms} is the rms fluid velocity, τ_p is the particle stopping time, and κ_p is the assumed particle diffusivity. Additionally, we found that the typical particle concentration enhancement over the mean scales as $(u^2_{rms}\tau_p/\kappa_p)^{1/2}$ and the pdf of the particle concentration over the mean has an exponential tail whose slope scales like $(u^2_{rms}\tau_p/\kappa_p)^{-1/2}$. However, it was not clear that these results would remain valid in a system in which the turbulence is not driven by the particles themselves. In this work, we confirm that the results of Nasab & Garaud (2020) apply in a system in which the turbulence is mechanically-driven. With this extension to a much wider class of turbulent systems, our model has important consequences for preferential concentration in the various applications introduced in Section 4.1. In the next sections, we discuss the potential caveats one should bear in mind before applying the model to real physical systems, and present a particular prediction of the model for droplet concentration in clouds.

4.5.2 Caveats of the model, and extension to higher Re

In general, realistic applications of preferential concentration in natural systems take place in environments such as clouds, river outflows, or accretion disks, that are highly turbulent in nature, and whose Reynolds numbers are asymptotically large. Because of this, the velocity spectra have an inertial range which spans many orders of magnitudes in lengthscales. For sufficiently turbulent flows satisfying Kolmogorov's scaling laws, the eddy turnover timescale is proportional to the eddy lengthscale to the power of 2/3, so one may expect the Stokes number to increase with wavenumber and reach a maximum at the end of the inertial range (i.e. near the Taylor microscale). This is at least qualitatively validated by our finding that the power spectrum of the particle density fluctuations peaks near the Taylor microscale (see Figure 4.6). This poses two problems in terms of the extension of our results to very strongly turbulent flows.

On the one hand, it is possible for the Stokes number at the Taylor microscale St_λ to exceed the threshold of validity of the two-fluid approximation (even if St is small at the injection scale). This is not a problem for the DNS presented here, where $St_\lambda = T_p \hat{\lambda}^{-2/3} \lesssim 0.06$ for all simulations listed[1] in Table 4.1. However, real-life turbulent flows that have a very large inertial range ($Re \gg 1$) are more likely satisfy $St_\lambda > 0.3$, in which case the two-fluid approximation breaks down and the scalings discussed here do not apply.

We also note that our theory is predicated upon the assumption that a single (possibly scale-dependent) Stokes number adequately summarizes the particle dynamics for the entire simulation. In practice, of course, this is not the case, and individual particles traveling through the turbulent flow experience a wide range of Stokes numbers depending on the local conditions within the eddy they

[1] With the Taylor microscales computed in Section 4.3.2, we find that St_λ is roughly $2T_p$ for $Re = 100$, $3T_p$ for $Re = 300$, and $4T_p$ for $Re = 600$

are currently interacting with. As a result, the two-fluid approximation can *locally* break down even if it holds on average. Since one of the main results of our analysis is concerned with extreme events (i.e. the prediction of the maximum particle density, and the existence of an exponential tail within the particle density pdf), one cannot rule out the possibility that these events coincidentally occur in the rare conditions for which the two-fluid approximation would break down. This can only be checked by performing Lagrangian simulations with a very large number of particles (so the tail of the distribution can be probed), and computing the instantaneous Stokes number of each particle while they are located in dense regions, which is beyond the scope of this study.

On the other hand, one also needs to question whether results obtained in DNS at moderate Reynolds numbers remain valid when $Re \to \infty$. Indeed, due to the high computational cost of running 3D DNS, we only looked at moderately turbulent systems where $Re \lesssim 600$. In that case, the inertial range of the velocity spectra is quite limited (see Section 4.3). As a result, the characteristic fluid velocity measured at the injection scale is comparable to the corresponding fluid velocity measured at the Taylor microscale. However when $Re \to \infty$, the velocities at these two scales may be vastly different. This naturally brings up a valid question concerning the predictive model: is the maximum particle concentration enhancement dependent on the fluid velocity measured at the injection scale (as we assumed in this work), or near the Taylor microscale which seems to set the dominant scale of the particle concentration fluctuations? A further look into the data may provide some preliminary clue to the answer (although simulations at much higher Re will ultimately be needed to fully confirm the results).

We saw in Section 4.4 that our predictive model for maximum particle concentration enhancement in the two-fluid approximation depends on the fluid velocity,

the particle stopping time, and the assumed particle diffusivity, as

$$\left(\frac{\rho_p'}{\bar{\rho}_p}\right)_{max} \approx \alpha \frac{u^2(\ell)\tau_p}{\kappa_p} \tag{4.28}$$

for some prefactor α, where here we allow for the possibility that the correct value of u may be different from u_{rms}. We now consider the hypothesis raised above that the fluid velocity may need to be that of the Taylor microscale instead, such that $\ell = \lambda$. Assuming a Kolmogorov scaling, it then follows that

$$u(\lambda) = u_{rms}(\lambda k_s)^{1/3}, \tag{4.29}$$

where we recall that $2\pi/k_s = L_z$ is the height of the computational domain.

Using the fact that $\lambda k_s = \hat{\lambda} \propto Re^{-1/2}$ we obtain

$$u(\lambda) \propto u_{rms} Re^{-1/6}. \tag{4.30}$$

Substituting $u(\lambda)$ in (4.28), the maximum particle concentration enhancement in this alternative model would be

$$\left(\frac{\rho_p'}{\bar{\rho}_p}\right)_{max} \sim Re^{-1/3} \frac{u_{rms}^2 \tau_p}{\kappa_p}. \tag{4.31}$$

This formula suggests that $(\rho_p'/\bar{\rho}_p)_{max}$ should decrease with increasing Re. If this were the case, then we would expect that $(\rho_p'/\bar{\rho}_p)_{max}$ should be approximately twice as large for $Re = 100$ in comparison to $Re = 600$ (with the remaining parameters fixed to be the same). This is contrary to the observations from our simulations, in which we see the opposite trend (see, e.g. Figure 4.9(c)). We therefore conclude that our original model, in which $(\rho_p'/\bar{\rho}_p)_{max} \sim u_{rms}^2 \tau_p/\kappa_p$, is closer to the correct answer. However, since it does not predict *any* direct

dependence of $(\rho_p'/\bar{\rho}_p)_{max}$ on Re, while the data suggests that there may be some, we also acknowledge that it cannot be the complete answer. Simulations at much higher Reynolds number will be needed to clarify the situation.

4.5.3 Application to natural systems

While the question of the applicability of our model to very large Reynolds number systems was partially addressed in the previous section, a second, much more difficult question arises concerning the applicability and validity of the two-fluid equations themselves. In particular, the central result of this work is the role of particle diffusion (κ_p) in controlling the maximum and typical (rms) particle concentration enhancement (see Sec. 4.4.1-4.4.2), so one may rightfully question whether the diffusion approximation used in Eqs. (4.1)–(4.4) is valid in the first place. A complete answer to this question is largely beyond the scope of this paper, and will require either delicate laboratory experiments, or DNS of a large number of fully-resolved particles interacting with a turbulent fluid.

In the limit where the particles are very small, however, stochastic collisions with the fluid molecules are a source of dispersion in the particle transport equation (usually referred to as Brownian motion), that can be modeled as a diffusion process and whose coefficient is given by

$$\kappa_p \approx \frac{k_B T_m}{6\pi s_p \rho_f \nu}, \tag{4.32}$$

where $k_B = 1.38 \times 10^{-23}$ J $\cdot$ K^{-1} is the Boltzmann constant, T_m is the mean temperature of the fluid, and s_p is the particle radius. This expression can be considered as a lower limit on the effective particle diffusivity, and using it in conjunction with Eq. (4.25) and (4.27), provides an upper limit on the maximum particle concentration $(\rho_p'/\bar{\rho}_p)_{max}$ and the rms particle concentration enhancement

$(\rho_p'/\bar{\rho}_p)_{rms}$.

To see what kind of prediction for particle concentration this lower-limit estimate for κ_p leads to, it is helpful to consider a specific application, such as that of rain formation in warm clouds (e.g. cumulus or stratocumulus clouds). In this application, turbulence is generally mechanically-driven, generated by vertical drafts and wind shear. It has been largely hypothesized that the broadening of the droplet spectrum during the initial stage of droplet growth is due to preferential concentration followed by enhanced collision rates and coalescence Shaw (2003). With this in mind, we consider small droplets of radius $s_p = 10$ μm and density $\rho_s = 1000$ kg/m^3 with the typical values for the properties of ambient air being $\rho_f = 1$ kg/m^3, $\nu \approx 10^{-5}$ m^2/s, and a mean temperature of $T_m \approx 300$ K.

Based on these estimates, the stopping time for a cloud droplet is given by

$$\tau_p = \frac{2\rho_s s_p^2}{9\rho_f \nu} \approx (2 \times 10^{-3} \text{ s})\left(\frac{s_p}{10 \ \mu\text{m}}\right)^2, \tag{4.33}$$

and the particle diffusivity due to Brownian motion is given by

$$\kappa_p = (2 \times 10^{-12} \text{ m}^2/\text{s})\left(\frac{10 \ \mu\text{m}}{s_p}\right)\left(\frac{T_m}{300 \text{ K}}\right). \tag{4.34}$$

Using this, we can then obtain an upper limit estimate of the maximum and rms particle concentration enhancements as

$$\left(\frac{\rho_p'}{\bar{\rho}_p}\right)_{max} \lesssim \alpha \frac{u_{rms}^2 \tau_p}{\kappa_p} \approx 10^8 \left(\frac{u_{rms}}{1 \text{ m/s}}\right)^2 \left(\frac{s_p}{10 \ \mu\text{m}}\right)^2 \left(\frac{2 \times 10^{-12} \text{ m}^2/\text{s}}{\kappa_p}\right) \tag{4.35}$$

$$\left(\frac{\rho_p'}{\bar{\rho}_p}\right)_{rms} \lesssim \gamma u_{rms} \sqrt{\frac{\tau_p}{\kappa_p}} \approx 2 \times 10^3 \left(\frac{u_{rms}}{1 \text{ m/s}}\right)\left(\frac{s_p}{10 \ \mu\text{m}}\right)\left(\frac{2 \times 10^{-12} \text{ m}^2/\text{s}}{\kappa_p}\right)^{1/2} \tag{4.36}$$

where we have used $\alpha \approx 0.1$ and $\gamma \approx 0.07$ extracted from our simulations (see

Figures 4.10 and 4.11), and a fiducial value of $u_{rms} = 1$ m/s was assumed. This result is quite remarkable, given that the characteristic Stokes number St associated with these droplets is very small. Indeed, assuming that the eddy turnover time is $\tau_e \sim L/u_{rms}$ where $L \sim 1$ km is a typical cloud height, we find that

$$St \simeq \frac{\tau_p}{\tau_e} \approx (2 \times 10^{-6}) \left(\frac{s_p}{10\ \mu\text{m}} \right)^2 \left(\frac{1\ \text{km}}{L} \right) \left(\frac{u_{rms}}{1\ \text{m/s}} \right). \tag{4.37}$$

This suggests that strong preferential concentration is possible even when $St \ll 1$ (a surprising result that is supported by the DNS presented in Section 4.3).

Of course, as discussed above, this provides only an upper limit estimate of the particle concentration enhancement, which is only valid as long as κ_p is dominated by the effects of Brownian motion. To check whether this is likely true in the cloud application considered, we compute the corresponding volume fraction occupied by the particles in regions of maximal concentration. We find that if the mean liquid water content of the cloud is $\bar{\rho}_p \approx 1$ mg/m^3, then the average volume fraction occupied by the droplets is $\bar{\Phi} = (\bar{\rho}_p/\rho_s) \approx 10^{-9}$. Thus, the associated maximum and typical volume fraction achievable though preferential concentration are

$$\Phi_{max} \approx \bar{\Phi}(\rho_p'/\bar{\rho}_p)_{max} \approx O(0.1), \tag{4.38}$$

$$\Phi_{rms} \approx \bar{\Phi}(\rho_p'/\bar{\rho}_p)_{rms} \approx O(10^{-6}). \tag{4.39}$$

With the possibility of very large volume fractions emerging out of the preferential concentration process, we must therefore account for the possibility that particles may interact hydrodynamically through their wakes, which would increase κ_p (and therefore lower $(\rho_p'/\bar{\rho}_p)_{max}$ and Φ_{max}, and possibly also $(\rho_p'/\bar{\rho}_p)_{rms}$ and Φ_{rms}). For simplicity, we use the results of Segre et al. (2001) to construct an effective diffusion coefficient associated with hydrodynamic interactions. They

suggest that that the mutually-induced dispersion can be modeled by

$$\kappa_p \approx \beta(\Phi) s_p V_p, \tag{4.40}$$

where β is a function of the volume fraction Φ occupied by the particles and V_p is the velocity of the particles relative to the fluid. Segre et al. (2001) found that $\beta(\Phi) \lesssim 0.1$ for volume fractions of up to $\Phi \approx 0.2$. Thus we can construct an approximate upper limit for κ_p by setting $\beta = 0.1$.

The relative velocity of the particles with respect to the fluid is obtained following Maxey (1987) (and the arguments presented in Eq. 4.15) to be

$$V_p = |\mathbf{u}_p - \mathbf{u}| \approx \tau_p \left| \frac{\partial \mathbf{u}}{\partial t} + \mathbf{u} \cdot \nabla \mathbf{u} \right| + O(\tau_p^2). \tag{4.41}$$

We can estimate it roughly using dimensional arguments as

$$V_p(\ell) \approx \tau_p \frac{u^2(\ell)}{\ell} \approx \tau_p \frac{u_{rms}^2}{L} \left(\frac{\ell}{L} \right)^{-1/3}, \tag{4.42}$$

assuming a Kolmogorov scaling for the eddy velocity $u(\ell)$ at scale ℓ. We therefore see that V_p will be largest at the Taylor microscale, and set $\ell = \lambda \approx \sqrt{15} Re^{-1/2} L$ to obtain an upper limit for V_p:

$$V_p \lesssim \tau_p \frac{u_{rms}^2}{L} (15)^{-1/6} Re^{1/6}. \tag{4.43}$$

Using (4.43) in (4.40) we can now obtain an upper limit on κ_p, as

$$\kappa_p \lesssim \beta s_p V_p \approx (3 \times 10^{-11} \text{ m}^2/\text{s}) \left(\frac{s_p}{10 \ \mu\text{m}} \right)^3 \left(\frac{u_{rms}}{1 \text{ m/s}} \right)^{13/6} \left(\frac{1 \text{ km}}{L} \right)^{5/6}, \tag{4.44}$$

which is only about one order of magnitude larger than the value for κ_p obtained

by considering the contribution due to Brownian motion only (for Eq. 4.35).

We apply this formulation for κ_p in (4.28) and find that

$$\left(\frac{\rho_p'}{\bar{\rho}_p}\right)_{max} \lesssim \alpha \frac{u_{rms}^2 \tau_p}{\kappa_p} \approx 10^7 \left(\frac{u_{rms}}{1 \text{ m/s}}\right)^2 \left(\frac{s_p}{10\ \mu\text{m}}\right)^2 \left(\frac{3 \times 10^{-11}\ \text{m}^2/\text{s}}{\kappa_p}\right), \tag{4.45}$$

$$\left(\frac{\rho_p'}{\bar{\rho}_p}\right)_{rms} \lesssim \gamma u_{rms} \sqrt{\frac{\tau_p}{\kappa_p}} \approx 600 \left(\frac{u_{rms}}{1 \text{ m/s}}\right) \left(\frac{s_p}{10\ \mu\text{m}}\right) \left(\frac{3 \times 10^{-11}\ \text{m}^2/\text{s}}{\kappa_p}\right)^{1/2}, \tag{4.46}$$

with a corresponding maximal and rms volume fraction

$$\Phi_{max} \approx \bar{\Phi}(\rho_p'/\bar{\rho}_p)_{max} \approx O(0.01), \tag{4.47}$$

$$\Phi_{rms} \approx \bar{\Phi}(\rho_p'/\bar{\rho}_p)_{rms} \approx O(10^{-6}). \tag{4.48}$$

Note that since these were obtained using upper limits on κ_p, they can be viewed as lower limits on Φ_{max} and Φ_{rms}.

Overall, this shows that both lower and upper limit estimates for the particle diffusivity κ_p yield relatively consistent results in the context of cloud applications, and more importantly, that cloud turbulence could produce very large localized enhancements of the droplet concentration, despite the fact that the Stokes number is very low. Applications of this work to dust growth in protoplanetary disks were discussed by Garaud & Nasab (2019), with very similar conclusions.

Of course, our results also show that these extreme events where Φ approaches Φ_{max} are rare, belonging to the tail of an exponential distribution. However, it is also well known in the context of both rain formation (Devenish et al., 2012; Grabowski & Wang, 2013) and planet formation (Birnstiel et al., 2016; Weidenschilling & Cuzzi, 1993), that producing a few larger particles is all it takes for the process to start. Indeed, these larger "lucky particles" then sediment or drift with respect to the smaller ones, and can continue to grow by sweeping the latter.

As such, particle growth in these contexts is controlled by what happens in the tail of the particle size distribution, which is why the results discussed here are particularly relevant.

Acknowledgements

S. N. is supported by NSF AST-1908338. Simulations were run on a modified version of the PADDI code, originally written by S. Stellmach, on the UCSC Lux cluster and the NERSC Cori supercomputer. The authors thank Eckart Meiburg for his invaluable insight.

Chapter 5

Identification and classification of particle clusters

5.1 Motivation and goals

In Chapters 3 and 4, we found that the maximum and typical particle concentration enhancement in a particle-laden flow can be predicted using scaling laws that depend on certain properties of the system, namely the particle stopping time τ_p, the rms fluid velocity u_{rms}, and the assumed particle diffusivity κ_p. In these studies, we also observed that due to preferential concentration, the particle field develops dense sheet-like structures (as shown in Figure 4.3). However, we have yet to quantitatively investigate the physical characteristics of these dense regions, which may shed light on processes associated with particle growth in relevant applications. For example when studying rain formation, it is important to study the dynamics that may contribute to enhanced collision rate of smaller droplets. At the same time, it may also be worth examining how the typical shape and mass of these dense regions are dependent on the inherent properties of the

system (such as particle size, turbulence, etc.). From there, we may be able to distinguish which of these characteristic features play a role in catalyzing droplet growth. Therefore in this chapter, we focus on identifying characteristic features of the densest particle concentrations, referred to as "clusters" hereafter.

There are several techniques used in the literature to identify clusters and their associated topological features. One method to characterize their shape is that of Minkowski functionals (Minkowski, 1903), which has been primarily used in cosmology to identify features of large-scale galactic structures (Mecke et al., 1993; Schmalzing et al., 1995; Schmalzing & Buchert, 1997). Using methods from integral geometry, Schmalzing & Buchert (1997) developed numerical methods to quantify the morphology of isodensity contours of a scalar field, where they have posited that the morphology of a d-dimensional structure is described by $d + 1$ Minkowski functionals. In 3D for example, the four functionals used are based on the volume, surface, curvature, and Euler number (based on the number of vertices, edges, and faces) for a given structure (or in our case, cluster). Other characteristics can be obtained using these functionals, such as typical dimensions and general shape of the structure analyzed.

Another standard class of techniques for cluster identification is box-counting methods, which we use in this study. The name refers to the fact that the domain is generally divided into boxes of equal size, so that an averaged particle concentration can be computed for a given box. A threshold value is employed in order to identify the denser clusters in the domain. For formalisms which track individual particles (such as the Lagrangian or fully-resolved formalisms), the threshold can be set in terms of the number density of particles per box. On the other hand for two-fluid and Equilibrium formalisms, the threshold can be easily set by some value of the particle concentration already measured in the system.

Once the boxes characterized by relatively denser concentrations are found, we can then determine which of the connected boxes constitute a given cluster. With the clusters identified, we can then extract and compute relevant quantities of interest.

Although there exist studies classifying large-scale structures in astrophysical applications, there are very few studies done in the context of preferential concentration (Aliseda et al., 2002), and none to the author's knowledge in conjunction with the two-fluid formalism. In what follows, we revisit the 3D Direct Numerical Simulations (DNSs) generated from Chapter 4, and develop the tools necessary to identify particle clusters and compute their aforementioned properties.

For completeness, we present the model and he model set-up consisted of a particle-laden flow following the two-fluid formalism in which the turbulence is mechanically-driven by a sinusoidal Kolmogorov flow.associated non-dimensional equations used from Chapter 4 here. T The system is initialized with a uniform distribution of particles (see Section 4.2 for more details). The non-dimensional governing equations are

$$\frac{\partial \hat{\mathbf{u}}}{\partial t} + \hat{\mathbf{u}} \cdot \nabla \hat{\mathbf{u}} = -\nabla \hat{p} + r_0 \hat{r} \frac{\hat{\mathbf{u}}_p - \hat{\mathbf{u}}}{T_p} + \frac{1}{Re} \nabla^2 \hat{\mathbf{u}} + \sin(z) \hat{\mathbf{e}}_x, \tag{5.1}$$

$$\frac{\partial \hat{\mathbf{u}}_p}{\partial t} + \hat{\mathbf{u}}_p \cdot \nabla \hat{\mathbf{u}}_p = \frac{\hat{\mathbf{u}} - \hat{\mathbf{u}}_p}{T_p} + \frac{1}{Re_p} \nabla^2 \hat{\mathbf{u}}_p, \tag{5.2}$$

$$\frac{\partial \hat{r}}{\partial t} + \nabla \cdot (\hat{\mathbf{u}}_p \hat{r}) = \frac{1}{Pe_p} \nabla^2 \hat{r}, \tag{5.3}$$

$$\nabla \cdot \hat{\mathbf{u}} = 0, \tag{5.4}$$

where the hatted quantities represent the non-dimensional state variables. These include the pressure $\hat{p}$, the fluid velocity $\hat{\mathbf{u}}$, the particle $\hat{\mathbf{u}}_p$ velocity, and the rescaled particle concentration $\hat{r} = \rho_p/(\rho_f r_0)$ where the ρ_p is the local particle mass density and ρ_f is the mean fluid density, and at initialization $\hat{r} = 1$ everywhere. The

non-dimensional parameters consist of the non-dimensional stopping time T_p, the mass loading r_0, the fluid Reynolds number Re, the particle Reynolds number Re_p, and the particle Péclet number Pe_p. We analyze the clusters only after the system has reached a statistically steady state. We also use several of previously defined quantities to aid in analyzing the clusters, namely the maximum particle concentration across the domain $\hat{r}_{sup}$ (4.18), the standard deviation around the mean particle density $\hat{r} = 1$ given by $\hat{r}_{rms}$ (4.19), and the rms fluid velocity $\hat{U}_{rms}$ (4.20).

Some of the key questions that we hope to answer are the following: (1) Can we predict cluster characteristics, such as shape and mass, from the parameters of the system? and (2) How do the individual clusters inform the shape of the probability distribution function of the particle concentration? With this in mind, the chapter is organized as follows: In Section 5.2, we introduce the algorithm used to identify clusters as well as the techniques used to extract certain cluster characteristics. In Section 5.3, we present the results of our algorithm when applied to the simulations generated for Chapter 4, and highlight observed trends in the cluster data. We conclude in Section 5.4 with a discussion of the implications from our findings to real-life applications, and work that remains to be done in future investigations.

5.2 Methodology

In this section, we describe the algorithm used to identify characteristic features of individual particle clusters due to preferential concentration, such as mass, size, and shape. The method we developed consists of three stages: (1) identifying and labeling clusters, (2) computing relevant quantities from each cluster, and (3) filtering and extracting the data pertinent to our study. We also provide several tests which we ran to verify the accuracy of our algorithm.

5.2.1 Algorithm

Identification of clusters

The algorithm that we use follows the connected-component labeling (CCL) method, which was shown to be effective for "blob" classification and extraction for image analysis (Shapiro, 1992). In order to distinguish denser particle regions from regions of lower particle concentration, we select a threshold value $\hat{r}_{crit}$ in which to analyze only the clusters for which $\hat{r} \geq \hat{r}_{crit}$. We create a `binary_mask` array to determine where the clusters are located, where the dimensions of the array correspond to the size of the computational domain. We construct the array in a way that the elements that are labeled with ones correspond to the grid points for which $\hat{r} \geq \hat{r}_{crit}$, whereas the remaining elements for which $\hat{r} < \hat{r}_{crit}$ are labeled with zeros. We refer to the elements labeled with ones as *foreground* elements, and we refer to the elements labeled with zeros as *background* elements. For our study, we design the `binary_mask` array with $N_x \times N_y \times N_z$ elements so that the indexed position (i, j, k) corresponds to a grid point at the same indexed position in physical space.

At this point, we define several other terms that will help us when describing the labeling procedure. In 2D, two elements are *neighbors* if they touch one another on their corners or edges, so that each element has 8 neighbors. In 3D, two elements are *neighbors* if they touch one another on their faces, edges, or corners. As such in 3D, each element is surrounded by 26 neighbors. A *cluster* is composed of all of the foreground elements that are connected, and is given a unique identification number which we refer to here as a *label*.

We next describe the labeling procedure that consists of a two-pass algorithm. The first pass assigns temporary labels to the foreground elements, and the second pass merges any connected clusters and reassigns the same label to the resulting

merged cluster. We store the labels in the `label_mask` array, which is initialized with zeros (and has the same dimensions of the computational domain, i.e. $N_x \times N_y \times N_z$).

The first pass algorithm is carried out by iterating over each element of the domain in row-major order, beginning at $(i, j, k) = (0, 0, 0)$ and ending at $(i, j, k) = (N_x, N_y, N_z)$. The procedure is outlined below:

1. If the element is a background element, continue to the next element and repeat step (1). If the element is a foreground element, continue to step (2).
2. Obtain the neighboring labels of the current element from the `label_mask` array. If all of the neighboring labels are zeros, then assign and store a unique label to the current element in the `label_mask` array. Continue to the next element, and start over at step (1). Otherwise if at least one the neighboring labels is non-zero, continue to step (3).
3. Find the neighbor with the smallest label. Assign and store this label to the current element in the `label_mask` array. Continue to the next element and start over at step (1).

It is worth noting that the algorithm takes into account the periodic boundary conditions. Thus for elements that lie on the boundaries, all neighboring labels (8 labels for the 2D case, 26 labels for the 3D case) can be successfully obtained.

In Figure 5.1, we show how the first pass labeling procedure uses the `binary_mask` array (a) to find the labels of the connected clusters stored in the `label_mask` array (b). For ease of understanding, we present 2D arrays and do not incorporate periodic boundary conditions in this example. As illustrated in Figure 5.1(b), there are cases after the first labeling pass where two connected regions (that should ultimately be labeled as one cluster) have different labels.

We fix this issue with the second labeling pass with what is often called in the

Figure 5.1: Identification of clusters. Each square in either figure corresponds to one grid point in a hypothetical 2D 9×10 simulation. (a) *Binary mask*: Foreground elements are labeled, while background elements are unlabeled. (b) *First pass labeling*: When an element is surrounded by neighboring elements with different labels (boxed in yellow), the element is labeled with the lowest numbered label.

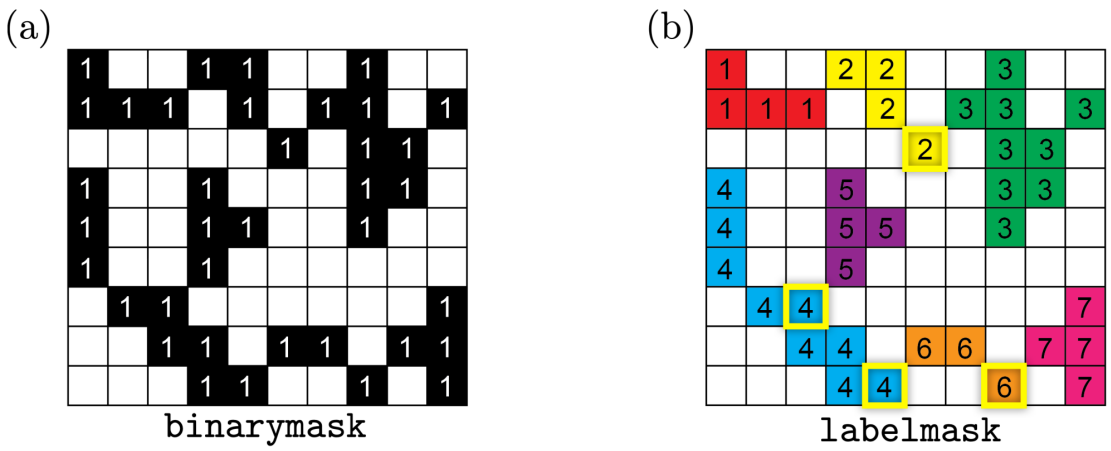

computer vision community as a union-find data structure (or a merge-find data structure) (Shapiro, 1992). We keep track of how the different labels are connected using the `parent` array. We illustrate how the `parent` array is constructed in Figure 5.2, where we use the `label_mask` found in Figure 5.1(b). In Figure 5.2 we present a tree diagram on the left, where each node of the tree represents a label and points upwards to another node, otherwise referred to as its parent node. As shown, there are two disjoint trees (representing the two unconnected clusters) that are given by the set of labels $\{1, 2, 3\}$ and $\{4, 5, 6, 7\}$. For example, we see that the parent node of 7 is 5, and the parent node of 5 is 4. We also see that the root parent nodes are 1 and 4. We store this hierarchy of labels in the `parent` array whose index represents a label, and whose values are the labels of the parent nodes. A parent value that is equal to 0 represent the node of the root of the tree.

The second labeling pass (or the merging procedure) is then carried out by

Figure 5.2: Example of a tree diagram and the corresponding `parent` array.

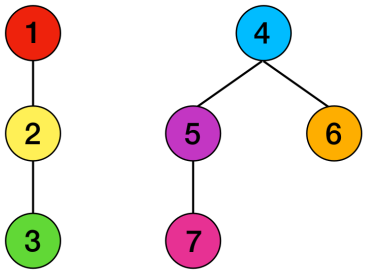

`parent`

index	1	2	3	4	5	6	7
value	0	1	2	0	4	4	5

collapsing the tree structure to its root parent nodes, by reassigning the non-root node labels with its respective root parent node label. We include the updated `parent` array and `label_mask` in Figure 5.3. We clearly see that after the second labeling pass, the two disjoint clusters are now correctly labeled.

Extracting cluster information

We then extract relevant quantities of interest from each individual cluster. To do so, we define a number of diagnostic quantities. The maximum density within the ith cluster, which occurs at the position $\mathbf{x} = \mathbf{x}_{sup,i}(t)$ at time t, is defined as

$$\varrho_{sup,i}(t) = \hat{r}(\mathbf{x}_{sup,i}, t) = \max_{\chi_i} \hat{r}(t), \tag{5.5}$$

where χ_i is the set of all elements of the ith cluster. The total particle mass is computed by summing up the mass of each element in χ_i written as

$$M_i(t) = \sum_{\chi_i} \hat{r}(t)\, \Delta x \Delta y \Delta z, \tag{5.6}$$

where Δ_x is the distance between two mesh points in the x direction, and similarly for Δ_y and Δ_z.

We are also interested in quantifying the shape of the clusters, in the vicinity

Figure 5.3: Merging of clusters. (a) After first pass labeling. (b) After second pass labeling (merging).

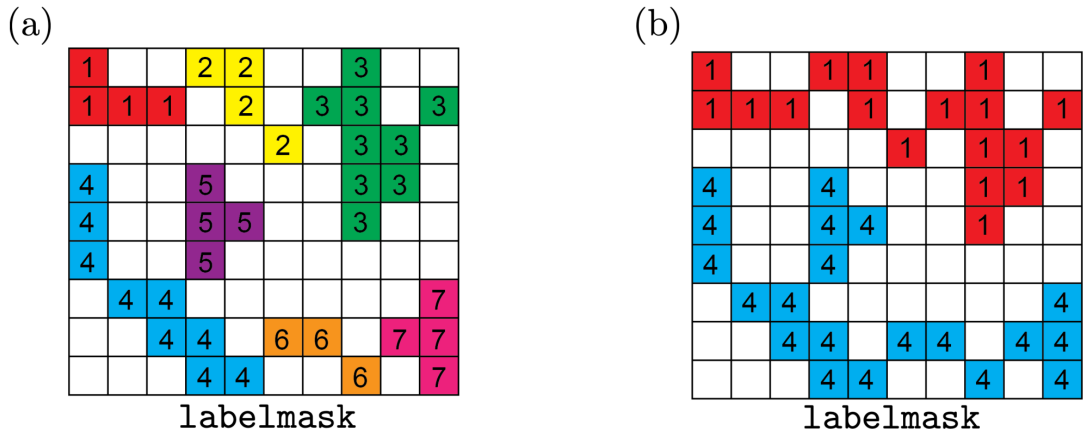

parent

index	1	2	3	4	5	6	7
value	0	1	1	0	4	4	4

of $\mathbf{x}_{sup,i}$. Therefore, another quantity of interest is the thickness of each cluster which is defined as the smallest dimension of the cluster around $\mathbf{x}_{sup,i}$. Compared to the previous diagnostic quantities, the thickness for each cluster is not as straightforward to compute and requires several steps. The first step is to determine the cluster dimensions along the principal axes around $\mathbf{x}_{sup,i}$. We can estimate the particle concentration $\hat{r}(\mathbf{x})$ near $\mathbf{x}_{sup,i}$ by carrying out a second-order Taylor expansion given by

$$\hat{r}(\mathbf{x}) \approx \frac{1}{2} (\mathbf{x} - \mathbf{x}_{sup,i})^T \mathbf{H}(\mathbf{x}_{sup,i}) (\mathbf{x} - \mathbf{x}_{sup,i}), \tag{5.7}$$

where the Hessian matrix $\mathbf{H}$ using (5.7) is

$$\mathbf{H} = \begin{cases} \begin{pmatrix} r_{xx} & r_{xy} \\ r_{xy} & r_{yy} \end{pmatrix} & \text{(2D case)}, \\ \\ \begin{pmatrix} r_{xx} & r_{xy} & r_{xz} \\ r_{xy} & r_{yy} & r_{yz} \\ r_{xz} & r_{yz} & r_{zz}, \end{pmatrix} & \text{(3D case)}, \end{cases}$$

and where we estimate the partial derivatives by using finite difference approximations. We can then find the principal axes about $\mathbf{x}_{sup,i}$ by solving for the eigenvectors of $\mathbf{H}$ (using the `dsyev` LAPACK routine, see Anderson et al., 1999). The respective ratios of the eigenvectors can be used to estimate the shape of the cluster in the vicinity of its densest point.

We can use this information to compute the thickness of a cluster along its thin dimension. To search for the edge of the cluster, we begin by defining a continuous version of the `binary_cluster` array that exists at every point in space, namely the function $A(\mathbf{x})$ constructed using a particle-in-cell (PIC) weighting scheme, illustrated in Figure 5.4 and defined in 2D as

$$\begin{aligned} A(x,z) = \frac{1}{\Delta x \Delta z} \Big[& (x_{hi} - x)(z_{hi} - z)\, \texttt{binary\_cluster}(i_{lo}, k_{lo}) \\ & + (x_{hi} - x)(z - z_{lo})\, \texttt{binary\_cluster}(i_{lo}, k_{hi}) \\ & + (x - x_{lo})(z_{hi} - z)\, \texttt{binary\_cluster}(i_{hi}, k_{lo}) \\ & + (x - x_{lo})(z - z_{lo})\, \texttt{binary\_cluster}(i_{hi}, k_{hi}) \Big], \end{aligned}$$

In this formula, the contribution from each neighboring grid point located at

(x_*, z_*) to the particle is computed as follows:

$$\left(\frac{\Delta x - |x - x_*|}{\Delta x}\right)\left(\frac{\Delta z - |z - z_*|}{\Delta z}\right)\texttt{binary\_cluster}(i_*, k_*),$$

where $\Delta x = x_{hi} - x_{lo}$ and $\Delta z = z_{hi} - z_{lo}$. With this definition, A is exactly equal to the binary mask on grid points, but is continuously interpolated in between grid points. For example, it is easy to see in Figure 5.4 that the contribution to the particle from the grid point at (x_{lo}, z_{hi}) (corresponding to the index (i_{lo}, k_{hi}) in the `binary_cluster` array) is the smallest, whereas the contribution from the grid point at (x_{hi}, z_{lo}) is the largest.

The extension to this algorithm in 3D is trivial, and accounts for the eight neighboring grid points, where the contribution from each neighboring point (x_*, y_*, z_*) is

$$\left(\frac{\Delta x - |x - x_*|}{\Delta x}\right)\left(\frac{\Delta y - |y - y_*|}{\Delta y}\right)\left(\frac{\Delta z - |z - z_*|}{\Delta z}\right)\texttt{binary\_cluster}(i_*, j_*, z_*),$$

where $\Delta y = y_{hi} - y_{lo}$.

It is also worth mentioning that the PIC weighting scheme incorporates several special cases with respect to the relative position of the particle to neighboring particles. For example, if a particle is precisely located on the edge between two grid points, only the contributions from the two neighboring points are incorporated into the value for A. If a point lies on the plane of four neighboring points in 3D, only the contributions from those four points are incorporated (instead of all eight).

Once $A(\mathbf{x})$ is determined, in order to find the boundary point of a cluster, we start at $\mathbf{x}_{sup,i}$ and go along the direction of the eigenvector with the smallest eigenvalue, searching for the location where $A(\mathbf{x})$ drops below 1/2. Note that in

Figure 5.4: Particle-in-cell weighting scheme. We determine the weight of the particle at (x, z) by taking into account the values of the neighboring points found in the `binary_cluster` array.

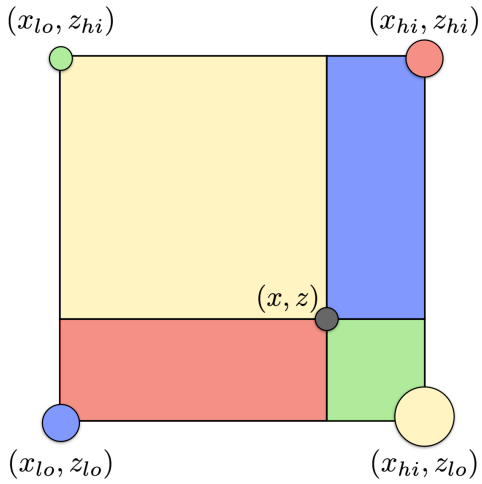

practice, $A(\mathbf{x})$ is not monotonic, and as a result, we use a two-step method in order to find the boundary point. The first is a linear stepping scheme in which we gradually increase the distance from $\mathbf{x}_{sup,i}$ until $A(\mathbf{x}) < 0.2$, as illustrated in Figure 5.5(a). Then we use an interval halving scheme to more precisely pinpoint the boundary point, corresponding to the location where $0.45 < A(\mathbf{x}) < 0.5$, as shown by Figure 5.5(b).

Filtering

As a consequence of choosing a relatively large threshold value for $\hat{r}_{crit}$, a significant number of very small clusters are identified (i.e. clusters consisting of a very small number of foreground elements). In order to eliminate these smaller clusters from the final data set (and thus the subsequent analyses), we apply a filter so that the extracted clusters are of the size $N_i \geq 27$ for 3D clusters, and $N_i \geq 9$ for 2D clusters.

Figure 5.5: (a) Linear stepping method to find a point that is sufficiently far from the cluster corresponding to the region $A(\mathbf{x}) < 0.2$ colored in light blue. (b) Interval halving method to find the boundary point of the cluster corresponding to the region $0.45 < A(\mathbf{x}) < 0.5$ colored in light red.

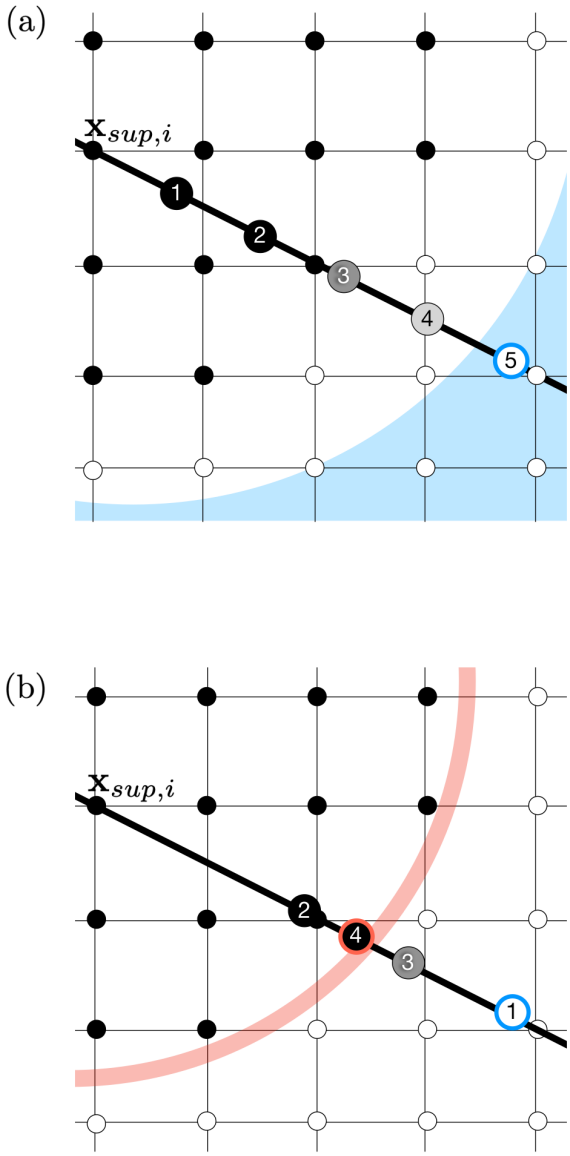

5.2.2 Selection of $\hat{r}_{crit}$

We explored various choices of threshold values $\hat{r}_{crit}$ on our simulations, where the primary objective here was to isolate a sufficient number of relatively dense clusters, to gain some confidence in the statistics of their measured properties. In real-life applications such as clouds for instance, the rationale for choosing $\hat{r}_{crit}$ may be more physical in nature. For instance, one may be interested in detecting only the highest density regions for which collisions of smaller droplets are likely to occur, eventually leading to rain formation.

Recall that for systems in which preferential concentration takes place, an exponential tail appears for values of $\hat{r}$ ranging from $1 + \hat{r}_{rms}$ to $\hat{r}_{sup}$ (see Figure 4.12). Therefore we would expect that regions for which rain formation occur would coincide with values of $\hat{r}$ specifically within this exponential tail.

That being said, we found that applying a fixed threshold for each simulation, e.g. $\hat{r}_{crit} = 2$ or $\hat{r}_{crit} = 1.2$, is not useful. This is because the maximum particle concentration varies dramatically between simulations with low Stokes number (where $\hat{r}_{sup}$ remains close to 1) and simulations with large Stokes number (where $\hat{r}_{sup}$ can be much larger than one). We therefore need to select $\hat{r}_{crit}$ to guarantee that $1 < \hat{r}_{crit} < \hat{r}_{sup}$, while providing a meaningful number of clusters across all simulations.

With that in mind, we systematically explored values of the form $\hat{r}_{crit} = 1 + \sigma\,\hat{r}_{rms}$, where σ is the number of standard deviations above the mean particle concentration $\hat{r} = 1$. When $\hat{r}_{crit}$ is too small, it is difficult to distinguish highly concentrated regions from lower density regions that also fall within the threshold. On the other hand when $\hat{r}_{crit}$ is too large, only a handful of clusters are detected, which is neither realistic nor statistically useful.

Unless otherwise mentioned for the simulations presented here, we set $\hat{r}_{crit} =$

$1 + 2\,\hat{r}_{rms}$ which we found to be optimal in identifying a substantial number of clusters, without ever exceeding $\hat{r}_{sup}$. Note that in real applications, however, $\hat{r}_{sup}$ is much greater than $\hat{r}_{crit}$, and the threshold density of interest (e.g. for rain formation) may have the form $1 + \sigma\,\hat{r}_{rms}$ with $\sigma \gg 1$ instead.

5.2.3 Testing

We verify the accuracy of our algorithm by generating several test cases consisting of clusters of varying size and orientation. For the purpose of clarity, we refer to any values obtained from our algorithm as "extracted" values, and known parameters or values originally set in our test simulations as "actual" values.

First we present 2D test cases, shown in Figure 5.6(a), where several clusters were artificially created. The particle concentration fields of clusters no. $1, 2, 5$ and 6 take the form of a Gaussian profile given by

$$\hat{r}(x, z) \sim \exp\left[-\frac{(x - x_0)^2}{2\sigma_1^2} - \frac{(z - z_0)^2}{2\sigma_2^2} \right], \tag{5.8}$$

where the densest region is by construction located at $\mathbf{x}_{sup,i} = (x_0, z_0)$ and the semi-major axes are given by σ_1 and σ_2, respectively.

To look at cases where the semi-major axes are not aligned with the $x-$ and $z-$ axes of the simulation, we model the particle concentration of clusters no. 3 and 4 with

$$\hat{r}(x', z') \sim \exp\left[-\frac{(x' - x_0')^2}{2\sigma_1^2} - \frac{(z' - z_0')^2}{2\sigma_2^2} \right], \tag{5.9}$$

where we rotate the points (x, z) counterclockwise through the angle θ with respect

to the x-axis about the origin with the following transformation

$$x' = x\cos\theta - y\sin\theta,$$
$$y' = x\sin\theta + y\cos\theta.$$

In Figure 5.6(a), highly concentrated regions are shown in red, and areas with little to no particles are shown in blue. We select $\hat{r}_{crit}$ to be $1 + 2\hat{r}_{rms}$ for each cluster, and outline in yellow where $\hat{r} = \hat{r}_{crit}$. We mark the extracted boundary points in red, and see that they lie on the edges of the cluster (where $\hat{r} = \hat{r}_{crit}$) fairly well. In this test case, we include one cluster (i.e. cluster no. 1) that intersects the periodic boundaries to ensure that the algorithm correctly identifies this as one cluster instead of two or more separate clusters.

We compare several actual characteristic quantities of each cluster, such as the center, the aspect ratio, and the dimensions of the cluster to the extracted quantities as measured from the algorithm in Table 5.1. The actual center is easily obtained by $\mathbf{x}_{sup,i} = (x_0, z_0)$ from the equation used to generate each cluster (5.8), and compares well with the extracted data. The semi-major axes are given by $\vec{\sigma} = (\sigma_1, \sigma_2)$. To compare the geometry of the clusters, we look at the normalized vector $\vec{\sigma}/|\vec{\sigma}|$ for the actual cluster and the normalized vector $\vec{\lambda}/|\vec{\lambda}|$, consisting of the eigenvalues $\vec{\lambda} = (\lambda_1, \lambda_2)$ for the extracted cluster. The actual dimensions of the cluster are found by solving for the distance between the two boundary points that lie on $\hat{r} = \hat{r}_{crit}$ for each of the principal axes. Corresponding cluster diagnostics extracted from the data are found using the searching scheme previously described. We include errors for each set of quantities in Table 5.1(a), and see that our algorithm performs well within an acceptable margin of error.

In Figure 5.6(b), we present a single cluster whose center is located at the bottom left-hand corner. As a result, the cluster appears on all four quadrants of

Table 5.1: Comparison of actual and extracted values of the 2D test cases in Figure 5.6.

	Center (x_0, z_0)			Normalized set of eigenvalues			Dimensions		
No.	Actual	Extracted	L_2 Error	Actual $(\sigma_1, \sigma_2)/\lvert\sigma\rvert$	Extracted $(\lambda_1, \lambda_2)/\lvert\lambda\rvert$	L_2 Error	Actual	Extracted	L_2 Error
1	$(4\pi, 2)$	$(12.55, 2.00)$	0.0164	$(0.7071, 0.7071)$	$(0.7073, 0.7069)$	0.0003	$(0.892, 0.892)$	$(0.901, 0.901)$	0.013
2	$(2\pi, \pi)$	$(6.28, 3.14)$	0.0036	$(0.7071, 0.7071)$	$(0.7072, 0.7070)$	0.0002	$(0.892, 0.892)$	$(0.901, 0.901)$	0.013
3	(π, π)	$(3.14, 3.14)$	0.0023	$(0.9285, 0.3714)$	$(0.9866, 0.1634)$	0.2159	$(0.357, 0.892)$	$(0.358, 0.894)$	0.003
4	$(3\pi, \pi)$	$(9.42, 3.14)$	0.0050	$(0.9285, 0.3714)$	$(0.9866, 0.1634)$	0.2159	$(0.357, 0.892)$	$(0.358, 0.894)$	0.002
5	$(2\pi, 5)$	$(6.28, 5.01)$	0.0105	$(0.9806, 0.1961)$	$(0.9992, 0.0407)$	0.1565	$(0.361, 1.784)$	$(0.357, 1.784)$	0.004
6	$(0, 0)$	$(0.00, 0.00)$	0.0000	$(0.7071, 0.7071)$	$(0.7179, 0.6962)$	0.0154	$(0.484, 0.484)$	$(0.483, 0.483)$	0.002

Table 5.2: Comparison of actual and extracted values of the 2D test cases in Figure 5.7.

	Center (x_0, y_0, z_0)			Normalized set of eigenvalues		
No.	Actual	Extracted	L_2 Error	Actual $(\sigma_1, \sigma_2, \sigma_3)/\lvert\sigma\rvert$	Extracted $(\lambda_1, \lambda_2, \lambda_3)/\lvert\lambda\rvert$	L_2 Error
7	$(\pi/4, \pi/4, \pi/4)$	$(0.785, 0.785, 0.785)$	0.001	$(0.5774, 0.5774, 0.5774)$	$(0.5774, 0.5774, 0.5774)$	0.000
8	$(0, \pi/4, \pi/4)$	$(0.000, 0.785, 0.785)$	0.001	$(0.5774, 0.5774, 0.5774)$	$(0.5774, 0.5774, 0.5774)$	0.000

	Dimensions		
No.	Actual	Extracted	L_2 Error
7	$(0.155, 0.155, 0.155)$	$(0.156, 0.156, 0.156)$	0.002
8	$(0.308, 0.308, 0.308)$	$(0.303, 0.303, 0.303)$	0.008

the snapshot. In Table 5.1, we verify that the algorithm accurately identifies this cluster as a single cluster (and not multiple clusters). In addition, the remaining extracted values are comparable to those of the actual values. The results of these boundary test cases are relevant to this study since a significant amount of clusters do intersect the boundaries of the domain.

Figure 5.6: Snapshots of the particle concentration field of the 2D test cases. Concentrated regions are shown in red, and less dense areas are shown in blue. The dimensions are $(L_x, L_z) = (4\pi, 2\pi)$ for (a) and $(L_x, L_z) = (\pi/2, \pi/2)$ for (b). Comparisons of the actual and extracted quantities are provided in Table 5.1.

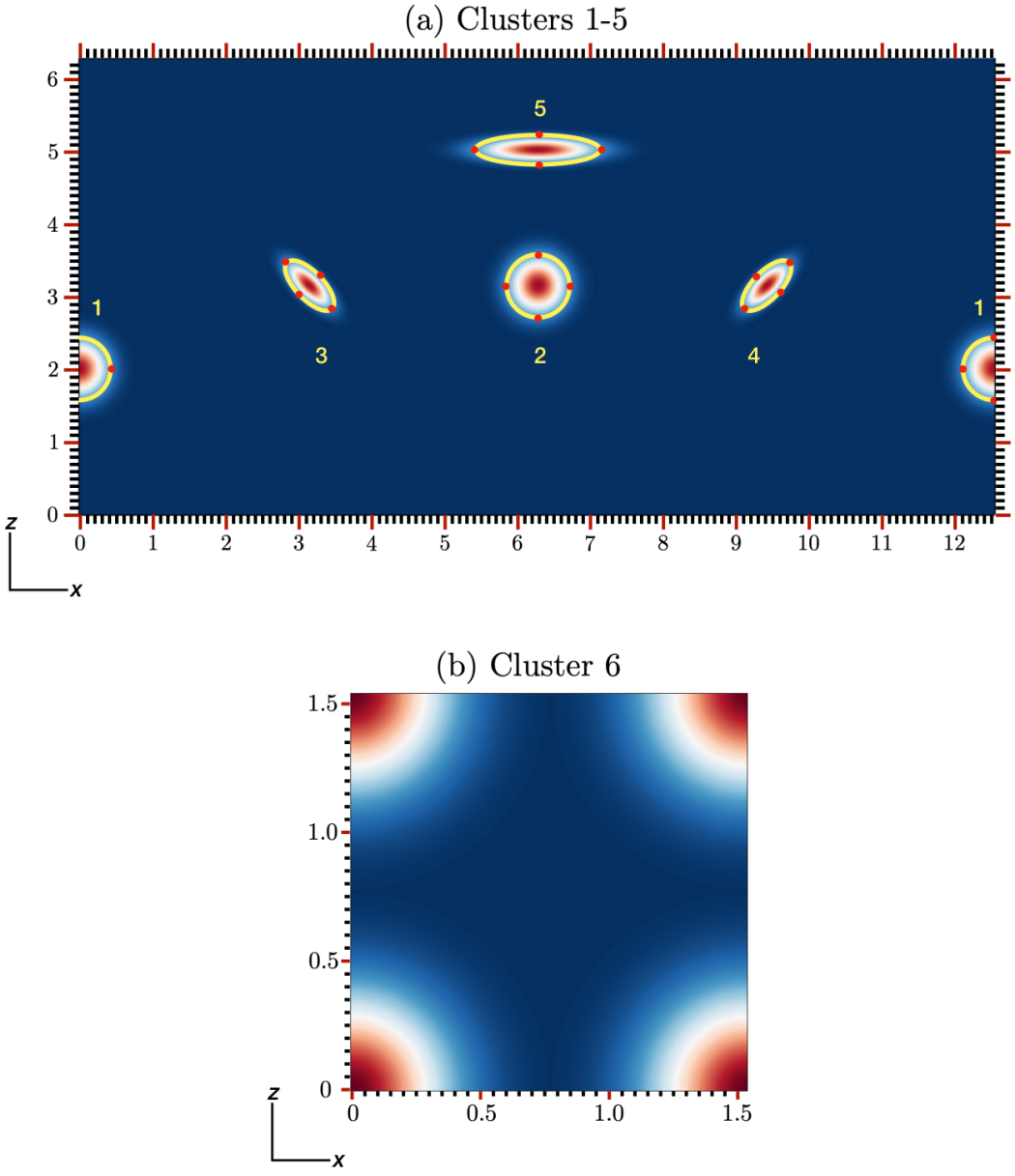

Figure 5.7: Snapshots of the particle concentration field of the 3D test cases taken at $y = L_y/2$. The dimensions are $(L_x, L_y, L_z) = (\pi/2, \pi/2, \pi/2)$ for both (a) and (b). Comparisons of the actual and extracted quantities are provided in Table 5.2.

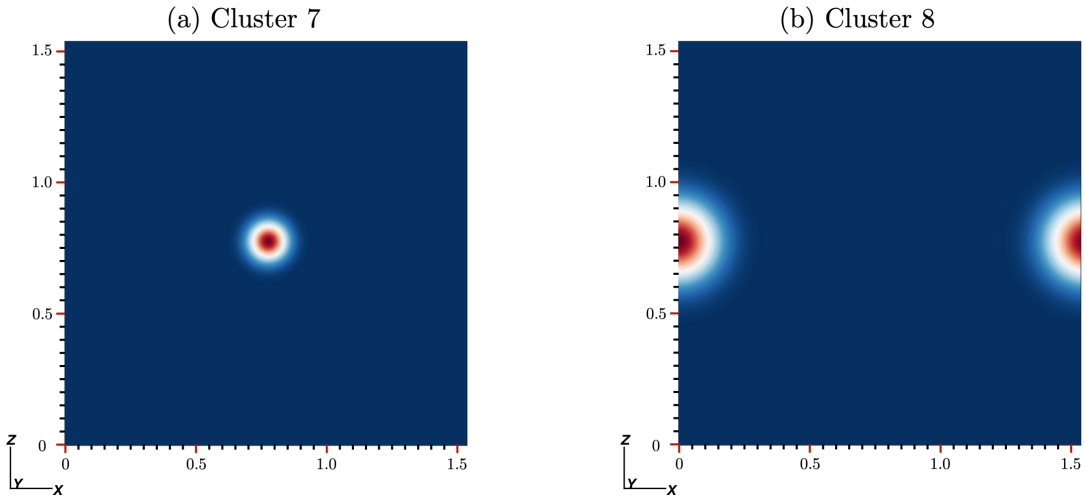

We also present two 3D test cases where each cluster is of the form

$$\hat{r}(x, y, z) \sim \exp\left[-\frac{(x - x_0)^2}{2\sigma_1^2} - \frac{(y - y_0)^2}{2\sigma_2^2} - \frac{(z - z_0)^2}{2\sigma_3^2} \right]. \tag{5.10}$$

We compute similar quantities to those of the 2D test cases and present the results in Table 5.2. We see that as in the 2D test case, the extracted values are comparable to the respective set of actual values.

5.3 Results

In this section, we describe the results of the cluster algorithm applied to the snapshots of the particle concentration field $\hat{r}$ of the 3D DNSs presented in Ch. 4. For each simulation, we apply the algorithm to a single snapshot (taken at one instant in time) only once the system has reached a statistically steady state. For reference, the model set-up is described in Section 4.2 with specifications listed in

Table 5.3. Here we focus our analysis to systems with a particle size range of up to $T_p \approxeq 0.03$ in moderately turbulent flows with $Re \leq 600$.

5.3.1 Properties of the identified clusters

We begin by looking at the properties of the identified clusters detected by the algorithm, which are found for values of $\hat{r} \geq \hat{r}_{crit}$. As previously mentioned in Section 5.2.2, we have selected a value of $\hat{r}_{crit}$ well within the exponential tail of the pdf, which is associated with larger values of $\hat{r}$. For systems with low Stokes number, the tail is fairly short so $\hat{r}_{sup} - \hat{r}_{crit}$ is small. In contrast for higher Stokes number, the exponential tail is much longer due to preferential concentration, and thus, $\hat{r}_{sup} - \hat{r}_{crit}$ is relatively larger.

We therefore investigate the relationship between $\hat{r}_{sup} - \hat{r}_{crit}$ and certain characteristics of the clusters, such as mass and size. We start by looking at the total mass fraction of particles contained within the identified clusters which we define as the ratio of the total mass of the identified clusters to the total particle mass in the system, namely

$$\zeta_m = \frac{\sum_i^{\mathcal{C}} M_i}{L_x L_y L_z}, \tag{5.11}$$

where M_i is the mass of the ith identified cluster (as defined by Eq. 5.6) and $\mathcal{C}$ is the number of identified clusters. Note that because we initialize the system with a uniform distribution of particles with $\hat{r} = 1$ at each grid point, the total particle mass can then be expressed as the volume of the domain, i.e. $L_x L_y L_z$.

In Figure 5.8, we present the mass fraction within clusters ζ_m (5.11) against $d_{\hat{r}} = (\hat{r}_{sup} - \hat{r}_{crit})/\hat{r}_{sup}$. We note that for this figure as well as for Figures 5.9, 5.11, 5.12, 5.16, and 5.19, each point corresponds to an instant in time once the system has reached a statistically steady state for a given simulation. The points in red mark simulations with $Re \geq 300$, and the points in yellow represent simulations

Table 5.3: Summary of numerical simulations, where details of the model set-up can be found in Sec. 4.2. The first column consists of the identification numbers which are used in several figures in this chapter. The second to fifth columns show T_p, r_0, Re, and Pe_p (where we have set $Re_p = Pe_p$). The sixth and seventh columns show $\hat{r}_{crit}$ and $\hat{r}_{sup}$ at an instant in time, where the threshold for all simulations are given by $\hat{r}_{crit} = 1 + 2\,\hat{r}_{rms}$, except the ones listed with an asterisk, where $\hat{r}_{crit} = 1 + 3\,\hat{r}_{rms}$. The eighth column shows the temporally averaged value for $\hat{U}_{rms}$ once the system has reached a statistically steady state. The remaining columns include $\zeta_m, \zeta_v, \mathcal{M}, \bar{\delta}_{\min}$, and $\bar{\delta}_{\max}$ extracted at an instant in time, where the errors represent a standard deviation around the mean. All 3D simulations were run with $(L_x, L_y, L_z) = (4\pi, 2\pi, 2\pi)$ with the corresponding number of grid points used in each direction as $(N_x, N_y, N_z) = (768, 384, 384)$.

No.	T_p	r_0	Re	Pe_p	$\hat{r}_{crit}$	$\hat{r}_{sup}$	$\hat{U}_{rms}$	$\zeta_m \times 10^2$	$\zeta_v \times 10^2$	$\mathcal{M}$	$\bar{\delta}_{\min} \times 10^2$	$\bar{\delta}_{\max} \times 10^2$
1	0.005	0.1	100	600	1.42	1.56	2.28 ± 0.07	0.29	0.19	0.20	4.14 ± 2.27	38.33 ± 2.27
2	0.005	1	600	1000	1.39	2.28	1.80 ± 0.09	0.87	0.60	0.16	2.52 ± 1.13	16.65 ± 1.13
3	0.005	10	600	1000	1.11	1.26	0.71 ± 0.01	0.33	0.29	0.17	3.31 ± 1.92	24.14 ± 1.92
4	0.01	0.1	100	100	1.54	1.87	2.20 ± 0.06	0.44	0.27	0.20	6.64 ± 3.46	51.72 ± 3.46
5	0.01	0.1	100	300	1.56	3.00	2.20 ± 0.09	1.46	0.85	0.43	5.11 ± 3.21	43.22 ± 3.21
6	0.01	0.1	100	600	1.58	2.45	2.22 ± 0.03	1.01	0.60	0.18	5.86 ± 5.12	43.98 ± 5.12
7	0.01	0.1	300	600	1.79	6.36	2.31 ± 0.07	3.08	1.55	0.43	3.11 ± 1.60	22.54 ± 1.60
8	0.01	0.1	600	600	1.72	6.28	2.16 ± 0.06	3.28	1.70	0.31	2.80 ± 1.34	18.09 ± 1.34
8*	0.01	0.1	600	600	2.08	6.28	2.16 ± 0.06	0.65	0.28	0.28	2.47 ± 0.93	17.51 ± 0.93
9	0.01	1	100	100	1.25	1.36	1.49 ± 0.00	0.40	0.31	0.29	7.80 ± 4.81	61.22 ± 4.81
10	0.01	1	100	600	1.47	2.66	1.63 ± 0.02	0.97	0.62	0.68	4.11 ± 2.10	36.37 ± 2.10
11	0.01	1	100	1000	1.54	2.31	1.58 ± 0.03	0.69	0.42	0.17	4.36 ± 3.08	36.85 ± 3.08
12	0.01	1	600	600	1.59	4.21	1.69 ± 0.02	1.09	0.64	0.38	2.96 ± 1.71	21.70 ± 1.71
13	0.01	10	600	600	1.16	1.21	0.69 ± 0.00	0.10	0.08	0.16	4.71 ± 1.74	41.27 ± 1.74
14	0.03	0.1	100	100	1.96	4.78	2.21 ± 0.00	4.88	2.22	0.59	7.11 ± 3.84	61.86 ± 3.84
14*	0.03	0.1	100	100	2.44	4.78	2.21 ± 0.00	0.80	0.30	0.23	5.48 ± 2.48	54.40 ± 2.48
15	0.03	0.1	100	600	2.48	22.17	2.05 ± 0.07	10.99	3.54	0.93	4.42 ± 2.96	34.74 ± 2.96
15*	0.03	0.1	100	600	3.22	22.17	2.05 ± 0.07	3.90	0.97	0.37	4.26 ± 3.38	35.88 ± 3.38
16	0.03	1	100	100	1.64	2.02	1.64 ± 0.00	0.60	0.35	0.17	9.62 ± 3.64	93.59 ± 3.64
17	0.03	1	100	1000	2.05	9.28	1.57 ± 0.03	5.68	2.38	0.41	3.82 ± 2.04	32.21 ± 2.04

with low $Pe_p = 100$; otherwise, the remaining simulations are shown in blue. We also include several points with a higher detection threshold of $\hat{r}_{crit} = 1 + 3\,\hat{r}_{rms}$ in green. The number next to each point refers to the number of the simulation listed in Table 5.3, where its characteristics can be found.

We see on Figure 5.8 that for $d_{\hat{r}} < 0.2$, the data points appear to be grouped together with relatively small values of ζ_m ranging from 10^{-3} to 10^{-2}. These points correspond to systems in which preferential concentration is not dominant, consisting of smaller values of T_p and Pe_p. In contrast as we move along to larger values of $d_{\hat{r}} \geq 0.4$, for which preferential concentration is significant, ζ_m spans larger values of ζ_m from about 10^{-2} to 10^{-1}. These points refer to simulations with larger $T_p \geq 0.01$ (with $r_0 \leq 1$ and $Pe_p \geq 300$). For the alternative analysis of simulations $8, 14$, and 15 using $\hat{r}_{crit} = 1+3\,\hat{r}_{rms}$, the green points are shifted to the left and down compared to the corresponding ones obtained using $\hat{r}_{crit} = 1+2\hat{r}_{rms}$, as expected from the selection of a higher density threshold. It is interesting to note that the data appears to collapse to some universal curve, at least for a given choice of σ (i.e. the green points, which have $\sigma = 3$ seem to lie somewhat below all the other points, which have $\sigma = 2$).

We next explore if the identified clusters occupy a significant volume fraction of the domain. To do so, we consider the total volume fraction of the identified clusters defined by

$$\zeta_v = \frac{\sum_i^{\mathcal{C}} V_i}{L_x L_y L_z} = \frac{\sum_i^{\mathcal{C}} N_i}{N_x N_y N_z}, \tag{5.12}$$

where $V_i = N_i\,\Delta x\,\Delta y\,\Delta z$ is the volume of the ith cluster and N_i is the number of elements (or grid points) for that same cluster. In Figure 5.9, we present the volume fraction ζ_v against $d_{\hat{r}} = (\hat{r}_{sup} - \hat{r}_{crit})/\hat{r}_{sup}$. We see a similar trend as in Figure 5.8, where larger values of $d_{\hat{r}}$ result in larger volume fractions ζ_v. However it is surprising that for the largest value of $d_{\hat{r}} \approx 0.9$, the value of ζ_v remains

Figure 5.8: Mass fraction of the identified clusters ζ_m versus $d_{\hat{r}} = (\hat{r}_{sup} - \hat{r}_{crit})/\hat{r}_{sup}$. The number next to each point refers to the number of the simulation listed in Table 5.3, where $\hat{r}_{crit} = 1 + 2\hat{r}_{rms}$ except for select simulations shown in green with $\hat{r}_{crit} = 1 + 3\hat{r}_{rms}$. The points in red mark simulations with $Re \geq 300$, and the points in yellow represent simulations with low $Pe_p = 100$; otherwise, the remaining simulations are shown in blue.

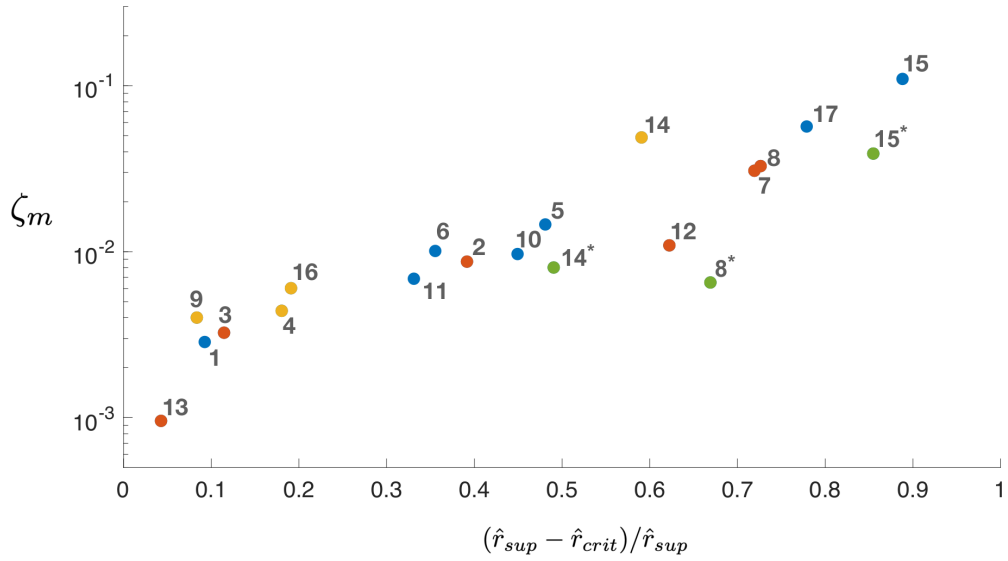

relatively low, on the order of $O(10^{-2})$, given that the relative mass contained in the clusters can reach values close to 0.1 (se Figure 5.8). This demonstrates that the mean value of the particle density within clusters has increased quite significantly.

5.3.2 Properties of the most massive cluster

Since we are interested in the properties of extreme events in particle concentration such as $\hat{r}_{sup}$, we now focus on the most massive cluster for each simulation, which we refer to as the "MMC" hereafter. In Figure 5.10, we present a snapshot of the particle concentration field $\hat{r}$ of the MMC for simulations with two different values of T_p (with the remaining parameters set as $r_0 = 0.1$, $Re = 100$, and $Re_p = Pe_p = 600$). We clearly see that the MMC varies in size, where for

Figure 5.9: Volume fraction of the identified clusters ζ_v versus $d_{\hat{r}} = (\hat{r}_{sup} - \hat{r}_{crit})/\hat{r}_{sup}$. The number next to each point refers to the number of the simulation listed in Table 5.3, where $\hat{r}_{crit} = 1 + 2\hat{r}_{rms}$ except for select simulations shown in green with $\hat{r}_{crit} = 1 + 3\hat{r}_{rms}$. The points in red mark simulations with $Re \geq 300$, and the points in yellow represent simulations with low $Pe_p = 100$; otherwise, the remaining simulations are shown in blue.

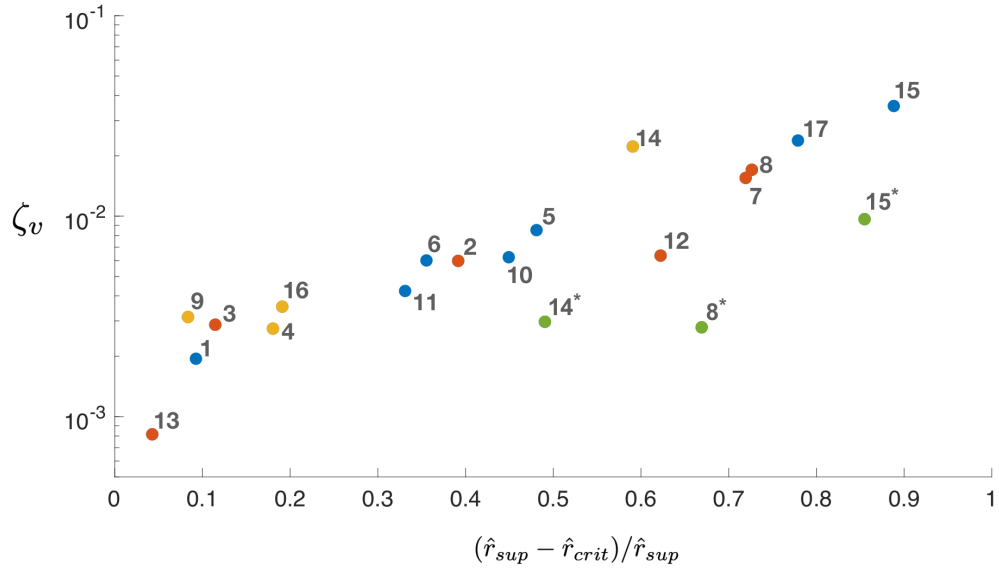

the smaller $T_p = 0.01$, the MMC occupies a small fraction of the domain. On the other hand for larger $T_p = 0.03$, the MMC appears to take up almost the entire volume of the domain.

Figure 5.10: Snapshot of the particle concentration field of the massive cluster (MMC) for $T_p = 0.01$ (simulation 6 in Table 5.3) and $T_p = 0.03$ (simulation 15 in Table 5.3) with the remaining parameters set as $r_0 = 0.1, Re = 100, Pe_p = 600, Re_p = 600$. The minimum value of the colorbar corresponds to $\hat{r}_{crit}$.

(a) $T_p = 0.01$

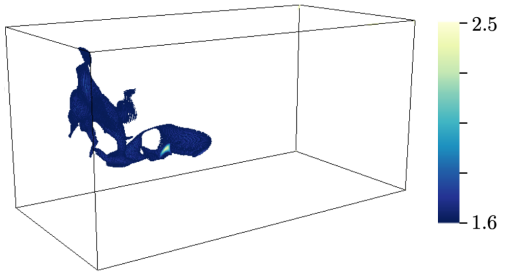

(b) $T_p = 0.03$

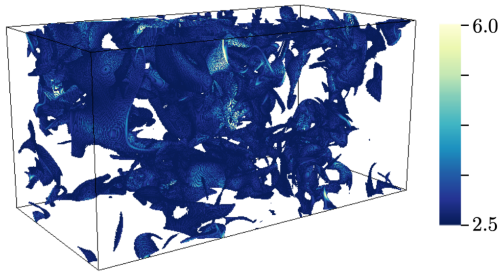

To gain further insight on why the size of the MMC increases with T_p so much, we can look at the ratio of the mass of the MMC to the total mass of the identified clusters given by

$$\mathcal{M} = \frac{\max M_i}{\sum_i^{\mathcal{C}} M_i}. \tag{5.13}$$

This ratio quantifies how dominant the MMC is compared with all the other identified clusters: when $\mathcal{M}$ is small, the MMC mass is presumably not much larger than the average mass of other clusters in the simulation, while when $\mathcal{M}$ is closer to one, the MMC contains almost all of the mass of the identified clusters.

In Figure 5.11, we present the relative mass $\mathcal{M}$ against $d_{\hat{r}} = (\hat{r}_{sup} - \hat{r}_{crit})/\hat{r}_{crit}$ for each simulation found in Table 5.3. We find that for $d_{\hat{r}} \leq 0.4$, most of the simulations have a mass fraction $\mathcal{M} \approx 0.2$, implying that the MMC contains about 20% of the total mass of dense clusters. In contrast for larger $d_{\hat{r}}$, almost all of the simulations are found to have $\mathcal{M} \geq 0.3$, found within the region boxed in yellow. We see that for several simulations consisting of higher T_p (specifically for simulations 10, 14, and 15), $\mathcal{M} \gtrapprox 0.6$, where one simulation has an exceedingly large mass fraction of $\mathcal{M} \approx 0.9$.

We originally speculated that the unexpected size of the MMC relative to the others in these simulations was due to the neighbor definition set in Section 5.2, which ultimately determines the size of a single cluster. Recall that in 3D we impose the condition that two elements are neighbors (and thus part of the same cluster) if they touch one another on their faces, edges, or corners. Therefore, a neighboring element simply needs to be within the neighborhood of the 26 elements surrounding the current one. We explored the effect of restricting this neighborhood size further by imposing the condition that two elements are neighbors only if they touch one another on their faces, decreasing the neighborhood size to 6 elements. However, we found that this condition did not significantly

change the size of the MMC, nor the size of the other clusters in the simulation. From here on, we therefore continue with the original definition of connectivity.

In order to understand why and when the MMC becomes so dominant, we note that this is certainly the natural outcome one may expect when the volume fraction of the domain occupied by clusters becomes large, and the probability that they are connected increases (hence appearing as one large cluster instead of several small ones). To analyze this more quantitatively, Figure 5.12 shows the relative mass fraction of the MMC $\mathcal{M}$, versus the total volume fraction ζ_v of all the clusters. We see there appears to be a sharp transition between simulations at low volume fraction (for which $\mathcal{M}$ remains small), and simulations at a volume fraction of ~ 0.01, where $\mathcal{M}$ suddenly jumps to much larger values.

Figure 5.11: Relative mass of the MMC $\mathcal{M}$ versus $d_{\hat{r}} = (\hat{r}_{sup} - \hat{r}_{crit})/\hat{r}_{sup}$. The number next to each point refers to the number of the simulation listed in Table 5.3, where $\hat{r}_{crit} = 1 + 2\hat{r}_{rms}$ except for select simulations shown in green with $\hat{r}_{crit} = 1 + 3\hat{r}_{rms}$. The points in red mark simulations with $Re \geq 300$, and the points in yellow represent simulations with low $Pe_p = 100$; otherwise, the remaining simulations are shown in blue.

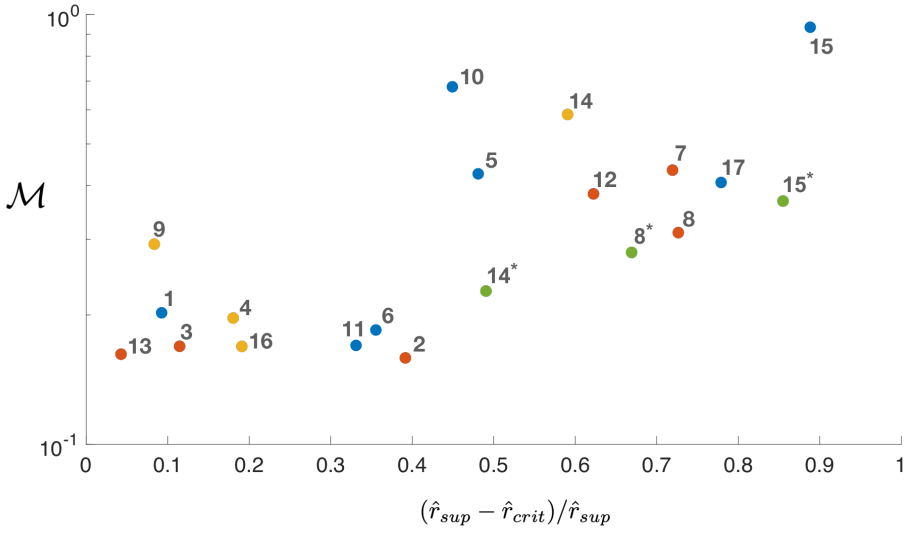

Figure 5.12: Relative mass of the MMC $\mathcal{M}$ as a function of volume fraction of the identified clusters ζ_v. The number next to each point refers to the number of the simulation listed in Table 5.3, where $\hat{r}_{crit} = 1 + 2\hat{r}_{rms}$ except for select simulations shown in green with $\hat{r}_{crit} = 1 + 3\hat{r}_{rms}$. The points in red mark simulations with $Re \geq 300$, and the points in yellow represent simulations with low $Pe_p = 100$; otherwise, the remaining simulations are shown in blue.

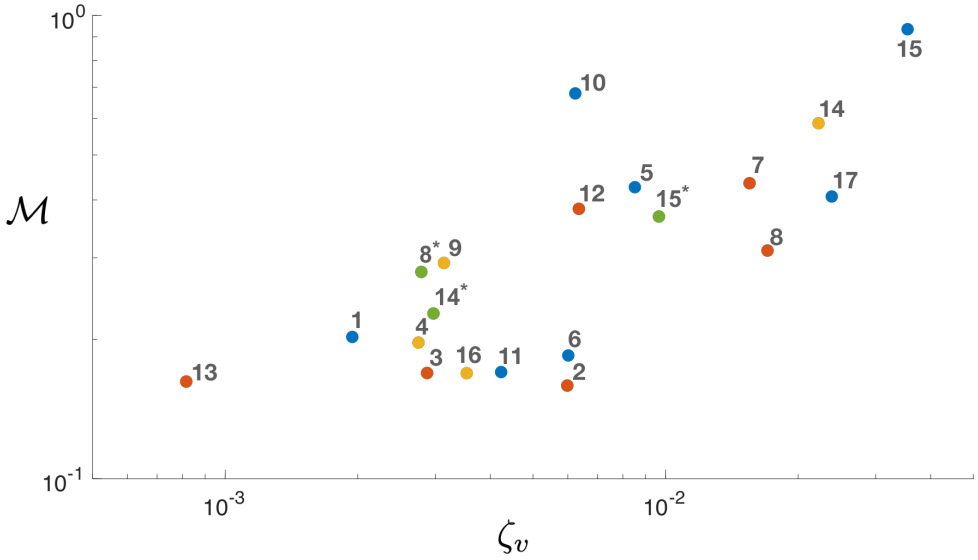

5.3.3 Connectivity

However, we were initially very surprised to find that the transition between low $\mathcal{M}$ to high $\mathcal{M}$ happens at relatively small volume fraction of 0.01. Indeed, it is easy to show that if the clusters are spherical, and occupy a volume fraction close to 0.01, they are not expected to be connected (and therefore would not appear as a single large cluster).

To show this, let's assume the clusters are spherical with radius r_c. Thus for two clusters to touch, their centers merely need to be within $2r_c$ of one another as shown by Figure 5.13.

We assume that the probability that a cluster is located at a given position is uniform in the domain. Then the probability that two clusters are within a

Figure 5.13: Two spherical clusters with radius r_c touch if their centers are within a distance $2r_c$ of one another.

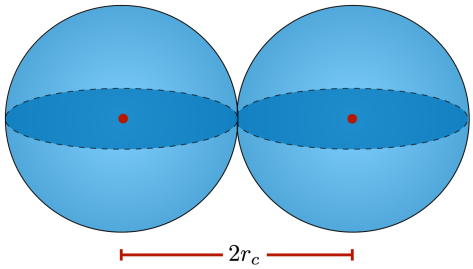

distance of $2r_c$ is given by the volume of the sphere of radius $2r_c$ divided by the volume of the domain, namely

$$\frac{\frac{4}{3}\pi(2r_c)^3}{L_x L_y L_z} = 8\Phi_c, \tag{5.14}$$

where Φ_c is the volume fraction of a single spherical cluster.

Following the same logic if there are $\mathcal{N}$ clusters in the domain, the probability that another cluster touches the MMC is

$$8(\mathcal{N}-1)\,\Phi_c \simeq 8\zeta_v. \tag{5.15}$$

We see that if $\zeta_v \simeq 0.01$, then the probability of any cluster touching the MMC is around 0.08, which is too low to explain the predominance of large values of $\mathcal{M}$ for $\zeta_v \sim O(0.01)$. This shows that the results presented in Figure 5.12 are inconsistent with spherical clusters, and that instead, the transition observed at $\zeta_v = 0.01$ must be due to the fact that the clusters are strongly aspherical.

5.3.4 Shape of the clusters

We take a closer look at the shape of the identified clusters, by first examining the ratio of the largest dimension of the cluster $\hat{\delta}_{\max}$ to the smallest dimension (also referred to as the "thickness") of the cluster $\hat{\delta}_{\min}$, extracted using the method described in Section 5.2.

In Figure 5.14, we present this aspect ratio $\hat{\delta}_{\max}/\hat{\delta}_{\min}$ measured in each cluster, a function of the maximum cluster density $\varrho_{sup,i}$, for three simulations with varying T_p (other parameters being held the same, and equal to $r_0 = 0.1, Re = 100, Pe_p = 600, Re_p = 600$, listed as simulations 1, 6, and 15 in Table 5.3, respectively). Each data point represents a single cluster for a given simulation at an instant in time. We clearly see that the majority of the clusters have an aspect ratio of about 5 to 15, with several clusters from each simulation exceeding an aspect ratio of 20. This signifies that the majority of clusters for the simulations presented here are not spherical.

We also circle the MMC in red for each simulation, and find that the MMC has a lower aspect ratio compared to clusters with lower $\varrho_{sup,i}$. Note that this is not the case in all the simulations (where the MMC is sometimes very elongated). We can explain this by presenting zoomed-in snapshots of $\hat{r}$ from a simulation with $T_p = 0.01, r_0 = 0.1, Re = 100, Pe_p = 600, Re_p = 600$ (listed as simulation 6 in Table 5.3). We see on the left in Figure 5.15(a) that the densest regions are found near the edges of the obvious vortex structure, as expected from Maxey's theory. Once the algorithm is applied and only data with $\hat{r} \geq \hat{r}_{crit}$ is kept, as shown in Figure 5.15(b), two clusters are identified.

We also see that the aspect ratio appears to be of order unity for the denser cluster, but much thinner for the weaker cluster, consistent with Figure 5.14. However, we now also see why this may be the case: in the MMC, $\mathbf{x}_{sup,i}$ is deeply

Figure 5.14: Aspect ratio of the clusters $\hat{\delta}_{\max}/\hat{\delta}_{\min}$ as a function of $\varrho_{sup,i}$ for a simulation with varying T_p with $r_0 = 0.1, Re = 100, Pe_p = 600, Re_p = 600$ (listed as simulations 1, 6, and 15 in Table 5.3). Note that the lower limit for $\varrho_{sup,i}$ in each simulation is $\hat{r}_{crit}$, equal to 1.4, 1.6, and 2.5, respectively as T_p increases. The MMC is circled in red in each case.

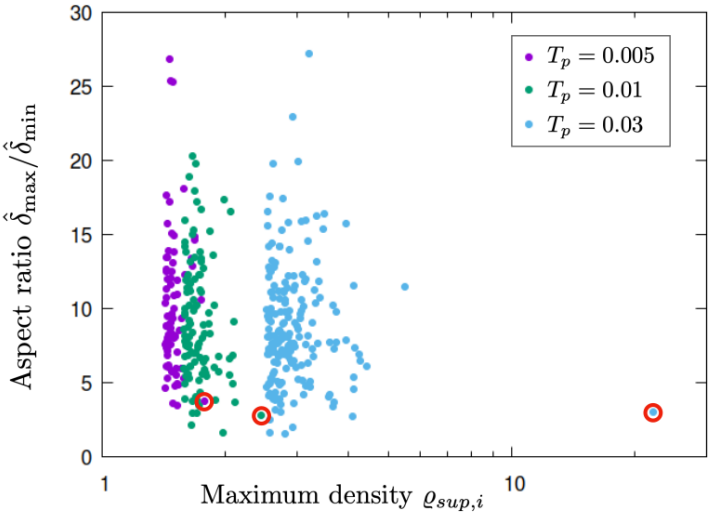

Figure 5.15: (a) Zoomed-in snapshot of $\hat{r}$ for a simulation with $T_p = 0.01, r_0 = 0.1, Re = 100, Pe_p = 600, Re_p = 600$ (listed as simulation 6 in Table 5.3). The corresponding snapshot (b) depicts the clusters identified by the algorithm, with the colorbar spanning values from $\hat{r}_{crit}$ to $\hat{r}_{sup}$.

(a)

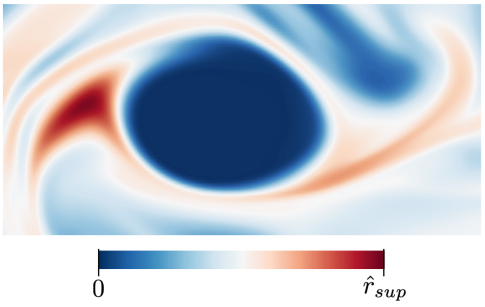

(b)

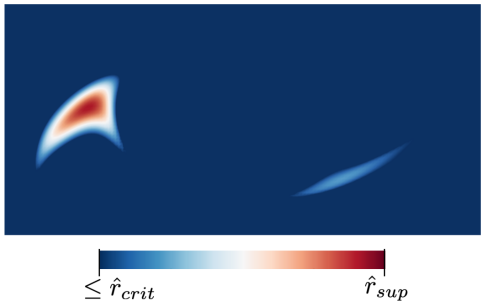

embedded in a sizable region of $\hat{r} \geq \hat{r}_{crit}$, and the isocontours of $\hat{r}$ around $\varrho_{sup,i}$ are elliptical (but do not have a particularly extreme aspect ratio). On the other hand, the weaker cluster has a maximum density that is barely above $\hat{r}_{crit}$, and

therefore traces the edge of the $\hat{r} = \hat{r}_{crit}$ isocontour, which accordingly is sheet-like or rod-like and has a relatively large aspect ratio.

For completeness, we also look at the average aspect ratio $\bar{\delta}_{\max}/\bar{\delta}_{\min}$ and the aspect ratio $\hat{\delta}_{\max}/\hat{\delta}_{\min}$ of the MMC for each simulation in Table 5.3. In Figure 5.16, we present two sets of data points, where the first is comprised of the filled data points which capture the relationship between the mean largest dimension $\bar{\delta}_{\max}$ against the mean thickness $\bar{\delta}_{\min}$ of the identified clusters for a given simulation. The second dataset consists of the non-filled points for which we extract $\hat{\delta}_{\max}$ versus $\hat{\delta}_{\min}$ for the MMC. We clearly see that the filled data points follow the scaling $\bar{\delta}_{\max} \simeq 10\,\bar{\delta}_{\min}$, given by the black dashed line, suggesting that the typical aspect ratio is approximately 10 for all simulations. This may not be entirely unexpected since for the simulations presented in Figure 5.14, the aspect ratio of the clusters is also centered around 10. On the other hand, we previously postulated that the aspect ratio of the MMC (as circled in red in Figure 5.14) may be smaller than the average. However this is clearly not the case when we consider all simulations in Figure 5.16, where we see that for most cases, the aspect ratio $\hat{\delta}_{\max}/\hat{\delta}_{\min}$ of the MMC is also approximately 10 with some degree of variability.

We can next investigate the shape of the clusters (to determine whether they are more rod-like or more sheet-like) by looking at the respective ratio of the Hessian eigenvalues λ_3/λ_2, and λ_2/λ_1 (see Section 5.2), where by definition λ_1 is the smallest eigenvalue and λ_3 is the largest. The results are presented in Figure 5.17, where we present λ_3/λ_2 as a function of λ_2/λ_1. Each data point represents a single cluster from a simulation with $T_p = 0.01, r_0 = 0.01, Re = 100, Pe_p = 600$, and $Re_p = 600$ (listed as simulation 6 in Table 5.3 for details). For reference, we have also circled the MMC in red. Note that if the clusters were indeed spherical,

Figure 5.16: Largest dimension versus the smallest dimension, where we look at the average dimensions using $\bar{\delta}_{\max}$ and $\bar{\delta}_{\min}$ represented by the filled data points, and the dimensions of the MMC $\hat{\delta}_{\max}$ and $\hat{\delta}_{\min}$ represented by the non-filled data points. The number next to each point refers the the number of the simulation listed in Table 5.3.

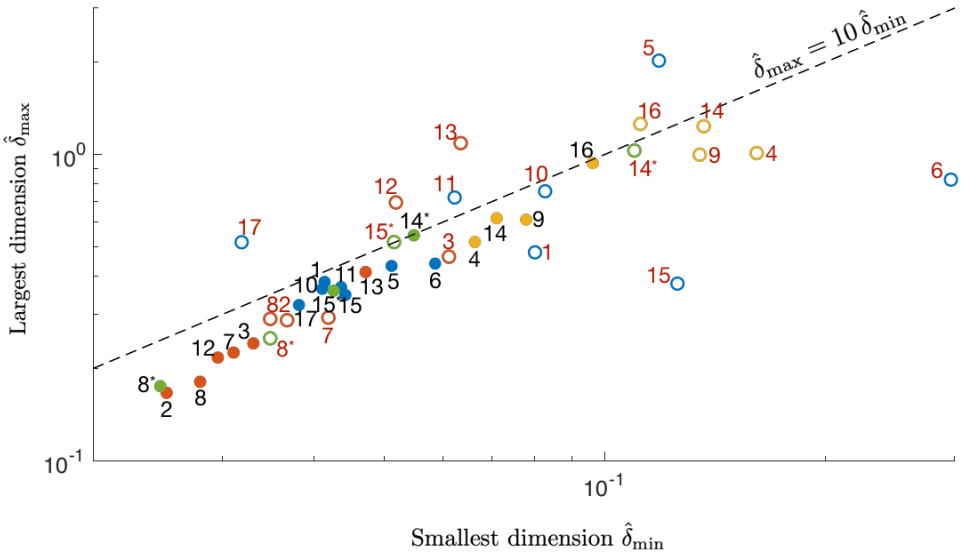

then the data points would be found at the bottom left-hand corner with $\lambda_3/\lambda_2 = 1$ and $\lambda_2/\lambda_1 = 1$, which is not the case for any of the clusters shown here.

We see instead that the ratio of the two smaller sides λ_2/λ_1 are found primarily in the range from 1 to 20, and the ratio of the two larger sides λ_3/λ_2 are found to span a larger range from about 1 to 100. Given that the majority of the points lie about $\lambda_3/\lambda_2 = 10$ with $\lambda_2/\lambda_1 \leq 10$, we can confirm that the clusters are more likely to be rod-like in shape. We also see several cases in which the shape of the clusters are sheet-like. These points are found in the right-hand side represented by values for λ_3/λ_2 that are relatively small compared to λ_2/λ_1.

Figure 5.17: Comparison of dimension lengths with λ_3/λ_2 as a function of λ_2/λ_1 for a simulation with $T_p = 0.01, r_0 = 0.1, Re = 100, Pe_p = 600, Re_p = 600$ (listed as simulation 6 in Table 5.3).

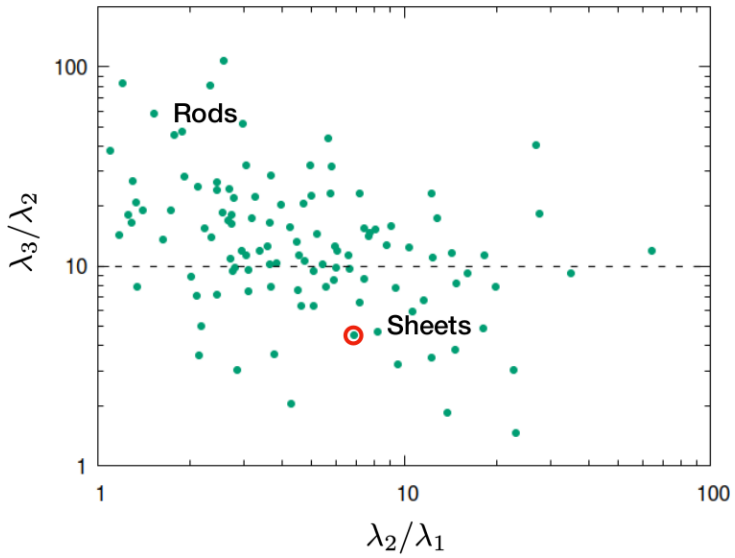

5.3.5 Quantifying the size of the clusters

Next, in order to better understand how the input parameters affect the size of the clusters, we look at how the thickness $\hat{\delta}_{\min}$ varies with respect to T_p, Re, and Pe_p (where we have assumed here that $Re_p = Pe_p$). Figure 5.18 shows pdfs that represent the probability $p(\hat{\delta}_{\min})$ of a cluster to have a thickness value that lies between $\hat{\delta}_{\min}$ to $\hat{\delta}_{\min} + \Delta\hat{\delta}$, where $\Delta\hat{\delta} = 0.005$. Note that the thickness of a cluster is measured around $\mathbf{x}_{sup,i}$ along its thin dimension (and not the typical length of an entire cluster).

The blue pdf in Figures 5.18(b)-(d) represents a reference simulation with $T_p = 0.01, r_0 = 0.1, Re = 100, Pe_p = 600$, and $Re_p = 600$ (given by simulation number 6 in Table 5.3), whose corresponding snapshot of $\hat{r}$ is given by Figure 5.18(a). To help visualize the thickness of the clusters in comparison to the reference simulation, we also include the snapshot of $\hat{r}$ next to the pdf in red for Figures

5.18(b)-(d). The colorbar of the snapshots is created to show $\hat{r} < \hat{r}_{crit}$ in dark blue, so that the clusters are easily distinguished.

We begin with Figure 5.18(a) in which we compare the results of the reference simulation to another with lower value of $T_p = 0.005$, while keeping $r_0 = 0.1, Re = 100, Pe_p = Re_p = 600$ constant (corresponding to simulations 1 and 6 in Table 5.3). We see that the pdf thickness is overall unaffected. This is consistent with the snapshots shown for (a) and (b), where we see that the thickness of the particle structures in regions of high density is about the same size for varying T_p. Next in Figure 5.18(b), we compare the reference simulation with another at higher $Re = 600$, while holding $T_p = 0.01, r_0 = 0.1, Pe_p = Re_p = 600$ constant (corresponding to simulations 6 and 8 in Table 5.3). We see the clusters are both more numerous, as well as smaller and thinner; this can be seen both in the size pdf, and in the snapshots. Finally in Figure 5.18(c), we compare the reference simulation with one at lower $Pe_p = Re = 100$, while holding $T_p = 0.01, r_0 = 0.1, Re = 100$ constant (corresponding to simulations 4 and 6 in Table 5.3). Although the pdfs are quite similar, there is a slight increase in thinner clusters for larger Pe_p. This is consistent with a visual comparison of the snapshots (d), which show that the clusters are thinner at larger Pe_p, consistent with the fact that the particle diffusivity is smaller in that case.

Figure 5.18: Probability distribution functions for the thickness $\hat{\delta}_{\min}$ for (b) varying T_p, (c) varying Re, and (d) varying Pe_p and Re_p at an instant in time from simulations that have reached a statistically steady state. The blue pdf represents a reference simulation where $T_p = 0.01, r_0 = 0.1, Re = 100, Pe_p = 600, Re_p = 600$ (simulation number 6 in Table 5.3), where the corresponding snapshot of $\hat{r}$ is shown in (a).

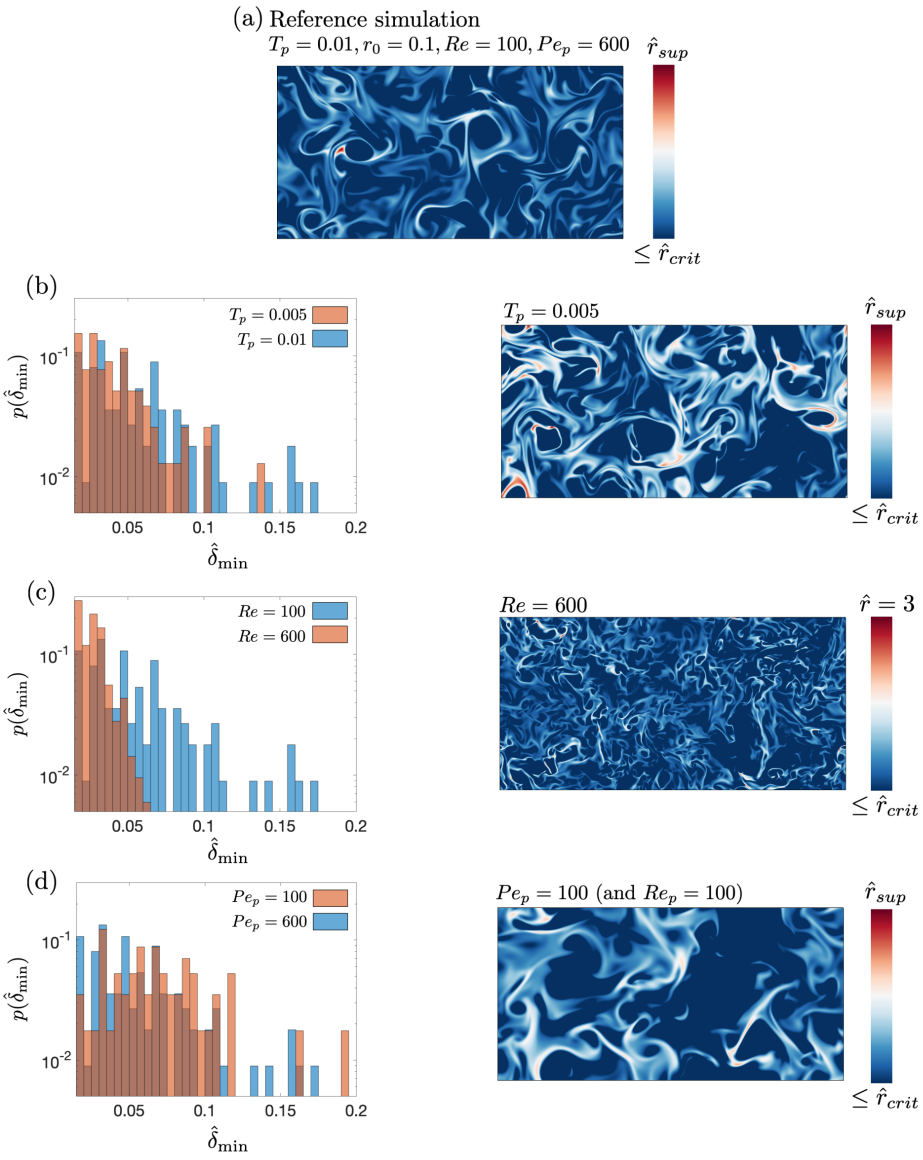

We explored several possible models and ideas to quantify the dependence of the cluster thickness with input parameters. One of the models explored considers

that these elongated clusters may be modeled as advection-diffusion boundary layers in the particle field. The balance between advection and diffusion in the particle transport equation (5.3) reads as

$$\hat{\mathbf{u}}_p \cdot \nabla \hat{r} \sim \frac{1}{Pe_p} \nabla^2 \hat{r}. \tag{5.16}$$

After applying dimensional analysis, we can solve for a lengthscale

$$\hat{\delta} \sim \frac{1}{\hat{U}_{rms} Pe_p}, \tag{5.17}$$

which we assume is a first estimate of $\hat{\delta}_{\min}$ for a single cluster.

We test the scaling (5.17) against the average thickness of all clusters in a given simulation, given by $\bar{\delta}_{\min}$ (shown by the circular points) in Figure 5.19. We also show, for comparison, the average largest dimension $\bar{\delta}_{\max}$ (shown by the triangular points) for all simulations listed in Table 5.3. For each point, we include errorbars that represent one standard deviation around the mean thickness. Here we use the same color scheme as previous plots, where the yellow color corresponds to low $Pe_p = 100$, the red color corresponds to high $Re \geq 300$, and the blue color corresponds to remaining simulations for which $\hat{r}_{crit} = 1 + 2\,\hat{r}_{rms}$; otherwise, the green color represents $\hat{r}_{crit} = 1 + 3\,\hat{r}_{rms}$. The predicted scalings, namely $\bar{\delta} \sim (\hat{U}_{rms} Pe_p)^{-1}$ are shown as solid black lines.

Focusing on the circular points corresponding to $\bar{\delta}_{\min}$ first, we see that the scaling appears to hold for low Pe_p (shown in yellow). On the other hand for those points on the right with effectively larger Re or higher $\hat{U}_{rms}$, the points appear to asymptote to a constant value that is close to twice the resolution for our simulations given by $2(L_z/N_z)$. In other words, the value extracted for $\bar{\delta}_{\min}$ on this side of the figure may be an artifact of the truncation set by the grid scale

of our simulations.

Moving on to the triangular points corresponding to $\bar{\delta}_{\max}$, we see that they follow a very similar trend to the the one found for $\bar{\delta}_{\min}$, which is consistent with our earlier finding that $\bar{\delta}_{\max} \simeq 10\bar{\delta}_{\min}$. Once again simulations with low Pe_p appear to follow the scaling law associated with an advection diffusion balance, but as we move to the right, the points asymptote to a constant. Interestingly, $\bar{\delta}_{\max}$ seem to approach the Taylor microscale computed for the corresponding value of Re (see horizontal lines). This result is consistent with the findings of Chapter 4 (see Section 4.3) where we saw that the power spectrum of the particle concentration field peaks near the Taylor microscale. In this case, by contrast with $\hat{\delta}_{\min}$, the results are not expected to be constrained by the numerical resolution, so they are likely robust.

Figure 5.19: Average thickness $\bar{\delta}_{\min}$ (circular points) and $\bar{\delta}_{\max}$ (triangular points) against $\hat{U}_{rms}Pe_p$. The two solid lines represent the scaling $\bar{\delta} \sim (\hat{U}_{rms}Pe_p)^{-1}$. The dashed horizontal line represents $\bar{\delta} = 2(L_z/N_z)$, and the blue and red dotted lines correspond to the Taylor microscale $\hat{\lambda}$ for $Re = 100$ and $Re = 600$, respectively. Errorbars for each data point represent one standard deviation around the mean. The labels represent the simulation number found in Table 5.3.

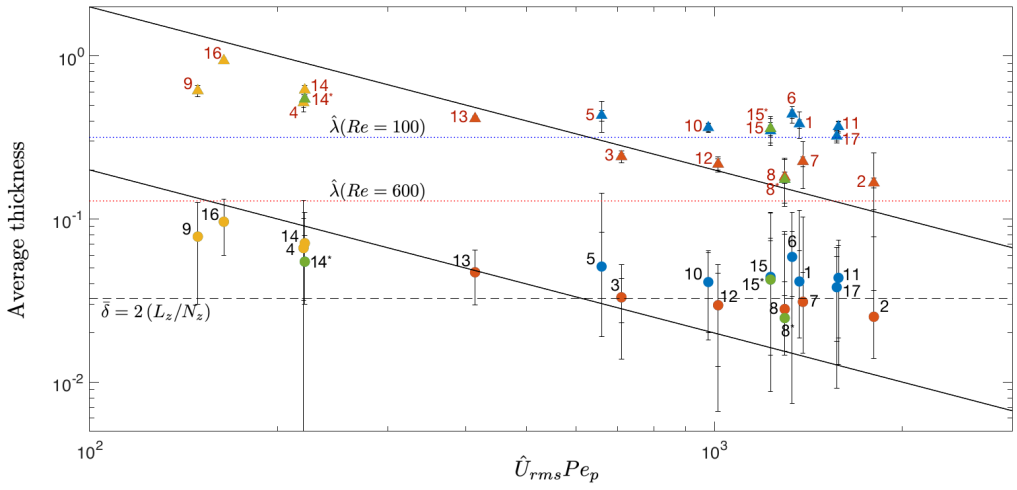

5.3.6 Shape of the probability distribution function

The second question of interest raised earlier is to try and understand how the largest clusters in the simulations contribute to the shape of the particle density pdfs originally presented in Section 4.4.2, focusing in particular on the exponential tail of the pdf. That is, we are interested in determining whether the tail is mostly associated with a single, or a few larger clusters, or whether it is created by the sum of many smaller clusters. To do so, we present pdfs of $\hat{r}$ for $T_p = 0.005$ (a) and for $T_p = 0.01$ (b), where we hold the other parameters to be $r_0 = 0.1, Re = 100, Pe_p = 600, Re_p = 600$. These are listed as simulations 1 and 6 in Table 5.3. The value for $p(\hat{r})$ represents the probability of one grid point in the simulation to have a particle concentration whose value lies between $\hat{r}$ and $\hat{r} + \Delta\hat{r}$, where $\Delta\hat{r} = 0.002$. Since we are interested in the contributions from the clusters identified by the algorithm, we have set the minimum value on the x-axis to be equal to $\hat{r}_{crit} = 1 + 2\,\hat{r}_{rms}$. The black histogram captures the pdf for $\hat{r}$, while the colored histograms represent the individual contribution from the five most massive clusters. The cluster pdfs are labeled in such a way that cluster no. 1 is the MMC, cluster no. 2 is the second massive cluster, etc.

For the low T_p simulation shown in Figure 5.20(a), we note first that the shape of the total particle density pdf at the highest values of $\hat{r}$ is not determined by the MMC (shown in red) but rather by two clusters no. 2 and 3, which contain the points with the highest density. We also see that the shape of the pdf for lower values of $\hat{r}$ is not determined by those five clusters alone since the sum of probabilities for a given $\hat{r}$ is significantly smaller than $p(\hat{r})$ of the total density pdf (in black). On the other hand for larger $T_p = 0.01$, the MMC clearly dominates across the entire range from $\hat{r}_{crit}$ to $\hat{r}_{sup}$, compared to the other four clusters. In this case, we see that the shape of the total density pdf for the highest

values of $\hat{r}$ can solely be attributed to the MMC. However, we see again that for smaller values of $\hat{r}$, the shape of the total pdf cannot be accounted for by the five most massive clusters alone, and must instead be due to the combination of many smaller clusters instead. We note that the pdfs of the largest clusters in this simulation are also exponential. However, we also know that, had we selected a higher $\hat{r}_{crit}$, these would be split into a number of smaller clusters. We therefore generally hypothesize that the exponential tail of the pdf results from the superposition of many small clusters whose own density pdf may not be exponential.

Figure 5.20: Probability distribution functions for $\hat{r}$ simulations with (a) $T_p = 0.005$ and (b) $T_p = 0.01$ (with $r_0 = 0.1, Re = 100, Pe_p = 600, Re_p = 600$). The black histogram represents the pdf for $\hat{r}$, where we have set the minimum value of $\hat{r} = \hat{r}_{crit}$. The colored curves represent the top five massive curves (with respect to M_i).

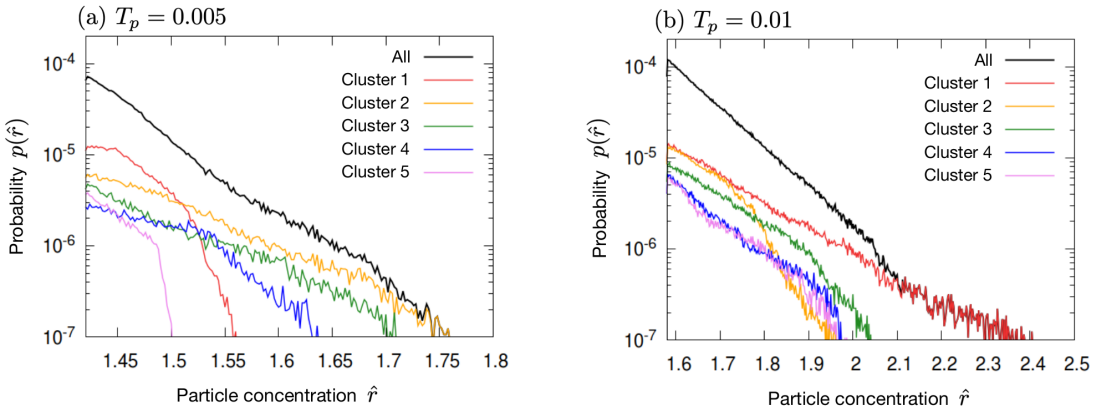

5.4 Summary and discussion

In Chapters 3 and 4 we first observed that regions of high densities typically consisted of fine, elongated particle structures due to preferential concentration. Thus in this chapter, we aimed to identify key features of these structures such

as the typical aspect ratio, size distribution, volume fraction, etc. that may help better understand the impact of preferential concentration on particle growth.

We focused our study on the 3D DNSs originally presented in Chapter 4, in which the turbulence of the system was mechanically-driven by a sinusoidal shear. There, we showed that when preferential concentration occurs, an exponential tail associated with large densities appears in the pdf for $\hat{r}$ (see Figure 4.12). Thus, in order to focus on clusters whose densities are within the exponential tail, we restricted our analysis to particle structures of densities several standard deviations above the mean.

We used a box-counting algorithm to identify the regions of denser concentrations, and accordingly labeled the connected regions as clusters. We found that the clusters generally take the form of thin, elongated structures, with a typical aspect ratio of about 10. Additionally upon further examination of the density field near the center of each cluster, we showed that the cluster shape is found to be either rod-like or sheet-like. These results coincide with the qualitative data of the particle concentration field presented in Chapter 4 (see Figures 4.3 and 4.7).

We also looked at how $\hat{r}_{sup} - \hat{r}_{crit}$ was related to the mass and size of the identified clusters. We noted that larger $\hat{r}_{sup} - \hat{r}_{crit}$ associated with preferential concentration often resulted in larger total mass fraction ζ_m and total volume fraction ζ_v of the clusters. However, we also found that ζ_v remained rather small, with values no more than 10% across all simulations regardless of the value for $\hat{r}_{sup} - \hat{r}_{crit}$. To see why this may be the case, we looked at a particular cluster in the domain: the most massive cluster (MMC). We found that a significant proportion of the mass (and volume) of the clusters were found in the MMC, as well as $\hat{r}_{sup}$. Although one may argue that the existence of the MMC is an artifact of how the algorithm identifies the clusters, we nevertheless observed that

the largest concentrations were located within one region of the domain, which has potential implications to applications for which particle growth is relevant. For instance we can extend the existence of the MMC to clouds, where we would then expect to see a relatively large region consisting of higher concentrations of droplets, where rain formation is most likely to occur.

We then explored the individual contributions of the clusters to the shape of the total density pdf. We determined that the exponential tail is composed of many smaller clusters, rather than a single cluster. This is an important result because it can help constrain models for the origin of the tail, which remains to be explained.

Contrary to commonly-held beliefs, we also found that the characteristic dimension of the cluster along the long-axis is commensurate with the Taylor microscale, and not the Kolmogorov scale. This is consistent with the discussion from Chapter 4 (see Section 4.5) that suggested that the Taylor microscale is the dominant scale of the particle concentration fluctuations as evidenced by the fact that the power spectrum of the particle concentration field peaked around the Taylor microscale (see Section 4.3). We explored an advection-diffusion model to for the width of the cluster, and found it to work as long as the predicted length-scale was larger than twice the grid resolution. For clusters that would be thinner than that, we found that the measured thickness was commensurate with the grid scale, suggesting that our detection algorithm (and simulations) may be limited by the resolution of the algorithm. Higher resolution simulations will be needed to establish whether the advection-diffusion model for the cluster thickness holds for a wider range of parameter space.

Finally, another question that deserves further attention concerns the lifetime of the identified clusters, and specifically, how the shape and densities of the

clusters change over time. With this in mind for clouds, we may be able to determine the likelihood for coalescence to occur, and thus, be able to predict the probability of larger raindrops forming for a given cluster. In order to answer this question however, we would require other means to track clusters individually, which we do not do in this study.

Chapter 6

Conclusion

This thesis is motivated by the need to understand particle growth in a number of geophysical and astrophysical applications, such as in clouds and accretion disks. One physical process that may play a fundamental role in enhancing collision rates in particle-laden flows is turbulence-induced preferential concentration, which describes the tendency of inertial particles to accumulate in certain regions of the flow, subsequently increasing local particle concentrations. In this work, we investigated the effect of preferential concentration in turbulent systems consisting of small, heavy particles using the two-fluid equations. We attempted to characterize and quantify the dependence of various statistical properties of the particle density field (such as its extremum, its rms, and the tail of the pdf), on the properties of the turbulence. Finally, we explored the properties of these dense clusters that may help shed light on collisional growth of relevant applications. One of the most important conclusions of this thesis is that preferential concentration can be important even when the Stokes number St is not particularly large, and that the statistical properties of the particle density distribution are interesting, and worth studying, even for low St.

In Chapter 3, we studied preferential concentration in a two-way coupled

particle-laden flow in the particle-induced Rayleigh-Taylor instability. The model set-up consisted of an unstable particle layer that settles in a stably stratified fluid. We used 2D DNSs and limited our exploration to particles with Stokes number $\lesssim O(0.1)$. In the presence of preferential concentration during the peak of the mixing event, we noted strongly enhanced particle concentrations with observed densities several standard deviations above the mean within the bulk of the particle layer.

We found that the particle concentration enhancement of the system could be predicted by assuming a dominant balance between the inertial concentration term and diffusion term from the particle transport equation. Specifically, we showed that the maximum particle concentration enhancement above the mean is related to the particle stopping time τ_p, the rms fluid velocity in the turbulent layer u_{rms}, and the assumed particle diffusivity κ_p, scaling as $u_{rms}^2 \tau_p \kappa_p$. We also found that the typical particle concentration enhancement over the mean scales like the square root of the same parameter group, expressed as $(u_{rms}^2 \tau_p \kappa_p)^{1/2}$. We showed that the pdfs of particle concentration enhancement had an exponential tail, whose slope scales as $(u_{rms}^2 \tau_p \kappa_p)^{-1/2}$. Although our findings were valid in the context of particle-driven convection, it remained to be determined whether the same results could be obtained in systems where turbulence was driven independently from the particles themselves.

For this reason in Chapter 4, we tested if the same scalings were also valid for particle-laden flows in which turbulence was mechanically-driven. To do so, we drove the mean flow using a body force given by a sinusoidal flow, forcing the system to be shear-unstable. Due to the high resolution needed for the 3D DNSs used in this case, we limited our parameter space to Stokes number $\lesssim O(0.01)$ and moderate turbulence with fluid Reynolds number $Re \leq 600$. For this study,

we analyzed the system only once the simulations reached a statistically steady state. We confirmed that the same scalings for the maximum and typical particle concentration enhancements applied here as well. Additionally, we showed that the pdf of the particle concentration again has an exponential tail whose slope scaled like $(u_{rms}^2 \tau_p \kappa_p)^{-1/2}$.

The predominance of the parameter group $u_{rms}^2 \tau_p \kappa_p$ in all of these scalings is to some extent rather surprising, because it arises from very simplistic arguments of dominant balance that, admittedly, are probably not very well justified. Indeed, we assumed a balance between the preferential concentration of the *mean* particle density and diffusion terms of the perturbations, shown dimensionally as

$$\bar{r} \nabla \cdot \mathbf{u}_p \sim \kappa_p \nabla^2 r'.$$

But since in many of the simulations $r' \gg \bar{r}$, the largest term in the particle equation should logically be $r' \nabla \cdot \mathbf{u}_p$ instead. However, if we were to follow the same derivation for the predictive model as originally presented in Section 3.4 with

$$r' \nabla \cdot \mathbf{u}_p \sim \kappa_p \nabla^2 r',$$

the terms involving particle concentration r' would cancel out, and one would not recover the observed scaling for $r'/\bar{r}$. The fact that two distinct sets of numerical experiments follow the scaling law proposed in Section 3.4, despite the flaws in the dominant balance argument, is therefore quite surprising. Future work will therefore be needed to understand *why* it works. A possible explanation may lie in the statistics of the simulations – i.e. the balance $\bar{r} \nabla \cdot \mathbf{u}_p \sim \kappa_p \nabla^2 r'$ may only be true on average in dense clusters, rather than for individual realizations of the flow.

Additionally, it also remains unclear, and perhaps counterintuitive, as to why the proposed scaling depends on u_{rms}, and not another measure of the fluid velocity. Although we do have tenuous evidence that these scalings do hold, this may be tied to the fact that the turbulence driven in the systems we have explored so far has a small inertial range, so u_{rms} may be taken as a reasonable estimate for the velocity of the eddies at all scales. By contrast, for turbulence at much higher Reynolds number, the inertial range spans many decades in eddy scales, so the typical eddy velocity at the injection scale will be very different from the eddy velocity at, e.g. the Taylor microscale. When this is the case, the scalings discussed here may break down. However if the scalings are found to be universally true (i.e. the u_{rms} is the correct choice for systems with higher Reynolds number), this will have a substantial impact on understanding how turbulence affects the resulting particle concentration enhancement.

Similarly, another key question that remains unanswered is the reason as to why the exponential tail of the pdfs of the particle concentration exists in the first place, and why its slope scales like $(u_{rms}^2 \tau_p \kappa_p)^{-1/2}$. Although we have a strong clue indicating that the shape of the pdf is related to the fact that it is made up of many clusters, and that the slope relates to the rms particle concentration, the reason still remains unclear, and therefore in that regard, future work is needed. On a positive note, we found that Shotorban & Balachandar (2006) also show that an exponential tail develops in the particle density pdfs both in the two-fluid and in the Lagrangian formalisms, demonstrating that it is not an artifact of the two-fluid equations in our own simulations.

Finally in Chapter 5, we aimed to characterize key attributes of the particle structures due to preferential concentration. We restricted our study to the dense regions found within the exponential tail of the pdfs of the particle concentration.

In order to identify the clusters, we used a box counting algorithm and extracted cluster features such as mass, size, and shape. Snapshots of the particles in Chapter 4 showed that the densest regions appeared to be found in elongated, thin layers. We confirmed this, showing that the typical particle clusters are indeed filamentary, with a mean aspect ratio of 10. We explored the physics responsible for the distinct shape of the particle clusters, and found partial evidence that the long dimension of the clusters is commensurate with the Taylor microscale, while the smaller dimension may (or may not) be commensurate with the characteristic width due to the advection-diffusion balance, i.e. $\hat{\delta}_{\min} \sim (\hat{U}_{rms} Pe_p)^{-1}$ (the latter finding remains to be confirmed for larger Re, and we would require using a higher resolution). If these results are proven to hold, then we may be able to use them to estimate the average volume and mass of particle clusters.

In this thesis, we have demonstrated that preferential concentration can be significant for small Stokes number, which has been shown to be relevant for various applications (see Sections 3.6.2 and 4.5.3). These findings also provide a different perspective to the current literature, which has primarily focused on particles with Stokes number of unity, where preferential concentration is found to be the most efficient in accumulating particles. Our goals in this study were aimed to enable us to predict statistical properties of the number density of cloud droplets, and then later to forecast properties of the coagulated drops. In that respect, we were able to go part way in characterizing several notable aspects of the regions corresponding to significant particle concentration enhancement, where collisional growth is relevant. In future work, we hope to investigate other turbulent systems and regions of parameter space, such as higher Reynolds numbers, and explore if these results also hold, which may have further implications to real-life applications.

Appendix A

Laplace's Approximation

We start from the nondimensional equation describing the motion of a single spherical particle as introduced in (1.4)

$$\frac{d\hat{\mathbf{v}}_p}{dt} = \frac{1}{St}\Big\{\hat{\mathbf{u}}(\hat{\mathbf{x}}_p(t), t) - \hat{\mathbf{v}}_p + \hat{\mathbf{w}}_s\Big\},$$

where $\hat{\mathbf{u}}$ is the fluid velocity at the particle position $\hat{\mathbf{x}}_p$ at time t, $\hat{\mathbf{v}}_p$ is the particle velocity, and $\hat{\mathbf{w}}_s$ is the particle settling velocity.

We integrate it over the time interval $[t_0, t]$ and obtain the integral solution for the particle velocity $\hat{\mathbf{v}}_p$:

$$\hat{\mathbf{v}}_p = e^{-t/St}\hat{\mathbf{v}}_p(t_0) + \hat{\mathbf{w}}_s(1 - e^{-t/St}) + \int_{t_0}^{t} \frac{\hat{\mathbf{u}}(t')}{St} e^{(t'-t)/St}\, dt'. \tag{A.1}$$

In the limit of $t \gg St$, the exponential terms outside of the integral are vanishingly small, and we rewrite $\hat{\mathbf{v}}_p$ as

$$\hat{\mathbf{v}}_p = \hat{\mathbf{w}}_s + \frac{1}{St}\int_{t_0}^{t} \hat{\mathbf{u}}(t') e^{-(t'-t)/St}\, dt'. \tag{A.2}$$

We can solve for the integral on the right-hand side by applying the Laplace

approximation. To do so, we note this term is of the form

$$\int_a^b e^{-\lambda(t'-t)} f(t')\, dt', \tag{A.3}$$

where

1. $\lambda = 1/St$ is very large (provided St is very small), and

2. $f(t) = \hat{u}_i(t)$ is a smooth function,

so that we can use Laplace's approximation:

$$\int_a^b e^{-\lambda t} f(t)\, dt \approx e^{-\lambda a} \left(\frac{f(a)}{\lambda} + \frac{f'(a)}{\lambda^2} \right). \tag{A.4}$$

Thus, $\hat{\mathbf{v}}_p$ can be written as:

$$\hat{\mathbf{v}}_p(t) = \hat{\mathbf{u}}(t) + \hat{\mathbf{w}}_s - St\frac{d\hat{\mathbf{u}}}{dt} + O(St^2), \tag{A.5}$$

which agrees with the equation for the instantaneous particle velocity given by (1.9).

Bibliography

Aliseda, A., Cartellier, A., Hainaux, F., & Lasheras, J. C. 2002, Journal of Fluid Mechanics, 468, 77

Alsinan, A., Meiburg, E., & Garaud, P. 2017

Anderson, E., Bai, Z., Bischof, C., et al. 1999, LAPACK Users' guide (SIAM)

Anderson, T. B., & Jackson, R. 1967, Industrial & Engineering Chemistry Fundamentals, 6, 527

Ayala, O., Rosa, B., Wang, L.-P., & Grabowski, W. W. 2008, New Journal of Physics, 10, 075015

Bakhtyar, R., Yeganeh-Bakhtiary, A., Barry, D. A., & Ghaheri, A. 2009, Advances in Water Resources, 32, 1267

Balachandar, S., & Eaton, J. K. 2010, Annual review of fluid mechanics, 42, 111

Balmforth, N. J., & Young, Y.-N. 2002, Journal of Fluid Mechanics, 450, 131

Bateson, C. P., & Aliseda, A. 2012, Experiments in fluids, 52, 1373

Beaumont, D. 1981, Journal of Fluid Mechanics, 108, 461

Birnstiel, T., Fang, M., & Johansen, A. 2016, Space Science Reviews, 205, 41

Blum, J. 2006, Advances in Physics, 55, 881

Blum, J., & Wurm, G. 2008, Annu. Rev. Astron. Astrophys., 46, 21

Bosse, T., Kleiser, L., & Meiburg, E. 2006, Physics of Fluids, 18, 027102

Boussinesq, J. 1903a, Theorie analytique de la chaleur, 2, 172

—. 1903b, Théorie analytique de la chaleur mise en harmonic avec la thermodynamique et avec la théorie mécanique de la lumière: Tome I-[II]..., Vol. 2 (Gauthier-Villars)

Burns, P., & Meiburg, E. 2012, Journal of fluid mechanics, 691, 279

—. 2015, Journal of Fluid Mechanics, 762, 156

Canuto, C., Hussaini, M. Y., Quarteroni, A., & Zang, T. A. 2007, Spectral methods: evolution to complex geometries and applications to fluid dynamics (Springer Science & Business Media)

Cao, Z.-M., Nishino, K., Mizuno, S., & Torii, K. 2000, Experiments in fluids, 29, S211

Carazzo, G., & Jellinek, A. 2013, Journal of Geophysical Research: Solid Earth, 118, 1420

Carrier, G. 1958, Journal of Fluid Mechanics, 4, 376

Cerminara, M., Ongaro, T. E., & Neri, A. 2016, Journal of Volcanology and Geothermal Research, 326, 143

Chambers, J. 2010, Icarus, 208, 505

Chein, R., & Chung, J. 1988a, Chemical engineering science, 43, 1621

—. 1988b, AIChE Journal, 34, 946

Chou, Y.-J., & Shao, Y.-C. 2016, Physics of Fluids, 28, 043302

Chou, Y.-J., Wu, F.-C., & Shih, W.-R. 2014a, International Journal of Multiphase Flow, 64, 35

—. 2014b, International Journal of Multiphase Flow, 64, 44

Coleman, S., & Vassilicos, J. 2009, Physics of Fluids, 21, 113301

Crowe, C., Chung, J., & Troutt, T. 1988, Progress in energy and combustion science, 14, 171

Crowe, C., Gore, R., & Troutt, T. 1985, Particulate Science and Technology, 3, 149

Crowe, C., Troutt, T., & Chung, J. 1996, Annual review of fluid mechanics, 28, 11

Csanady, G. 1963, Journal of the Atmospheric Sciences, 20, 201

Cuzzi, J. N., Hogan, R. C., Paque, J. M., & Dobrovolskis, A. R. 2001, The Astrophysical Journal, 546, 496

Cuzzi, J. N., Hogan, R. C., & Shariff, K. 2008, The Astrophysical Journal, 687, 1432

Delhaye, J., & Achard, J. 1976, On the averaging operators introduced in two-phase flow modeling (Centre d'études nucléaires de Grenoble)

Devenish, B., Bartello, P., Brenguier, J.-L., et al. 2012, Quarterly Journal of the Royal Meteorological Society, 138, 1401

Druzhinin, O. 1995, Journal of Fluid Mechanics, 297, 49

Druzhinin, O., & Elghobashi, S. 1998, Physics of Fluids, 10, 685

Eaton, J. K. 1994

Eaton, J. K., & Fessler, J. 1994, International Journal of Multiphase Flow, 20, 169

Eisma, D. 1991, Geo-Marine Letters, 11, 147

Elghobashi, S. 1994, Applied scientific research, 52, 309

Elghobashi, S., & Abou-Arab, T. 1983, The Physics of Fluids, 26, 931

Elghobashi, S., & Truesdell, G. 1992, Journal of Fluid Mechanics, 242, 655

—. 1993, Physics of Fluids A: Fluid Dynamics, 5, 1790

Falkovich, G., Fouxon, A., & Stepanov, M. 2002, Nature, 419, 151

Ferry, J., & Balachandar, S. 2001, International journal of multiphase flow, 27, 1199

—. 2002, Powder Technology, 125, 131 , the fourth international conference on multiphase Flow

Ferry, J., Rani, S. L., & Balachandar, S. 2003, International Journal of Multiphase Flow, 29, 869

Fessler, J. R., Kulick, J. D., & Eaton, J. K. 1994, Physics of Fluids, 6, 3742

Friedlander, S., & Howard, L. 1998, Studies in Applied Mathematics, 101, 1

Frisch, A. S., Martner, B. E., Djalalova, I., & Poellot, M. R. 2000, Journal of Geophysical Research: Atmospheres, 105, 15361

Gañán-Calvo, A. M., & Lasheras, J. C. 1991, Physics of Fluids A: Fluid Dynamics, 3, 1207

Garaud, P., & Brummell, N. 2015, The Astrophysical Journal, 815, 42

Garaud, P., Gallet, B., & Bischoff, T. 2015, Physics of Fluids, 27, 084104

Garaud, P., & Kulenthirarajah, L. 2016, The Astrophysical Journal, 821, 49

Garaud, P., & Nasab, S. 2019, in AAS/Division for Extreme Solar Systems Abstracts, Vol. 51, AAS/Division for Extreme Solar Systems Abstracts, 317.09

Ghosh, S., & Jonas, P. 2001, Geophysical research letters, 28, 3883

Goto, S., & Vassilicos, J. 2006, Physics of Fluids, 18, 115103

—. 2008, Physical review letters, 100, 054503

Grabowski, W. W., & Wang, L.-P. 2013, Annual review of fluid mechanics, 45, 293

Ham, J., & Homsy, G. 1988, International journal of multiphase flow, 14, 533

Harrington, P. Z., & Garaud, P. 2019, The Astrophysical Journal Letters, 870, L5

Harris, D. M., & Rose Jr, W. I. 1983, Journal of Geophysical Research: Oceans, 88, 10969

Hoyal, D. C., Bursik, M. I., & Atkinson, J. F. 1999, Journal of Geophysical Research: Oceans, 104, 7953

Hsu, T.-J., Jenkins, J. T., & Liu, P. L.-F. 2004, Proceedings of the Royal Society of London. Series A: Mathematical, Physical and Engineering Sciences, 460, 2223

Ishii, M., & Hibiki, T. 2010, Thermo-fluid dynamics of two-phase flow (Springer Science & Business Media)

Ishii, M., & Mishima, K. 1984, Nuclear Engineering and design, 82, 107

Jackson, R. 1997, Chemical Engineering Science, 52, 2457

Johansen, A., Klahr, H., & Henning, T. 2006, The Astrophysical Journal, 636, 1121

Kada, H., & Hanratty, T. J. 1960, AIChE Journal, 6, 624

Klahr, H. H., & Henning, T. 1997, Icarus, 128, 213

Kobayashi, H., Masutani, S., Azuhata, S., Arashi, N., & Nishinuma, Y. 1988, Transport Phenomena in Turbulent Flows: Theory, Experiment, and Numerical Simulation, 433

Kraichnan, R. H. 1970, The physics of fluids, 13, 22

Kuerten, J. G. 2016, Flow, turbulence and combustion, 97, 689

Kulick, J. D., Fessler, J. R., & Eaton, J. K. 1994, Journal of Fluid Mechanics, 277, 109

Laitone, J. A. 1981

Marble, F. E. 1970, Annual Review of Fluid Mechanics, 2, 397

Marchioli, C. 2017, Acta Mechanica, 228, 741

Maxey, M. 1987, Journal of Fluid Mechanics, 174, 441

Maxey, M., & Corrsin, S. 1986, Journal of Atmospheric Sciences, 43, 1112

Maxey, M. R., & Riley, J. J. 1983, The Physics of Fluids, 26, 883

Maxworthy, T. 1999, Journal of Fluid Mechanics, 392, 27

Mecke, K. R., Buchert, T., & Wagner, H. 1993, arXiv preprint astro-ph/9312028

Meek, C. C., & Jones, B. G. 1973, Journal of the Atmospheric Sciences, 30, 239

Mei, R. 1994, International journal of multiphase flow, 20, 273

Meiburg, E., & Kneller, B. 2010, Annual Review of Fluid Mechanics, 42, 135

Minkowski, H. 1903, in Encyklopädie der Mathematischen Wissenschaften mit Einschluss ihrer Anwendungen (Springer), 558–613

Mittal, R., & Iaccarino, G. 2005, Annu. Rev. Fluid Mech., 37, 239

Moll, R., Garaud, P., & Stellmach, S. 2016, The Astrophysical Journal, 823, 33

Monchaux, R., Bourgoin, M., & Cartellier, A. 2010, Physics of Fluids, 22, 103304

—. 2012, International Journal of Multiphase Flow, 40, 1

Morel, C. 2015, Mathematical modeling of disperse two-phase flows (Springer)

Nakagawa, Y., Sekiya, M., & Hayashi, C. 1986, Icarus, 67, 375

Nasab, S., & Garaud, P. 2020, Physical Review Fluids, 5, 114308

—. 2021, arXiv preprint arXiv:2103.08121

Necker, F., Härtel, C., Kleiser, L., & Meiburg, E. 2002, International Journal of Multiphase Flow, 28, 279

Nicolai, H., Herzhaft, B., Hinch, E., Oger, L., & Guazzelli, E. 1995, Physics of Fluids, 7, 12

Obligado, M., Teitelbaum, T., Cartellier, A., Mininni, P., & Bourgoin, M. 2014, Journal of Turbulence, 15, 293

Ouillon, R., Edel, P., Garaud, P., & Meiburg, E. 2020

Parsons, J. D., Bush, J. W., & Syvitski, J. P. 2001, Sedimentology, 48, 465

Peyret, R. 2002, Spectral methods for incompressible viscous flow, Vol. 148 (Springer Science & Business Media)

Pinsky, M., & Khain, A. 2002, Quarterly Journal of the Royal Meteorological Society: A journal of the atmospheric sciences, applied meteorology and physical oceanography, 128, 501

Platt, N., Sirovich, L., & Fitzmaurice, N. 1991, Physics of Fluids A: Fluid Dynamics, 3, 681

Press, W. H. 1996, Numerical recipes in Fortran 90 (Univ. Press)

Raju, N., & Meiburg, E. 1995, Physics of Fluids, 7, 1241

—. 1997, Physics of Fluids, 9, 299

Reali, J., Garaud, P., Alsinan, A., & Meiburg, E. 2017, Journal of Fluid Mechanics, 816, 268

Reeks, M. W. 1980, Journal of Fluid Mechanics, 97, 569

Revil-Baudard, T., & Chauchat, J. 2013, Journal of Geophysical Research: Oceans, 118, 619

Riemer, N., & Wexler, A. 2005, Journal of the atmospheric sciences, 62, 1962

Riley, J. J. 1971, Computer simulations of turbulent dispersion (The Johns Hopkins University)

Rouson, D. W., & Eaton, J. K. 2001, Journal of Fluid Mechanics, 428, 149

Saw, E. W., Shaw, R. A., Ayyalasomayajula, S., Chuang, P. Y., & Gylfason, A. 2008, Physical review letters, 100, 214501

Schmalzing, J., & Buchert, T. 1997, The Astrophysical Journal Letters, 482, L1

Schmalzing, J., Kerscher, M., & Buchert, T. 1995, arXiv preprint astro-ph/9508154

Schreck, S., & Kleis, S. J. 1993, Journal of Fluid Mechanics, 249, 665

Segre, P. N., Liu, F., Umbanhowar, P., & Weitz, D. A. 2001, Nature, 409, 594

Shao, Y.-C., Hung, C.-Y., & Chou, Y.-J. 2017, Journal of Fluid Mechanics, 824, 513

Shapiro, L. 1992, Computer vision and image processing (Academic Press)

Shaw, R. A. 2003, Annual Review of Fluid Mechanics, 35, 183

Shotorban, B., & Balachandar, S. 2006, Physics of Fluids, 18, 065105

Sommerfeld, M. 2017, in Particles in Flows (Springer), 327–396

Sparks, R., & Wilson, L. 1976, Journal of the Geological Society, 132, 441

Spiegel, E., & Veronis, G. 1960, The Astrophysical Journal, 131, 442

Squires, K. D., & Eaton, J. K. 1990, Physics of Fluids A: Fluid Dynamics, 2, 1191

—. 1991, Physics of Fluids A: Fluid Dynamics, 3, 1169

Stellmach, S., & Hansen, U. 2008, Geochemistry, Geophysics, Geosystems, 9

Stellmach, S., Traxler, A., Garaud, P., Brummell, N., & Radko, T. 2010, arXiv preprint arXiv:1008.1808

—. 2011, Journal of Fluid Mechanics, 677, 554

Tang, L., Wen, F., Yang, Y., et al. 1992, Physics of Fluids A: Fluid Dynamics, 4, 2244

Tithof, J., Suri, B., Pallantla, R. K., Grigoriev, R. O., & Schatz, M. F. 2017, Journal of Fluid Mechanics, 828, 837

Tobin, J. J., Hartmann, L., Chiang, H.-F., et al. 2012, Nature, 492, 83

Toschi, F., & Bodenschatz, E. 2009, Annual Review of Fluid Mechanics, 41, 375

Traxler, A., Garaud, P., & Stellmach, S. 2011a, The Astrophysical Journal Letters, 728, L29

Traxler, A., Stellmach, S., Garaud, P., Radko, T., & Brummell, N. 2011b, Journal of Fluid Mechanics, 677, 530

van der Poel, E. P., Stevens, R. J., & Lohse, D. 2013, Journal of fluid mechanics, 736, 177

van Veen, L., & Goto, S. 2016, Fluid Dynamics Research, 48, 061425

Vié, A., Franzelli, B., Gao, Y., et al. 2015, Proceedings of the Combustion Institute, 35, 1675

Völtz, C., Pesch, W., & Rehberg, I. 2001, Physical Review E, 65, 011404

Voulgaris, G., & Meyers, S. T. 2004, Continental Shelf Research, 24, 1659

Wang, L.-P., Ayala, O., Rosa, B., & Grabowski, W. W. 2008, New Journal of Physics, 10, 075013

Wang, L.-P., & Maxey, M. R. 1993, Journal of fluid mechanics, 256, 27

Wang, L.-P., Wexler, A. S., & Zhou, Y. 2000, Journal of Fluid Mechanics, 415, 117

Wang, Q., & Squires, K. D. 1996, Physics of Fluids, 8, 1207

Webster, H., Thomson, D., Johnson, B., et al. 2012, Journal of Geophysical Research: Atmospheres, 117

Weidenschilling, S. 1977, Monthly Notices of the Royal Astronomical Society, 180, 57

Weidenschilling, S., & Cuzzi, J. N. 1993, in Protostars and planets III, 1031–1060

Wen, F., Kamalu, N., Chung, J., Crowe, C., & Troutt, T. 1992

Woods, A. W. 1995, Reviews of geophysics, 33, 495

Yang, C., & Lei, U. 1998, Journal of Fluid Mechanics, 371, 179

Yau, M. K., & Rogers, R. R. 1996, A short course in cloud physics (Elsevier)

Yeung, P. K. 2002, Annual Review of Fluid Mechanics, 34, 115

Yoshimoto, H., & Goto, S. 2007, Journal of Fluid Mechanics, 577, 275

Youdin, A. N., & Goodman, J. 2005, The Astrophysical Journal, 620, 459

Zaichik, L., & Alipchenkov, V. 2005, International Journal of Heat and Fluid Flow, 26, 416

Zaichik, L. I., & Alipchenkov, V. M. 2003, Physics of Fluids, 15, 1776

Zhang, D., & Prosperetti, A. 1994, Journal of Fluid Mechanics, 267, 185